Impact ionization Characterisation of $Al_{0.70}In_{0.30}As_{0.74}Sb_{0.26}$ p-i-n and $GaAs/Ga_{0.96}AsBi_{0.04}$ MQW photodiodes

Xiaofeng Tao

A thesis submitted for the degree of Doctor of Philosophy

School of Electronic and Electrical Engineering

The University of Sheffield

25/10/2024

Declaration of Authorship

I, Xiaofeng Tao, declare that this thesis titled, “Impact ionization Characterisation of $Al_{0.70}In_{0.30}As_{0.74}Sb_{0.26}$ p-i-n and $GaAs/Ga_{0.96}AsBi_{0.04}$ MQW photodiodes” and the work presented in it are my own. I confirm that:

- This work was completed primarily during my PhD period at the University of Sheffield.
- Any part of this thesis previously submitted for a degree or other qualification at any institution is clearly indicated.
- Published work consulted is properly attributed.
- All quotations from other works are cited, and apart from those, this thesis represents my original work.
- I have acknowledged all major sources of assistance.
- Where the research involved collaboration, I have clarified my individual contributions and those of others.

Signed: Xiaofeng Tao

Date: 25/10/2024

Abstract

The goal of this work is to first, characterize the impact ionization properties of $Al_{0.70}In_{0.30}As_{0.74}Sb_{0.26}$ for its potential application as the avalanche multiplication layer in separate absorption and multiplication avalanche photodiodes (SAM-APDs) on an InP substrate for optical communication systems. Previous studies on $AlAs_{0.56}Sb_{0.44}$ homojunction diodes were systematically investigated at room temperature. It was found that the bulk electron and hole ionization coefficients, α and β respectively, differ significantly, exhibiting "silicon-like" behaviour at low electric fields and noise showed the excess noise on an InP substrate, with k=0.005. However, this material is prone to oxidation and surface leakage current. These issues are significantly mitigated by using the AlInAsSb quaternary alloy system, which offers improved stability and reduced leakage. In this work, the multiplication, ionization coefficients, and excess noise characteristics for the AlInAsSb alloy on an InP substrate were presented over an electric field range of 0.33–0.6 MV/cm. These findings provide valuable insights for the design and optimization of high-performance shortwave infrared (SWIR) Separate Absorption, Charge, and Multiplication (SACM) Avalanche Photodiodes (APDs) using an AlInAsSb multiplication layer on commercially viable InP substrates.

Secondly, characterize the impact ionization coefficients of GaAs/GaAsBi multiple quantum well. In previous research, the systematic analysis on the series of bulk GaAsBi p-i-n and n-i-p samples, with varying intrinsic region thicknesses and bismuth content revealed a significant disparity between electron and hole ionization coefficients. In this research, introducing thin layers of GaAsBi as quantum wells (QWs) within a GaAs matrix can enhance the performance of avalanche structures. For the first time, a systematic study of avalanche multiplication in a series of GaAsBi/GaAs multiple quantum well (MQW) structures grown in a p-i-n configuration was undertaken, and their ionization behaviours was examined through photomultiplication measurements. The α/β ratio in GaAs was increased by suppressing hole impact ionization, achieved by modifying the valence band structure.

List of publications

Journal papers:

1. T. J. Ronningen, S. H. Kodati, X. Jin, S. Lee, H. Jung, **X. Tao**, H. I. J. Lewis, M. Schwartz, N. Gajowski, P. Martyniuk, B. Guo, A. H. Jones, J. C. Campbell, C. Grein, J. P. R. David and S. Krishna, "Ionization coefficients and excess noise characteristics of AlInAsSb on an InP substrate", *Applied Physics Letters* (2023). 123, 13.

2. **X. Tao**, X. Jin, S. Gao, X. Yi, Y. Liu, T. B. Rockett, N. J. Bailey, F. Harun, N. A. Adham, C. H. Tan, R. D. Richards and J. P. David. "Engineering of impact ionization characteristics in GaAs/GaAsBi multiple quantum well avalanche photodiodes". Submitted to ACS Photonics.

Oral and poster presentation:

1. N. A. Adham, **X. Tao**, N. J. Bailey, F. Harun, J. P. R. David and R. D. Richards, *Electroluminescence comparison between bulk and MQD GaAsBi structures*, UK Semiconductor. Sheffield, UK, 6th July 2022

2. **X. Tao**, X. Jin, Y. Liu, C. H. Tan, R. D. Richards, J. P. R. David and X. Yi, *Characterisation of GaAsBi Multiple quantum well photodiodes*, Semiconductor and Integrated Opto-Electronics Conference, Cardiff, UK, 5th April 2023

3. R. D. Richards, **X. Tao**, X. Jin, C. H. Tan, J. Bork, J. M. O Zide and J. P. R. David, *Characterisation of InAlAsBi pin photodiodes*, Semiconductor and Integrated Opto-Electronics Conference, Cardiff, UK, 5th April 2023

4. J. Bork, R. D. Richards, W. Acuna, **X. Tao**, X. Jin, C. H. Tan, J. P. R. David and J. Zide, *(In)AlBiAs-Based Short-Wave Infrared Avalanche Photodiodes*, 65th Electronic Materials Conference, California, USA, 28th 2023

5. S. Gao, **X. Tao**, X. Jin, Y. Liu, N. J. Bailey, C. H. Tan, J. P. R. David and R. D. Richards, *Characterisation of GaAs/GaAsBi heterostructure photodiodes*, Semiconductor and Integrated Opto-Electronics Conference, Cardiff, UK, 5th April 2024

Acknowledgements

I would like to express my deepest gratitude to my supervisor, Professor John P. R. David, whose invaluable guidance and unwavering support were pivotal throughout this journey. His profound knowledge, especially on the fundamentals of semiconductors and impact ionization theory, has been a constant source of inspiration. Without his advice and mentorship, this work would not have been possible. I would also like to thank Dr. Robert D. Richards, Professor Jo S. Ng and Professor Chee H. Tan for their supervision.

I would also like to extend my thanks to Dr. Nicholas. J. Bailey, Dr. Thomas B. O. Rockett as well as to Dr. Xin Yi for their ongoing support. Special thanks go to Dr. Yuchen Liu and Dr. Xiao Jin, whose insightful guidance at the initial stages of the project set a solid foundation for this work and particularly in guiding me through device fabrication and assisting with the experimental set-up, as well as for the many enlightening discussions we had. I am also grateful to Shiyuan Gao, Yifan Liu, Nada A. Adham, Matthew Carr and Qingyu Tian, who have been wonderful companions throughout my PhD studies.

Additionally, I would like to express my appreciation to Dr. Ye Cao, Dr. Yuting Ji, Dr. Tarick Blain and Dr. Jonathan Petticrew for their assistance in the lab.

Meanwhile, I would like to thank Dr. Seunghyun Lee, Dr. T. J. Ronningen, and their co-workers for providing the MBE growth and device fabrication from Ohio State University.

A heartfelt thank you to the members of the Impact Ionization Group (2020–2024) at the University of Sheffield, whose camaraderie and support made a significant difference.

Finally, and most importantly, I would like to acknowledge my parents for their unwavering financial and emotional support. Their encouragement has been the driving force behind my achievements.

Contents

List of Figures

List of Tables

1. CHAPTER 1: Introduction

1.1 Overview

Photodetectors have become increasingly important in today's world due to their critical role in numerous applications across numerous fields, for example, telecommunications, medical diagnostics, environmental monitoring, industrial automation, and scientific research. As technology advances and industries continue to evolve, the demand for efficient, sensitive, and reliable photodetectors has grown exponentially, making them essential components in many modern systems. Their significance stems from their ability to convert light into electrical signals, enabling a wide range of innovations and advancements in both everyday technology and high-precision scientific instruments.

One of the most prominent areas where photodetectors are indispensable is telecommunications, particularly in fibre-optic communication systems. In this domain, photodetectors play a vital role in converting light signals transmitted through optical fibres into electrical signals that can be processed by electronic devices. As the backbone of the internet and data transfer networks, fibre-optic systems rely heavily on photodetectors for high-speed data transmission with negligible signal power loss and reduced interference. The growing demand for faster and more reliable internet connectivity, along with the advent of 5G networks and cloud-based services, has made the efficiency of photodetectors crucial to meeting these needs. Improvements in photodetector technology directly translate into enhanced communication speeds, bandwidth, and overall network performance.

In the field of medical diagnostics, photodetectors have proven to be invaluable tools in the development of advanced imaging techniques and diagnostic devices. They are integral to medical imaging systems like X-rays, computed tomography (CT) scans, and positron emission tomography (PET) scans, where they detect the light emitted from various biological tissues and convert it into detailed images for analysis. Photodetectors are also fundamental in blood analysis equipment, fluorescence microscopy, and optical coherence tomography (OCT), which is used extensively in ophthalmology for detailed imaging of the retina. As the demand for early disease detection and minimally invasive diagnostic procedures grows, the importance of photodetectors in enabling these technologies becomes even more pronounced. Their ability to deliver precise, real-time results has improved the accuracy of medical diagnoses and expanded the potential for personalised healthcare.

Environmental monitoring and remote sensing are other areas where photodetectors play a crucial role. With growing concerns about climate change, pollution, and natural resource management, the need for accurate environmental monitoring systems has never been more pressing. Photodetectors are used in sensors that monitor air and water quality, detect hazardous gases, measure atmospheric conditions, and even track the health of crops and forests using satellite-based remote sensing. These applications rely on the sensitivity and accuracy of photodetectors to detect light from various sources, analyse spectral data, and provide actionable insights for environmental conservation efforts. As governments and organisations around the world intensify their focus on sustainability, photodetectors will continue to be key components in developing and implementing effective environmental monitoring solutions.

In industrial automation and manufacturing, photodetectors are essential for improving efficiency, safety, and precision. They are widely used in applications like machine vision, quality control, robotics, and process automation, where they enable machines to detect and respond to changes in their environment with high speed and accuracy. For example, in quality control, photodetectors are used to inspect products for defects, measure dimensions, and ensure that manufacturing standards are met. In robotics, they help guide autonomous systems by detecting obstacles, interpreting visual signals, and navigating complex environments. As industries move towards smart manufacturing and the implementation of the Internet of Things (IoT), the role of photodetectors in facilitating real-time data acquisition and automation will become even more critical.

Scientific research and space exploration also heavily depend on the capabilities of photodetectors. In fields like astronomy, photodetectors are used in telescopes and observatories to capture and analyse light from distant stars, galaxies, and other celestial objects. High-sensitivity photodetectors allow astronomers to study the universe's structure, detect exoplanets, and gather data on cosmic phenomena like supernovae and black holes. In particle physics, photodetectors are used in experiments that require the detection of faint light emissions from particle collisions or radioactive decay. These devices are crucial for understanding fundamental physical laws and exploring new frontiers in science. Advances in photodetector technology have led to breakthroughs in these fields, enabling researchers to make new discoveries and deepen our understanding of the universe.

Moreover, the rise of autonomous vehicles and advanced driver assistance systems (ADAS) has highlighted the importance of photodetectors in modern transportation technologies. Photodetectors are central to LIDAR (Light Detection and Ranging) systems, which provide vehicles with 3D mapping capabilities and obstacle detection by emitting laser pulses and measuring the reflected light. The accurate and real-time detection of surrounding objects is vital for the safe operation of self-driving cars, as it allows them to navigate complex environments and avoid collisions. As the automotive industry pushes towards greater automation and the development of fully autonomous vehicles, the demand for highly sensitive and reliable photodetectors will continue to grow.

In the context of consumer electronics, photodetectors are present in a wide range of everyday devices, from smartphones and digital cameras to smart home systems and wearable health monitors. In cameras, photodetectors are responsible for capturing light and converting it into digital images, affecting the quality and resolution of photographs. They are also used in proximity sensors, ambient light sensors, and facial recognition technology, enhancing user experience and device functionality. The integration of photodetectors in smart home devices, such as automated lighting systems and security cameras, helps create responsive environments that improve convenience, energy efficiency, and safety.

As artificial intelligence (AI) and machine learning technologies become more sophisticated, photodetectors are increasingly being used in AI-driven systems to enable visual recognition and interpretation. In these applications, photodetectors provide the necessary data for algorithms to analyse images, detect patterns, and make intelligent decisions based on visual inputs. This capability is essential for applications in surveillance, facial recognition, gesture control, and even industrial robotics, where AI systems rely on visual data to perform tasks accurately.

The ongoing development of quantum computing and quantum communication also leverages the unique properties of photodetectors. In these cutting-edge technologies, photodetectors play a role in detecting single photons, which are used as quantum bits (qubits) for processing information. The ability to detect individual photons with high precision is critical for the advancement of quantum encryption techniques, which promise to revolutionise secure data transmission. As quantum technologies progress, photodetectors will remain at the forefront, enabling new capabilities in computing power and data security.

This chapter is started with the introduction of photodetectors after the introduction of III-V elements. Then, two main different kinds of photodetectors, photodiodes and avalanche photodiodes will be explained in detail. Thirdly, different III-V materials-based photodetectors will be presented. At the end of this chapter, an overview of this thesis will be given.

1.2 III-V elements

III-V elements refer to compounds formed by elements from group III (such as gallium (Ga), indium (In), and aluminium (Al)) and group V (such as nitrogen (N), arsenic (As), and phosphorus (P)) of the periodic table as shown in Table 1.1. These compounds, known as III-V semiconductors, have exceptional electronic and optoelectronic properties, making them highly valuable in advanced technological applications. Examples include gallium arsenide (GaAs), indium phosphide (InP), and gallium nitride (GaN).

Recent research on III-V materials has focused on enhancing their performance in various fields.

One major area of development is in the realm of high-speed and high-efficiency electronics, such as 5G communication systems and next-generation transistors. III-V semiconductors are seen as crucial for overcoming the limitations of traditional silicon in these applications.

Another exciting area is optoelectronics, where III-V compounds are widely used in light-emitting diodes (LEDs), laser diodes, and solar cells. GaN-based LEDs, for instance, are being refined for more efficient lighting and display technologies. In the past two decades, significant research has focused on incorporating elements such as Antimony (Sb) and bismuth (Bi) into III-V compounds, driven by the unique properties introduced by these additives. It is worth noting that a key finding is that doping Bi into these materials leads to a significant reduction in their bandgap[1] [2] .

III	IV	V
5 Be	6 C	7 N
13 Al	14 Si	15 P
31 Ga	32 Ge	33 As
49 In	50 Sn	51 Sb
81 Tl	82 Pb	83 Bi

Table 1.1 Group III, IV, and V of the periodic table

1.3 Photodetector

A photodetector is a key electronic device utilized for detecting light and transforming it into an electrical signal, enabling a wide variety of technological and scientific applications. This device operates based on the principle of the photoelectric effect, where incoming photons hit the surface of the photodetector, releasing charge carriers, electrons or holes, which then generate an electrical response. The power of the signal produced is proportional to the intensity of the incoming light, allowing for highly precise measurements of light levels.

There are several types of photodetectors, each suited to specific uses. Photodiodes (PDs) are one of the most common types, especially in optical communication systems and consumer electronics, generating current when exposed to light. They are valued for their fast response time and high sensitivity. Avalanche photodiodes (APDs) are designed to amplify weak light signals through an internal amplification mechanism, making them suitable for low-light conditions, such as in LIDAR systems and telecommunications. Details of PDs and APDs will be introduced in the next session. Phototransistors, similar to photodiodes, offer higher sensitivity and amplify the signal created by light exposure, making them ideal for low-light sensing applications. Photomultiplier tubes (PMTs) are highly sensitive detectors capable of detecting even single photons by amplifying the signal, normally from 10^5-10^8 times, from incident photons through electron multiplication [3] . PMTs are typically used in scientific research, medical imaging, astronomy, and nuclear detection, where detecting faint light sources is crucial. Additionally, charge-coupled devices (CCDs) and complementary metal-oxide-semiconductor (CMOS) sensors are widely used in digital cameras, medical imaging devices, and diagnostic equipment. These work by capturing light in an array of tiny photodetectors and converting it into an image signal.

The performance of a photodetector is determined by several key parameters that influence its efficiency and sensitivity. These include responsivity, which measures how effectively the device converts incident light into an electrical signal, and quantum efficiency, which represents the ratio of electrons generated to photons received. Dark current is the amount of current flowing in the absence of light, and lower dark current is preferred for reducing noise. The noise equivalent power (NEP) indicates the minimum detectable optical power, with lower NEP values signalling higher sensitivity. Response time or bandwidth is crucial for determining how quickly the detector can respond to changes in light intensity, impacting its suitability for high-speed applications. The dynamic range defines the range of light intensities the detector can handle without saturation, while linearity ensures that the output signal remains proportional to the input light intensity across this range.

Photodetectors are widely employed in various fields. In optical communication, they serve as the foundation for fibre-optic communication systems by converting light signals transmitted through fibres into electrical signals. Their high sensitivity and fast response make them indispensable for processing large data volumes in telecommunication infrastructure. In imaging, photodetectors are used in digital cameras and medical imaging devices like microscopes and telescopes to capture light and create high-resolution images. In environmental and industrial monitoring, photodetectors are used for tasks such as air quality monitoring, gas detection, and automation processes like motion detection and lighting control. LIDAR systems, which rely on photodetectors, are essential in applications such as autonomous vehicles and topographic mapping by measuring the time it takes for light to reflect back from objects. In medical diagnostics, photodetectors are crucial in equipment like CT (Computed Tomography) scanners, X-ray machines, and fluorescence microscopes for analysing light signals to aid in disease detection.

Despite their versatility, photodetectors do have limitations. Some photodetectors cannot directly measure non-radiative recombination in materials, which means they may not capture all energy losses within a system. Temperature sensitivity is another challenge, as photodetectors can experience performance degradation in extreme environmental conditions. Moreover, each type of photodetector is optimized for a specific range of wavelengths, limiting its effectiveness outside that spectral range unless modified.

In conclusion, photodetectors are indispensable in converting light into electrical signals and enabling a broad array of applications across telecommunications, medical imaging, environmental monitoring, and scientific research. Their precision, sensitivity, and adaptability to various wavelength ranges make them fundamental to modern technology.

1.4 Photodiodes and Avalanche photodiodes

A p-i-n photodiode is a specialized type of photodiode that features an intrinsic (i) layer sandwiched between the p-type and n-type semiconductor regions which is shown in Figure 1.1. This intrinsic layer enhances the device's performance by enlarging the depletion region where light absorption occurs. The primary function of a p-i-n photodiode is to convert incoming light into an electrical signal, making it essential in applications that require fast and efficient light detection, such as optical communication systems, laser rangefinders, and medical instruments.

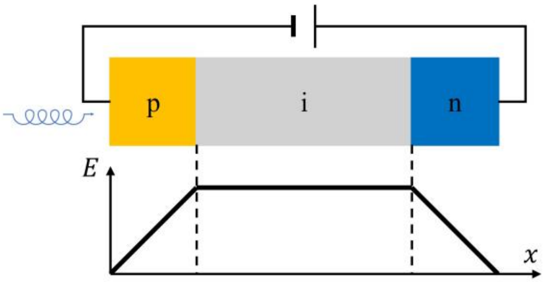

Figure 1.1 A typical p-i-n photodiode and its photogeneration profile under electric field.

When photons enter the p-i-n photodiode, they are absorbed in the intrinsic region, generating electron-hole pairs (charge carriers). The electric field across the intrinsic layer quickly separates these carriers, driving them toward the p and n regions, which results in a current that is proportional to the intensity of the incoming light. The intrinsic layer increases the width of the depletion region, leading to improved quantum efficiency and faster response times compared to standard photodiodes. Additionally, p-i-n photodiodes are valued for their low noise and linear response, which make them highly reliable for precision light detection.

An avalanche photodiode (APD) is an advanced photodiode that employs an internal gain mechanism to amplify the electrical signal generated by light. APDs operate at higher voltages, where the electric field in the depletion region is strong enough to cause impact ionization. As photons are absorbed in the depletion region, they generate electron-hole pairs. In an APD, these charge carriers gain sufficient energy from the electric field to create additional electron-hole pairs through collisions with the crystal lattice, resulting in a cascade or avalanche effect. This internal multiplication increases the photocurrent significantly, making APDs extremely sensitive to low-light conditions.

APDs are ideal for applications where detecting very weak signals is critical, such as LIDAR, high-speed optical communication, and medical imaging. The ability to amplify the signal internally, without external amplification circuits, makes APDs highly efficient. However, APDs also introduce higher noise levels due to the avalanche multiplication process and are more sensitive to temperature and voltage variations compared to p-i-n photodiodes. Despite these limitations, APDs are widely used in applications requiring high sensitivity and precision.

The most significant difference between p-i-n photodiodes and avalanche photodiodes lies in the presence of internal multiplication/gain M. While p-i-n photodiodes do not feature internal amplification, APDs multiply the photocurrent through the avalanche process, offering much higher sensitivity. This makes APDs well-suited for detecting very low light levels, while p-i-n photodiodes excel in applications where fast response and low noise are needed. Although APDs provide greater sensitivity, they typically introduce more noise due to the avalanche process, whereas p-i-n photodiodes offer more stable performance with lower noise. P-i-n photodiodes are often used in high-speed communication systems, while APDs are preferred in environments requiring extreme sensitivity, such as LIDAR and scientific imaging. Excess noise is a key problem in APDs because it comes from the stochastic impact ionization process. Impact ionization coefficients of electron (α) and holes (β) will be introduced in this process to express impact ionization. The impact ionization ratio (α/β) will affect the excess noise performance directly. For high-speed and high-sensitive APDs, large α/β ratio is needed to reduce the excess noise[4] [5] . In recent decades, a large amount of research has been invested in increasing and reducing excess noise. The first way to achieve low noise performance is to choose bulk materials with high electron hole impact ionization coefficient ratios, while initiating impact ionization processes through higher impact ionization carrier types[6] . The second solution to solve this problem is to reducing multiplication region due to the non–local property of impact ionization[7] [8] [9] [10] [11] [12] . The newest design is heterojunction and multilayer structures [13] [14] [15] [16] [17] .

1.5 III-V Materials

The performance of semiconductor devices is primarily influenced by the underlying physics of semiconductor materials. This section provides a literature review of avalanche materials. In 1966, optical fibre was first used for optical communication by Kao and Hockham[18] to prevent signal degradation caused by atmospheric interference. Initially, with the successful development of AlGaAs-based lasers, operating wavelengths ranged between 0.8 and 0.9 μm. As a result, GaAs (with a bandgap of 1.42 eV) and Si (with a bandgap of 1.12 eV) emerged as suitable materials for these wavelengths.

Silicon-based devices have come to dominate the market, largely due to their distinct ionization coefficients, low excess noise, unparalleled technological maturity, and cost-effectiveness. However, their main limitation is their reduced ability to detect near-infrared light. The driving force behind modern avalanche photodiodes (APDs) has been the development of next-generation Lightwave communication systems, which utilize the low-attenuation and low-dispersion wavelengths of 1.31 and 1.55 μm in silicon optical fibres.

To meet the demand for detecting longer wavelengths, researchers have recently incorporated germanium (Ge, with a bandgap of 0.67 eV) as an absorber material in silicon-based devices[19] [20] [21] . Although this approach addresses the wavelength requirement, it introduces a lattice mismatch issue, leading to a high dark current level (~10^{-5} A/cm^2), which reduces sensitivity.

With the successful growth of InAs/GaAs quantum dots on GaAs substrates[22] [23] and the growth of InGaAs nanopillars on GaAs substrates[24] , it is now possible to achieve optical detection at wavelengths of 1.31 and 1.55 μm on the GaAs platform as well. This breakthrough opens new possibilities for optical communication at longer wavelengths while leveraging the advantages of GaAs-based materials.

Mercury Cadmium Telluride (HgCdTe) avalanche photodiodes (APDs) with a bandgap of less than approximately 0.55 eV have been demonstrated ideal impact ionization properties, where the hole ionization coefficient is nearly zero at room temperature, resulting in a very low excess noise factor ranging between 1 and 1.5[25] [26] [27] . Despite these advantages, they are typically grown on small, costly substrates, making them primarily suited for high-end applications in the space and military sectors. The development of InAs APDs (with a bandgap of around 0.34 eV) has been driven by their similar band structure to HgCdTe. Interestingly, studies have shown that InAs APDs can achieve comparable performance to HgCdTe devices. Several research groups have reported excess noise values of $F < 2$ in both mesa and planar devices[28] [29] [30] [31] [32] . Additionally, room-temperature frequency response measurements have shown a high gain-bandwidth product of 580 GHz[33] . However, challenges such as high dark leakage current, expensive substrates, complex growth processes, and sensitivity to temperature continue to limit further advancement of InAs APDs.

The impact ionization coefficient and excess noise of $In_{0.53}Ga_{0.47}As$ grown on InP substrate have been reported by Ng J. et al in 2003[34] [35] . The $In_{0.53}Ga_{0.47}As$ is lattice matched on InP substrate and has become a preferred material for use in Separate Absorption and Multiplication (SAM) APDs as the absorption layer in telecommunication photodetectors. $In_{0.53}Ga_{0.47}As$ has a direct bandgap of approximately 0.75 eV at room temperature, making it highly effective at absorbing wavelengths up to 1.65 μm, which is ideal for telecommunication applications. However, InGaAs is not typically used as the avalanche region due to the high tunnelling current generated under strong electric fields. Fortunately, other semiconductor materials that can be grown lattice-matched on InP substrates offer alternatives for use in avalanche regions. In this thesis, AlInAsSb lattice-matched on InP substrate will be introduced.

Recently, X. Yi et al reported in 2018 that $AlAs_{0.56}Sb_{0.44}$ APDs have ionization coefficient ratio, and it is lattice matched with InP substrate[36] . One year later, he showed that this material has extremely low excess noise and high sensitivity and the β/α ratio, k , is as low as 0.005[37] . These works establish that $AlAs_{0.56}Sb_{0.44}$ is a leading material for next-generation avalanche photodiodes due to its unique impact ionization properties and its ability to significantly reduce excess noise while maintaining high sensitivity.

Also, the work done by Y. Liu et al in 2021 showed that incorporating Bi into the GaAs, significant changes can be made to the valence band structure of the material. Bismuth, being a larger atom with different electronegativity compared to arsenic, introduces perturbations in the valence band, which in turn affects the hole transport and impact ionization rates[38] . This modification leads to a reduction in the ionization coefficient for holes relative to electrons, which is crucial for achieving lower excess noise in APDs.

1.6 Motivation

Avalanche photodiodes (APDs) are essential optical components used to amplify weak light signals through the process of impact ionization. However, the randomness of this process introduces excess noise, which limits the achievable signal-to-noise ratio (SNR) or sensitivity in practical applications. The α/β ratio is a key parameter that can affect excess noise in this procedure. In recent deep research, people are looking for low dark current, large α/β ratio and low excess noise materials. Most III-V semiconductor materials have a small III-V α/β ratio like GaAs. However, it is possible to incorporate other III-V elements like Sb and Bi into the material like GaAs and AlInAs to increase α/β ratio and reduce excess noise. Also, there is no work reported on the impact ionization coefficient and excess noise on AlInAsSb structures and GaAs/GaAsBi MQW structure. Therefore, this work is aim for characterisation and understanding of the impact ionization coefficient and excess noise on $Al_{0.70}In_{0.30}As_{0.74}Sb_{0.26}$ and GaAs/GaAsBi MQW.

1.7 Thesis organisation

Chapter 1: Introduction of III-V elements and different kind of photodetectors. And III-V semiconductor materials APDs is a key photodetector.

Chapter 2: The background knowledge of PN junction, depletion width and diode equation. After that the background theory of light absorption, impact ionization coefficient and excess noise will be discussed.

Chapter 3: All the experimental techniques and equipment will be introduced for device processing and APD characterisation, including device fabrication, photoluminescence (PL), current-voltage (IV), capacitance-voltage (CV), photo spectral response, photo multiplication and excess noise.

Chapter 4: The detailed research on AlInAsSb p-i-n diode grown on InP substrate will be discussed in this chapter. The introduction will be separated into growth condition and device fabrication. These wafers are grown by OSU and the fabrication was done by OSU and also the University of Sheffield. The measurements include SIMS, IV, CV, bias–dependent spectral response and photo–multiplication. After that the impact ionization coefficient and excess noise will be reported.

Chapter 5: GaAsBi/GaAs multiple quantum well (MQW) p-i-n diodes grown on GaAs substrate will be present. The characteristic results will include not only SIMS, TEM, IV, CV but also XRD and PL, photo-spectral, photo-multiplication. Similar to chapter 4, the impact ionization coefficient of MQWs and excess noise will be discussed. And these results will be compared with Y. Liu's GaAsBi bulk samples.

Chapter 6: All the key results in this thesis will be summarized and the future work will be discussed.

1.8 References

[1] K. Oe and H. Okamoto, ‘New Semiconductor Alloy GaAs1-xBix Grown by Metal Organic Vapor Phase Epitaxy’, *Jpn. J. Appl. Phys.*, vol. 37, no. Part 2, No. 11A, pp. L1283–L1285, Nov. 1998, doi: 10.1143/JJAP.37.L1283.

[2] M. Weyers, M. Sato, and H. Ando, ‘Red Shift of Photoluminescence and Absorption in Dilute GaAsN Alloy Layers’, *Jpn. J. Appl. Phys.*, vol. 31, no. Part 2, No. 7A, pp. L853–L855, Jul. 1992, doi: 10.1143/JJAP.31.L853.

[3] "Photomultiplier Tubes: Basics and Application Third Edition," Hamamatsu Photonics K. K.

[4] R. B. Emmons, “Avalanche photodiode frequency response,” *J. Appl. Phys.*, vol. 38, no. 9, pp. 3705–3714, 1967.

[5] R.B. Emmons and G. Lucovsky, "The frequency response of avalanching photodiodes," *IEEE Trans. Electron Devices*, vol. 13, pp. 297-305, 1966.

[6] R. J. McIntyre, “Multiplication noise in avalanche photodiodes”, *IEEE Trans. Electron De-vices*, vol. 13, no. 1, pp. 164–168, Jan. 1966.

[7] M. M. Hayat, B. E. A. Saleh, and M. C. Teich, “Effect of dead space on gain and noise of double-carrier-multiplication avalanche photodiodes,” *IEEE Trans. Electron Devices*, vol. 39, no. 3, pp. 546–552, Mar. 1992.

[8] X.W. Li,X.G. Zheng, S. L.Wang, F. Ma, and J. C. Campbell, “Calculation of gain and noise with dead space for GaAs and AlxGa1-xAs avalanche photodiode,” *IEEE Trans. Electron Devices*, vol. 49, no. 7, pp. 1112–1117, Jul. 2002.

[9] [1] J. C. Campbell, S. Chandrasekhar, W. T. Tsang, G. J. Qua, and B. C. Johnson, “Multiplication noise of wide-bandwidth InP/InGaAsP/InGaAs Avalanche Photodiodes,” *Journal of Lightwave Technology*, vol. 7, no. 3, pp. 473–478, Mar. 1989. doi:10.1109/50.16883.

[10] P. Yuan et al., “Impact ionization characteristics of III-V semiconductors for a wide range of multiplication region thicknesses,” *IEEE J. Quantum Electron*, vol. 36, no. 2, pp. 198–204, Feb. 2000.

[11] M. A. Saleh et al., “Impact-ionization and noise characteristics of thin III–V avalanche photodiodes,” *IEEE Trans. Electron Devices*, vol. 48, no. 12, pp. 2722–2731, Dec. 2001.
[12] P. Yuan et al., “A new look at impact ionization—Part II: Gain and noise in short avalanche photodiodes,” *IEEE Trans. Electron Devices*, vol. 46, no. 8, pp. 1632–1639, Aug. 1999.
[13] P. Yuan, S. Wang, X. Sun, X. G. Zheng, A. L. Holmes, and J. C. Campbell, “Avalanche photodiodes with an impact-ionization-engineered multiplication region,” *IEEE Photon. Technol. Lett.*, vol. 12, no. 10, pp. 1370–1372, Oct. 2000.
[14] O. H. Kwon et al., “Optimal excess noise reduction in thin heterojunction Al0.6Ga0.4 As-GaAs avalanche photodiodes,” *IEEE J. Quantum Electron*, vol. 39, no. 10, pp. 1287–1296, Oct. 2003.
[15] M.M. Hayat, O.H. Kwon, S.L. Wang, J.C. Campbell, B.E. A. Saleh, and M.C. Teich, “Boundary effects on multiplication noise in thin heterostructure avalanche photodiodes: Theory and experiment,” IEEE Trans. Electron Devices, vol. 49, no. 12, pp. 2114–2123, Dec. 2002.
[16] S. Wang et al., “Low-noise impact-ionization-engineered avalanche photodiodes grown on InP substrates,” *IEEE Photon. Technol. Lett.*, vol. 14, no. 12, pp. 1722–1724, Dec. 2002.
[17] N. Duan et al., “High-speed and low-noise SACM avalanche photodiodes with an impact-ionization-engineered multiplication region,” *IEEE Photon. Technol. Lett.*, vol. 17, no. 8, pp. 1719–1721, Aug. 2005.
[18] K. C. Kao and G. A. Hockham, “Dielectric-fibre surface waveguides for optical frequencies”, *Proc. Institution Elect. Engineers*, vol. 113, no. 7, pp. 1151–1158, Jul. 1966. doi.org/10.1049/piee.1966.0189
[19] D. D. Cannon et al., “Tensile strained epitaxial Ge films on Si(100) substrates with potential application in L-band telecommunications”, *Appl. Phys. Lett.*, vol. 84, no. 6, pp. 906–908, Feb. 2004. doi.org/10.1063/1.1645677
[20] G. Dehlinger and S.J. Koester and J. D. Schaub and J. O. Chu and Q.C. Ouyang and A. Grill, “High-Speed Germanium-on-SOI Lateral PIN photodiodes,” *IEEE Photon. Technol. Lett.* 16, 2547-2549 (2004).

[21] J. Liu, J. Michel, W. Giziewicz, D. Pan, K. Wada, D. Cannon, L.C. Kimerling, J. Chen, F. O. Ilday, F. X. Kartner and J. Yasaitis, “High-performance, tensile-strained Ge p-i-n photode-tectors on a Si platform,” *Appl. Phys. Lett.* 87, 103501 (2005).

[22] S. Sauvage, P. Boucaud, J.M. Gerard, and V. Thierry-Mieg, “In-plane polarized intraband absorption in InAs/GaAs self-assembled quantum dots,” *Phys. Rev. B*, vol. 58, pp. 10562-10567, Oct. 1998.

[23] D. Huffaker and D. Deppe, “A quantum leap in laser emission,” *IEEE Circuit & Devices*, vol. 15, pp. 8-13, May 1999.

[24] A.C. Farrell et al. “Plasmonic field confinement for separate absorption -multiplication in InGaAs nanopillar avalanche photodiodes,” *Scientific Reports*, vol. 5, pp. 17580, 2015.

[25] J.D. Beck, C-F. Wan, M.A. Kinch, J.E. Robinsonl, “MWIR HgCdTe avalanche photodiodes,” Proc. SPIE, *Materials for Infrared Detectors*, vol. 4454, pp. 188-197, 2001.

[26] J. Beck, C. Wan, M. Kinch, J. Robinson, P. Mitra, R. Scritchfield, F. Ma and J. Campbell, “The HgCdTe electron avalanche photodiode,” *J. Electronic Materials*, vol. 35, no. 6, pp. 1166-1173, 2006.

[27] X. Sun, J.B. Abshire, J.D. Beck, P. Mitra, K. Reiff and G. Yang, “HgCdTe avalanche photodiode detectors for airborne and spaceborne lidar at infrared wavelengths,” *Opt. Exp.*, Vol. 25, No. 14, Jul. 2017.

[28] P.J. Ker, J.P.R. David and C.H. Tan, “Temperature dependence of gain and excess noise in InAs electron avalanche photodiodes,” *Opt. Exp.*, Vol. 20, Iss. 28, Dec. 2012.

[29] P.J. Ker, A.R.J. Marshall, J.P.R. David and C.H. Tan, “Low noise high responsivity InAs electron avalanche photodiodes for infrared sensing,” *Phys. Status Solidi C*, No. 2, Dec. 2011.

[30] P.J. Ker, A.R.J. Marshall, A.B. Krysa, J.P.R. David and C.H. Tan, “Temperature Dependence of Leakage Current in InAs Avalanche Photodiodes,” *IEEE J. Quantum Electron.*, Vol. 47, No. 8, Aug. 2011.

[31] A.R.J. Marshall, J.P.R. David, and C.H. Tan, “Impact Ionization in InAs Electron Avalanche Photodiode,” IEEE Trans. Electron Devices, Vol. 57, No. 10, Oct. 2010.

[32] B.S. White, I.C. Sandall, X. Zhou, A. Krysa, K. McEwan, J.P.R. David and C.H. Tan, “High-gain InAs planar avalanche photodiode,” *Journal of Lightwave Technology*, Vol. 34, No. 11, Jun. 2016.

[33] A.R.J. Marshal, P.J. Ker, A. krysa, J.P.R. David and C.H. Tan, “High speed InAs electron avalanche photodiodes overcome the conventional gain-bandwidth product limit,” *Opt. Exp.*, Vol. 19, No. 23, pp. 23341-23349, Nov.2011

[34] J.S. NG, C. H. Tan, J.P.R. David, G. Hill, and G.J. Rees, “Field dependence of InGaAs impact ionization coefficients,” *IEEE Trans. Electron Devices*, vol. 50, no. 4, pp. 901–905, Apr. 2003.

[35] J.S. Ng, C.H. Tan, J.P.R. David and G.J. Rees, “Effect of impact ionization in the InGaAs Absorber on excess noise of avalanche photodiodes” *IEEE Journal of Quan. Elec.*, Vol. 41, No. 8, pp. 1092-1096, Aug. 2005.

[36] X. Yi et al., “Demonstration of large ionization coefficient ratio in AlAs0.56Sb0.44 lattice matched to InP,” *Scientific Reports*, vol. 8, no. 1, Jun. 2018. doi:10.1038/s41598-018-27507-w.

[37] X. Yi et al., “Extremely low excess noise and high sensitivity AlAs0.56Sb0.44 avalanche photodiodes”, *Nature Photon.*, vol. 13, no. 10, pp. 683–686, Jul. 2019. doi.org/10.1038/s41566-019-0477-4.

[38] Y. Liu et al., “Valence band engineering of GaAsBi for low noise avalanche photodiodes”, *Nature Communication.*, vol. 12, no. 1, Aug. 2021. doi.org/10.1038/s41467-021-24966-0

2. CHAPTER 2: Background Theory

2.1 PN junction

A PN junction is a crucial component in semiconductor devices, created by combining two types of semiconductor materials: p-type and n-type as shown in Figure 2.1. E_c and E_v are the conduction band and valance band respectively. The majority carriers in p-type semiconductor are holes J_{hp}, while the n-type semiconductor has majority carrier of electrons J_{en}. The majority carriers form diffusion current. In the meanwhile, the minority carriers, holes in n–type J_{hn} and electrons in p–type J_{ep}, contribute to drift current. The interface where these two materials meet is called the junction.

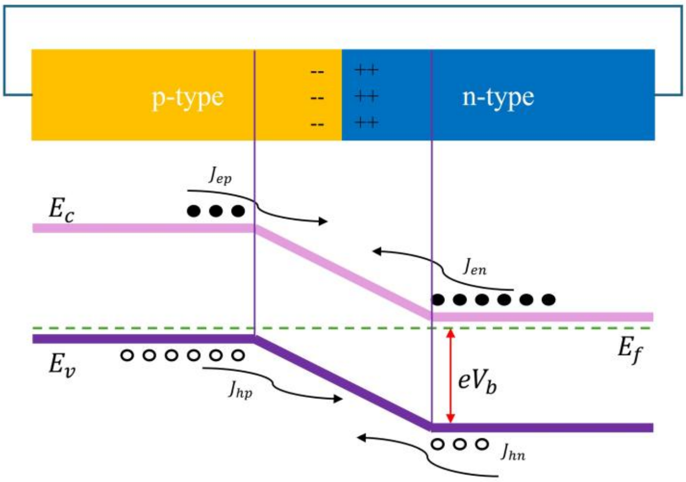

Figure 2.1 PN junction under zero bias.

When the PN junction is formed, electrons from the n-type region begin to diffuse into the p-type region, while holes from the p-type region diffuse into the n-type region. This process leads to the creation of a region near the junction known as the depletion region, where free carriers (electrons and holes) are depleted. As a result of this diffusion, the depletion region becomes populated with immobile ions, negatively charged in the p-region and positively charged in the n-region, leading to the formation of an electric field that opposes further carrier movement and establishes equilibrium.

This built-in electric field across the depletion region plays a crucial role in the junction's behaviour. Under different conditions, the PN junction behaves differently. In forward bias in Figure 2.2, when a positive voltage is applied to the p-type side and a negative voltage to the n-type side, the external voltage decreases the width of the depletion region, enabling current to flow across the junction. This is how diodes conduct electricity in one direction. In contrast, under reverse bias in Figure 2.3, when the p-type side is connected to the negative terminal while the n-type side to the positive, the depletion region widens, preventing significant current flow. In this case, only a small leakage current flows due to minority carriers.

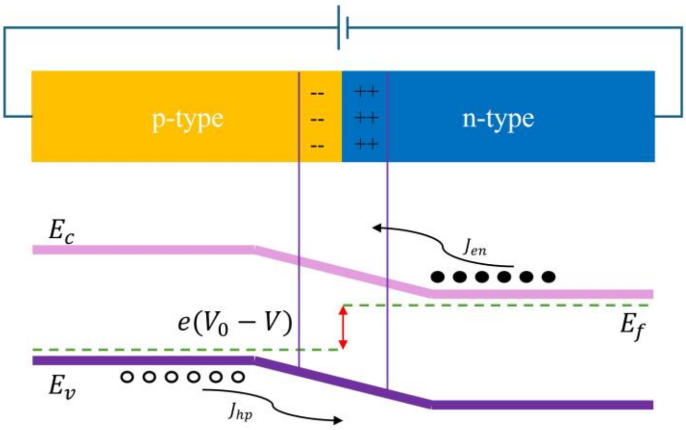

Figure 2.2 PN junction under forward bias

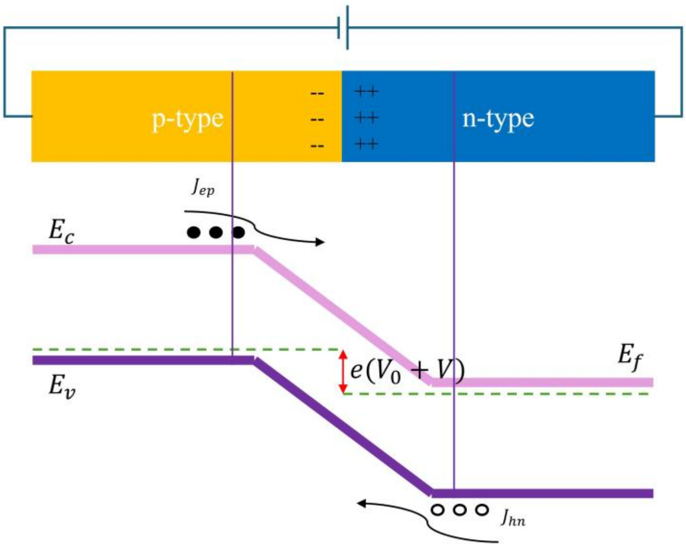

Figure 2.3 PN junction under reverse bias

The PN junction is the foundation of various semiconductor devices. Diodes use it to allow current to pass in only one direction. Photodetectors rely on the PN junction to convert light into an electrical signal. Solar cells use it to transform sunlight into electricity, and transistors, which are essential for amplifying or switching signals, are built upon this structure.

2.2 Diode equation

The diode equation, often referred to as the Shockley equation, is a key formula that defines the current-voltage (I-V) relationship of a p-n junction diode. Named after William Shockley, a co-inventor of the transistor, this equation is crucial for comprehending the operation of semiconductor devices such as diodes. It explains how current flows through a diode based on the applied voltage, accounting for its behaviour in both forward and reverse bias conditions.

The basic form of the Shockley equation is:[1] [2]

$$I = I_s\left(e^{\frac{qV}{nkT}} - 1\right) \tag{2.1}$$

where I is the current flowing through the diode, I_s is the reverse saturation current, q is the electron charge (1.6×10^{-19}), V is the voltage across the diode, n is the ideality factor, k is the Boltzmann constant (1.38×10^{-23}) and T is the absolute temperature in kelvins.

The reverse saturation current, I_s , is the small current that flows through a diode when it is reverse biased, caused by the diffusion of minority carriers—electrons in the p-type region and holes in the n-type region—across the depletion region. While I_s is typically very small, it is a crucial parameter in the Shockley equation. This current is highly sensitive to temperature, increasing exponentially with rising temperatures. Additionally, its value depends on the materials and physical dimensions of the diode.

At room temperature (300K), the thermal voltage $V_T = \frac{kT}{q}$ is approximately 26 millivolts. Thermal voltage reflects the impact of temperature on the motion of charge carriers within the semiconductor material. At higher temperatures, the kinetic energy of carriers increases, affecting the diode's behavior and influencing the current flow.

The ideality factor, n, also known as the emission coefficient, typically higher than 1, depending on the material and manufacturing process of the diode. It accounts for recombination processes in the depletion region. When $n = 1$, the current is primarily dominated by carrier diffusion across the depletion region, indicating ideal diode behavior. However, when carrier recombination becomes significant, n can approach values closer to 2. This factor is critical in determining how closely the real behavior of a diode matches that of an ideal one. When the ideality factor $n > 2$, it suggests the presence of Auger recombination, which dominates at high carrier injection levels and contributes to efficiency droop in LEDs [3] . Additionally, non-ideal effects such as carrier leakage, series resistance, tunneling, or interface defects can further increase n, leading to deviations from ideal recombination mechanisms[4] .

When a diode is forward biased in Figure 2.2, the depletion region narrows, allowing charge carriers to flow more easily across the junction. In this condition, the Shockley equation shows that the current increases exponentially as the voltage rises. The term $e^{\frac{qV}{nkT}}$ grows significantly with increased voltage, leading to a rapid rise in current. At small forward voltages, the -1 term in the Shockley equation ensures that no current flows when no voltage is applied.
The diode equation can be simplified as:

$$I = I_s\left(e^{\frac{qV}{nkT}}\right) \tag{2.2}$$

As the forward voltage exceeds a threshold, which is called turn voltage (typically around 0.7 V for Si and 0.3 V for Ge diodes), the exponential term dominates, and current rises sharply, making the diode function as a switch that conducts current in forward bias while blocking it in reverse bias.

In reverse bias in Figure 2.3, which widens the depletion region and prevents the majority carriers from flowing across the junction. Here, the Shockley equation shows that the current is nearly constant, equalling the reverse saturation current I. The term $e^{\frac{qV}{nkT}}$ becomes negligible in reverse bias because the exponent is negative, reducing the value close to zero. The equation simplifies to $I \approx I_S$, meaning only a small leakage current flows regardless of the applied reverse voltage. However, in some diodes, if the reverse voltage exceeds a critical level known as the breakdown voltage, the diode can enter avalanche or Zener breakdown, where the current increases rapidly, but the Shockley equation no longer applies, as other factors govern the diode's behaviour in this region.

The diode equation is grounded in the physics of carrier diffusion and recombination in a p-n junction. When a voltage is applied, the electric field in the depletion region either strengthens in reverse bias or weakens in forward bias. In forward bias, the weakened electric field allows electrons from the n-type region and holes from the p-type region to diffuse into the depletion region, generating current. The exponential form of the Shockley equation reflects the Boltzmann distribution of carrier energies in the semiconductor. In reverse bias, the strong electric field in the depletion region sweeps minority carriers across the junction, resulting in the small, constant reverse saturation current I_S. This small current flows because the number of thermally generated minority carriers is limited, and the diode effectively blocks the flow of majority carriers.

2.3 Absorption of light

The absorption of light in semiconductors is a critical process that underpins many of the technologies we use today, from solar cells and photodetectors to light-emitting diodes (LEDs) and lasers. When light interacts with a semiconductor material, it can excite electrons from the valence band, where they are bound to atoms, to the conduction band, where they are free to move and contribute to electrical conduction. This transition, which requires the absorption of energy, is made possible by photons, the basic particles of light. For a photon to be absorbed by a semiconductor, its energy must be equal to or greater than the semiconductor's bandgap energy, the energy difference between the valence band and the conduction band. This fundamental interaction lies at the heart of how semiconductors convert light into electrical signals or use electrical energy to emit light. The relationship between photon energy E and the wavelength of light λ is:

$$\lambda = \frac{hc}{E} = \frac{hc}{E_g} \approx \frac{1.24}{E_g} \tag{2.3}$$

where h refers to Planck's constant ($4.13 \times 10^{-15}\ eV \cdot s$), c is the speed of light ($3 \times 10^{8}\ m/s$) and E_g is the bandgap of the semiconductor. λ also refers to the cut off wavelength of this material.

In semiconductors, the bandgap energy determines the range of photon energies the material can absorb. Photons with energy lower than the bandgap pass through the material without being absorbed, as there is not enough energy to excite electrons across the bandgap. Conversely, photons with energy higher than or equal to the bandgap are absorbed, exciting electrons from the valence band to the conduction band. This excitation process creates electron-hole pairs: the electron moves to the conduction band, leaving behind a "hole" in the valence band, which behaves like a positive charge carrier. The presence of these free electrons and holes is what allows the semiconductor to conduct electricity in response to light, a principle that is exploited in devices like solar cells and photodetectors.

The absorption of light in a semiconductor is governed by several factors, including the material's absorption coefficient (γ), the thickness of the material, and the wavelength of the incoming light. The absorption coefficient is a material property that indicates how effectively a semiconductor can absorb light of a specific wavelength. The intensity of light φ can be expressed by:

$$\varphi = \varphi_0 e^{-\gamma x} \tag{2.4}$$

Where φ_0 is the original light intensity of the light and x defines the distance light travels.
A higher absorption coefficient means the material is more efficient at capturing photons and converting their energy into electron-hole pairs. This coefficient depends on the energy of the photons relative to the semiconductor's bandgap: photons with energies close to the bandgap are often absorbed less efficiently than those with much higher energy, because they may not have enough energy to fully excite an electron into the conduction band or may only partially penetrate the material before being absorbed.

In addition to the absorption coefficient, the thickness of the semiconductor material also plays a role in the absorption of light. Thicker materials have a greater chance of interacting with photons because the light must travel a longer distance through the material. This increases the probability that photons will be absorbed rather than passing through the material without interaction. In thin semiconductor films, absorption may be less efficient simply because there is less material to interact with the incoming light. This is why many solar cells and photodetectors are designed with layers of semiconductor material that are thick enough to absorb most of the incident light, but not so thick that they become impractical to manufacture or inefficient due to increased material costs or weight.

The wavelength of the incoming light is another important factor in the absorption process. Light consists of a spectrum of wavelengths, and different wavelengths carry different amounts of energy. Shorter wavelengths, such as ultraviolet light, have higher energy photons, while longer wavelengths, like infrared light, have lower energy photons. The absorption of light in a semiconductor is wavelength-dependent: only photons with energies matching or exceeding the semiconductor's bandgap can be absorbed. For example, silicon, with a bandgap of about 1.1 eV, can absorb visible light and some near-infrared light, but it does not efficiently absorb photons with energies lower than 1.1 eV, such as those in the mid- to far-infrared range.

In the context of solar cells, the absorption of light is a key mechanism for converting sunlight into electricity. When sunlight strikes the surface of a solar cell, photons with sufficient energy are absorbed, creating electron-hole pairs. These charge carriers are then separated by an internal electric field and collected at electrodes, generating an electric current. The efficiency of a solar cell largely depends on its ability to absorb a broad spectrum of sunlight, particularly in the visible and near-infrared ranges where most solar energy is concentrated. Semiconductor materials used in solar cells, such as silicon or CdTe, are selected for their bandgap properties, which must be optimized to capture as much of the solar spectrum as possible while minimizing energy losses due to unabsorbed photons or excessive thermalization of carriers.

In photodetectors, the absorption of light allows for the detection of optical signals by converting them into electrical signals. Photodetectors rely on the creation of electron-hole pairs when light is absorbed, and the subsequent collection of these carriers generates a current that corresponds to the intensity of the light. Different types of photodetectors, such as p-n junction photodiodes or avalanche photodiodes (APDs), are designed to be sensitive to specific wavelengths of light, based on the bandgap of the semiconductor material used. For example, indium gallium arsenide (InGaAs) photodetectors are often used for near-infrared light detection due to their narrow bandgap, which allows them to absorb photons in this range effectively.

In light-emitting diodes (LEDs), the process of light absorption is reversed. Here, electrons are injected into the conduction band, where they recombine with holes in the valence band, emitting photons in the process. The energy of the emitted photons corresponds to the bandgap energy of the semiconductor, which determines the colour of the light. By carefully selecting the semiconductor material, manufacturers can design LEDs that emit light at specific wavelengths, from infrared to ultraviolet, making LEDs versatile for a wide range of applications, including displays, lighting, and communication systems.

In semiconductor lasers, the absorption of light is also integral to their operation, but in a more controlled manner. A laser diode, like an LED, relies on the recombination of electrons and holes, but it also requires a process called stimulated emission to produce coherent light. In this process, an incoming photon with energy matching the bandgap of the semiconductor can stimulate the recombination of an electron and a hole, releasing another photon with the same energy and phase. This chain reaction amplifies the light, producing the highly focused and intense beam characteristic of lasers. Semiconductor lasers are used in applications ranging from optical communications to medical devices.

The temperature of the semiconductor material can also affect light absorption. As the temperature of a semiconductor increases, its bandgap tends to shrink, allowing it to absorb longer wavelengths of light. However, higher temperatures can also increase the likelihood of non-radiative recombination events, where electron-hole pairs recombine without emitting light, thus reducing the efficiency of devices such as solar cells and LEDs. Managing temperature and minimizing heat generation are important considerations in designing semiconductor devices for optimal light absorption and emission.

In summary, the absorption of light in semiconductors is a complex and multifaceted process that plays a crucial role in the operation of a wide variety of electronic and optoelectronic devices. From converting sunlight into electricity in solar cells to detecting and emitting light in photodetectors and LEDs, the ability of semiconductors to absorb light and create charge carriers is fundamental to their function. The efficiency of this process depends on factors such as the bandgap of the material, the absorption coefficient, the thickness of the material, and the wavelength of the incoming light. Understanding these interactions is key to optimizing the performance of semiconductor devices in both everyday technology and advanced scientific applications.

2.4 Valence band Anti-crossing model

The Valence Band Anti-Crossing (VBAC) model explains how the incorporation of certain elements, such as nitrogen or bismuth, into a semiconductor material can drastically alter its electronic band structure. In GaAs, incorporating N or Bi will lead to significant mismatch because of the obvious ionic size difference. The ionic radius of N(V) is 27pm and for Bi(V) is 90pm while the ionic radius of As(V) is 60pm [5] . In particular, this model describes the interaction between the localized impurity states (introduced by N or Bi) and the extended states of the host semiconductor's valence band. This interaction leads to the formation of new energy levels, creating band splitting and reducing the bandgap, which has important implications for designing semiconductors with tailored electronic and optical properties.[6]

In compounds like GaAsBi, the anti-crossing interaction between the Bi-related states and the valence band of GaAs significantly modifies the valence band structure. This model is essential in understanding how small amounts of Bi can be used to fine-tune the bandgap and electronic properties, which is particularly useful in infrared applications and optoelectronics, such as lasers and detectors operating at long wavelengths. The energy of sub band E is given by Mohmad[7] below:

$$E_{\pm}(GaAsBi) = \frac{E_v(GaAs) - E_{Bi} \pm \sqrt{(E_v(GaAs) - E_{Bi})^2 + 4xC_{Bi}^2}}{2} \quad (2.5)$$

$$E_v(GaAs) = -\frac{\hbar^2 k^2}{2m^*} \quad (2.6)$$

where $E_v(GaAs)$ is the valence band maximum energy for GaAs, E_{Bi} is the Bi-level energy, x is the Bi fraction, $C_{Bi}$is the coupling between the Bi level and the GaAs valence band maximum energy, $\hbar$ is the Planck constant, k is the momentum and m^* is the effective mass of hole.

2.5 Avalanche multiplication and Impact ionization coefficient

Avalanche multiplication is a process that occurs in semiconductor devices, such as APDs, where free carriers (electrons or holes) in a high-electric-field region undergo successive impact ionization events, leading to an exponential increase in the number of carriers. This phenomenon is critical for devices that require high sensitivity, such as in optical communication systems, as it allows for the amplification of weak electrical signals.

The process begins when a primary carrier, often referred to as a "cold" carrier, is injected into a region of high electric field, typically at the depletion region of a semiconductor device. In this region, the carrier is accelerated by the electric field and gains energy as it moves. However, this energy gain is gradual due to the energy losses caused by scattering events, particularly phonon scattering. When the carrier accumulates enough energy, it can collide with an atom in the lattice, causing a secondary ionization event. This event generates an additional free electron-hole pair.

Each of these newly created carriers is also subject to the electric field and can undergo the same process, causing further impact ionization. This chain reaction of ionization events is referred to as avalanche multiplication. The injected primary carrier initiates the process, but as the number of ionized carriers increases exponentially, the current within the device is multiplied significantly, leading to a current multiplication factor, denoted by M.

Avalanche multiplication is inherently statistical in nature. The path length a carrier travels before undergoing ionization, known as the ionization path length, is random, as is the position where secondary carriers are generated. As a result, the overall multiplication process exhibits fluctuations. These fluctuations can lead to variations in the number of carriers generated from one instance of the process to another, contributing to noise in the system. This noise is known as excess noise, and it affects the performance of devices like APDs. The higher the fluctuations in the multiplication factor, the greater the excess noise, which can degrade the sensitivity of the device.

To quantify this process, a key parameter called the gain M is used. The expected value of the multiplication gain is denoted by $\langle M \rangle$, while the randomness of the gain is expressed by a random variable M_{ind} . Devices designed to operate with lower excess noise tend to have more controlled impact ionization processes and a smaller variance in the gain.

The avalanche multiplication process is particularly sensitive to the semiconductor material and device structure. In some materials, the ionization coefficients for electrons and holes differ, affecting the behaviour of the avalanche. For instance, in materials where electrons ionize more readily than holes, the multiplication factor M and its associated noise characteristics will differ from those of a material where the two carriers ionize at similar rates.

Avalanche multiplication ends when the carriers exit the high-field region, either at the boundaries of the depletion region or when they lose energy through other mechanisms. This entire process is fundamental to the operation of APDs and other high-gain semiconductor devices, as it allows for the detection of low-intensity signals by amplifying the current generated from a small number of primary carriers.

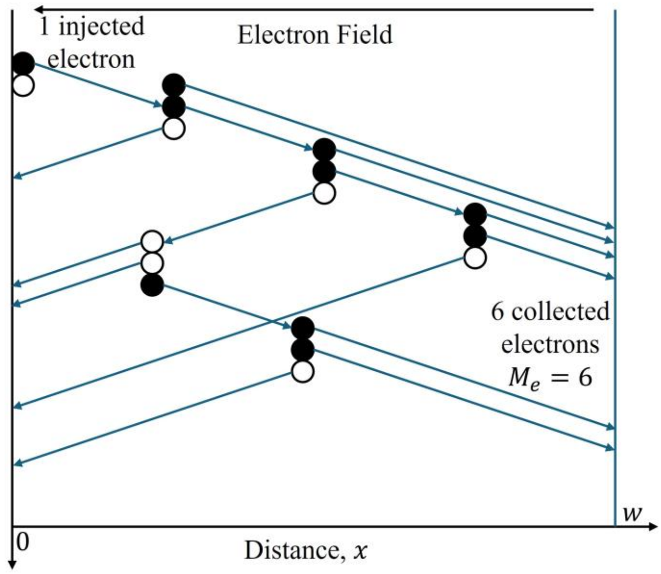

Figure 2.4 Avalanche multiplication process, 1 injected electron hole pair can resluts 6 electrons in the end. In this case $M_e = 6$.

In semiconductors, when a strong electric field is applied across a device, free electrons and holes are accelerated by this field. As these carriers move faster and gain more energy, they can eventually collide with atoms in the semiconductor lattice with enough force to ionise them, knocking additional electrons from the valence band into the conduction band. This process generates electron-hole pairs and thus increases the number of free carriers in the material. The newly created electrons and holes are also accelerated by the electric field, and they may in turn collide with other atoms, creating further ionisation as shown in Figure 2.4. This avalanche effect, resulting from a chain reaction of impact ionisation events, is the basis of the carrier multiplication process in devices such as avalanche photodiodes. With one electron injected, six electron go out of electric field while 5 holes go out. In this case, $M_e = 6$ and holes are called noise.

Stillman and Wolfe[8] derived an analytical expression for the mean multiplication factor by analysing the current continuity equation for primary carriers generated within the region www. They assumed that the ionization probability of the carriers depends solely on the local electric field. The mean multiplication factor at a position x, $M(x)$, is given by the following expression:

$$M(x) = \frac{\exp\left[-\int_x^w \alpha(x') - \beta(x')dx'\right]}{1 - \int_x^w \alpha(x')exp\left[-\int_{x'}^w \alpha(x'') - \beta(x'')dx''\right]dx'} \qquad (2.7)$$

When the electron is injected at $x = 0$, it can be written as:

$$M(0) = \frac{1}{1 - \int_0^w \alpha(x')exp\left[-\int_0^x \alpha(x'') - \beta(x'')dx''\right]dx'} \qquad (2.8)$$

When the hole is injected at $x = w$, it can be written as:

$$M(w) = \frac{1}{1 - \int_0^w \alpha(x')exp\left[-\int_x^w \alpha(x'') - \beta(x'')dx''\right]dx'} \qquad (2.9)$$

Assuming the high field is uniform, these two equation can be written as:

$$M_e = \frac{1}{1 - \frac{\alpha}{\alpha - \beta}\{exp[(\beta - \alpha)w] - 1\}} \qquad (2.10)$$

$$M_h = \frac{1}{1 - \frac{\beta}{\beta - \alpha}\{exp[(\alpha - \beta)w] - 1\}} \qquad (2.11)$$

Impact ionization coefficient is one of the most significant parameter of semiconductor devices, particularly in APDs. It describes the rate at which charge carriers, electrons and holes, gain enough kinetic energy under the influence of a strong electric field to cause additional ionization of atoms within the semiconductor lattice. This phenomenon is integral to many devices where multiplication of carriers is necessary for enhanced performance, such as in the detection of low-light signals or in voltage regulation circuits. Understanding the role of the impact ionization coefficient is crucial for the design and optimisation of these semiconductor devices, as it directly affects the performance, efficiency, and stability of the systems in which they are used.

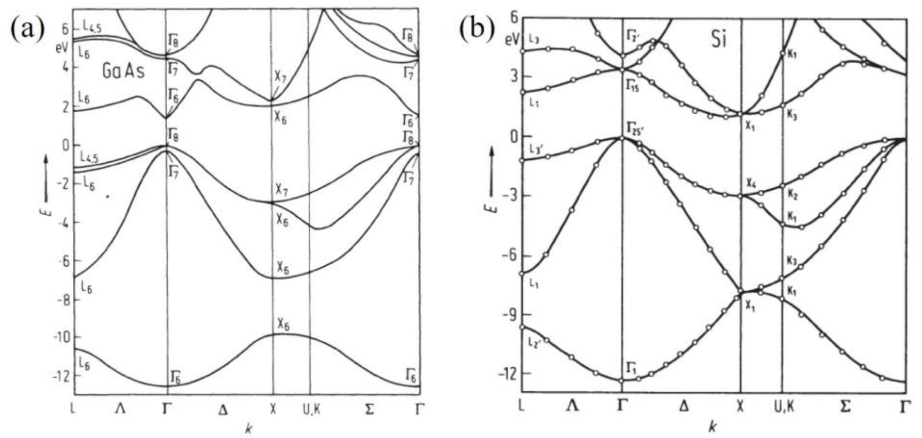

Figure 2.5 Band structure of (a) GaAs and (b) Si [1]

Figure 2.5 shows the electronic band structures of GaAs (a) and Si (b). The energy dispersion E_k is plotted along high-symmetry directions in the Brillouin zone. GaAs has a direct band gap at Γ, while Si has an indirect band gap between Γ and X.

The impact ionisation coefficient (α for electrons and β for holes) quantifies the probability of impact ionisation occurring per unit distance travelled by a charge carrier in the electric field. In essence, the coefficients α and β describe the likelihood that an electron and a hole, respectively, will create additional charge carriers as it moves through the semiconductor. These coefficients are strongly dependent on the strength of the electric field, the material properties of the semiconductor, and the temperature. They can be expressed using Chynoweth equations as:[9]

$$\alpha = A_n e^{-\left(\frac{B_n}{E}\right)^{C_n}} \tag{2.12}$$

$$\beta = A_p e^{-\left(\frac{B_p}{E}\right)^{C_p}} \tag{2.13}$$

where A_n, B_n and C_n are empirical coefficients for electrons while A_p, B_p and C_p for holes.

As the electric field increases, the kinetic energy of the carriers also increases, leading to a higher probability of impact ionisation and thus higher values of α/β. The impact ionisation coefficients vary significantly between different semiconductor materials, depending on their bandgap energy, lattice structure, and carrier mobility. For example, materials with a smaller bandgap, such as silicon or germanium, tend to have higher impact ionisation coefficients because electrons require less energy to move from the valence band to the conduction band. In contrast, wide-bandgap semiconductors like GaN or SiGe require higher energy levels for impact ionisation to occur, which means their ionisation coefficients are typically lower under the same electric field conditions. This characteristic makes wide-bandgap semiconductors ideal for high-power and high-voltage applications, where avalanche breakdown and carrier multiplication are undesirable, while materials with higher ionisation coefficients are more suited for devices that rely on these effects, such as APDs.

The temperature also plays a critical role in determining the impact ionisation coefficient. As the temperature increases, the thermal energy of the charge carriers increases as well, leading to more frequent collisions with atoms in the lattice. However, higher temperatures also introduce more scattering events that dissipate the carriers' energy before they can cause ionisation. Therefore, at elevated temperatures, the probability of impact ionisation may actually decrease, leading to lower ionisation coefficients. This temperature dependence must be carefully considered when designing semiconductor devices that operate in environments with fluctuating or high temperatures, such as in automotive or industrial applications.

In avalanche photodiodes (APDs), impact ionisation is a deliberate and controlled process used to achieve carrier multiplication, which enhances the sensitivity of the device. APDs are commonly used in applications where detecting very weak optical signals is essential, such as in fibre optic communications, LIDAR systems, and scientific instrumentation. When light enters the APD, it generates electron-hole pairs in the absorption region of the device. These carriers are then accelerated by the electric field in the multiplication region, where impact ionisation occurs. The resulting avalanche effect produces many more carriers than were initially generated by the absorbed photons, amplifying the signal and allowing the device to detect extremely low light levels. The performance of an APD is directly related to the impact ionisation coefficients of the material from which it is made. Materials with high ionisation coefficients enable efficient multiplication with lower excess noise, improving the overall sensitivity and signal-to-noise ratio of the device.

The ratio of the electron and hole ionisation coefficients, α/β, is a crucial factor in determining the performance of APDs. Ideally, a large disparity between the two coefficients is desirable because it reduces the excess noise associated with random fluctuations in the multiplication process. In materials where the electron ionisation coefficient is much larger than the hole ionisation coefficient, such as in silicon, electron-initiated multiplication dominates, leading to lower noise levels and more predictable behaviour. This is why silicon is often the material of choice for APDs in many applications, despite the availability of other semiconductors with similar or even superior properties for other aspects of photodetection.

In APDs, impact ionisation is also a critical process, although it is typically an undesirable effect in standard p-n junction diodes unless these devices are specifically designed to operate in the breakdown region. In a reverse-biased p-n junction, if the reverse voltage exceeds a certain threshold known as the breakdown voltage, the electric field in the depletion region becomes strong enough to induce impact ionisation. This results in a sharp increase in current, which can damage the device if it is not designed to handle such conditions. However, in APDs, this breakdown behaviour is harnessed for voltage regulation. These diodes are designed to operate in the breakdown region in a stable manner, with the impact ionisation process providing a controlled mechanism for limiting voltage in power supply circuits.

The modelling and simulation of impact ionisation coefficients are complex due to their dependence on various factors, such as the electric field distribution, carrier dynamics, and material properties. Semi-empirical models are often used to calculate these coefficients in specific materials under certain conditions, but they must be validated against experimental data to ensure accuracy. Researchers continue to refine these models to better understand the underlying physics of impact ionisation and to optimise the performance of semiconductor devices that rely on carrier multiplication.

2.6 Excess noise

Excess noise in semiconductors is a critical concept that plays a significant role in determining the performance of various semiconductor devices, particularly those designed for signal amplification and detection, such as APDs and other high-gain devices. In essence, excess noise refers to the additional noise that arises due to random fluctuations in the processes that generate electrical signals within these devices. In many cases, excess noise is directly linked to the stochastic nature of the carrier multiplication processes, such as impact ionisation, which can occur in devices subjected to high electric fields. Understanding the sources and implications of excess noise is vital for the design of high-performance semiconductor components, especially in applications that demand precise signal detection, such as optical communication, imaging systems, and scientific instrumentation.

The main source of excess noise in semiconductor devices like APDs comes from the randomness associated with the impact ionisation process, which is the mechanism that underlies carrier multiplication in these devices. When an electron or hole is accelerated by a strong electric field, it gains sufficient energy to ionise atoms in the semiconductor lattice, generating additional electron-hole pairs. These newly generated carriers are also accelerated by the electric field, leading to further ionisation events, which create an avalanche effect. However, the ionisation process is inherently random: not every carrier gains enough energy to cause ionisation, and the exact location and timing of ionisation events are unpredictable. This randomness leads to fluctuations in the number of carriers generated during the avalanche process, causing excess noise beyond the inherent thermal and shot noise typically present in semiconductor devices.

In an ideal semiconductor device with perfect carrier multiplication, the number of electron-hole pairs generated by impact ionisation would be the same for each avalanche event. In reality, however, the number of carriers generated in each event varies due to the probabilistic nature of impact ionisation. As a result, the output current from a device like an avalanche photodiode is not constant, but fluctuates around an average value, introducing excess noise. This noise can degrade the signal-to-noise ratio (SNR) of the device, making it harder to distinguish the desired signal from the background noise, especially in applications where weak signals need to be amplified or detected.

The magnitude of excess noise in semiconductor devices depends on several factors, including the impact ionisation coefficients of the material, the ratio of electron and hole ionisation rates, and the multiplication gain of the device. The impact ionisation coefficients for electrons and holes, typically denoted by α and β, respectively, represent the probability that an electron or a hole will cause ionisation as it travels through the semiconductor. In many materials, α and β differ, meaning that electrons and holes do not contribute equally to the multiplication process.

This disparity leads to additional noise, as the overall multiplication gain depends on which type of carrier initiates the avalanche.

The excess noise factor, often denoted by F, is a quantitative measure of the additional noise introduced by the random nature of carrier multiplication in a semiconductor device. It is defined as the ratio of the total noise in the device to the noise that would be present if the multiplication process were noiseless. In other words, F represents how much the random variations in the multiplication process increase the overall noise level. For a given material and device structure, the excess noise factor increases with the multiplication/gain, M, and can be expressed approximately by the formula:

$$F = kM + (1-k)\left(2 - \frac{1}{M}\right) \qquad (2.14)$$

where k is a factor that depends on the relative contributions of electron and hole ionisation to the multiplication process.

$$k = \frac{\beta}{\alpha} \qquad (2.15)$$

In devices where the ionisation rates of electrons and holes are nearly equal (i.e., $\alpha \approx \beta$), the excess noise factor is higher because the random fluctuations in ionisation events are more pronounced. In contrast, in materials where one type of carrier dominates the ionisation process (for example, where α is much larger than β or vice versa), the excess noise factor is lower, as the multiplication process is more consistent and less subject to random variations.

In APDs, excess noise is a critical design consideration, as these devices rely on carrier multiplication to achieve high sensitivity. APDs are used in applications where detecting extremely weak optical signals is essential, such as in fibre optic communication systems, LIDAR, and scientific measurements. The carrier multiplication process in APDs allows for the amplification of weak optical signals into detectable electrical currents. However, the excess noise introduced by random variations in the impact ionisation process can significantly degrade the performance of the APD, particularly by reducing the signal-to-noise ratio (SNR). To minimise excess noise, semiconductor materials with a high disparity between the electron and hole ionisation coefficients are preferred, as they lead to more predictable and lower-noise multiplication gains.

Different semiconductor materials exhibit different levels of excess noise, depending on their intrinsic properties. Silicon, for instance, is widely used in APDs due to its relatively favourable ratio of electron and hole ionisation coefficients, which results in lower excess noise compared to many other materials. In silicon, the ionisation coefficient for electrons is significantly larger than that for holes, which means that electron-initiated multiplication is the dominant process, leading to reduced noise. This makes silicon APDs particularly well-suited for low-noise applications, such as optical communication systems, where maintaining a high SNR is crucial for reliable signal detection and transmission.

In contrast, compound semiconductors such as gallium arsenide (GaAs) or indium phosphide (InP) tend to have more balanced ionisation coefficients for electrons and holes, leading to higher excess noise in APDs made from these materials. However, these materials are often used for detecting longer-wavelength light (such as in the infrared range), where silicon is less efficient due to its larger bandgap. As a result, designers of APDs must carefully balance the trade-off between excess noise and wavelength sensitivity when selecting materials for specific applications.

Temperature also plays a significant role in determining the level of excess noise in semiconductor devices. As the temperature increases, the thermal energy of the charge carriers increases as well, leading to more frequent scattering events. These scattering events can dissipate the carriers' energy before they have a chance to cause ionisation, thereby reducing the overall multiplication gain. However, higher temperatures can also increase the likelihood of non-radiative recombination events, where electron-hole pairs recombine without generating a measurable signal. This can further contribute to noise, making it challenging to design semiconductor devices that operate reliably in high-temperature environments.

In applications where low-noise performance is essential, such as in scientific instrumentation or high-speed communication systems, engineers take several measures to minimise excess noise. These include selecting materials with favourable impact ionisation properties, optimising the design of the device to minimise the influence of random ionisation events, and controlling the operating temperature to ensure stable performance. In some cases, additional signal processing techniques, such as noise filtering or amplification with low-noise circuits, are used to further improve the signal-to-noise ratio and mitigate the effects of excess noise.

2.7 Random Path Length (RPL) model

Monte Carlo (MC) models generally provide the most accurate method for simulating high-field carrier scattering, though they are computationally intensive. To develop a more efficient non-local model, Hayat et al.[10] introduced a recursive technique based on the probability distribution function (PDF) of a carrier's ionization path length in an electric field, enabling the simulation of multiplication and excess noise even in small avalanche regions, down to 0.1 μm [11] . Ong et al. [12] proposed the Random Path Length (RPL) model, which selects ionization path lengths randomly to determine the carrier ionization probability. Within an MC framework, displaced ionization path length PDFs are used to predict multiplication and excess noise in avalanche photodiodes (APDs). Both methods produce similar results in terms of gain and noise predictions.

The Random Path Length (RPL) model describes the behaviour of a carrier in a region with a given electric field, where the carrier's movement is characterized by an ionization path length PDF, $h(x)$. This function represents the probability that a carrier, after traveling a distance x from its initial position x_0, will undergo ionization. The expression for this probability is given as follows[11] :

$$h_e(x) = \begin{cases} 0 \quad , & x < d_e \\ \alpha^* \exp\left[-\alpha^*(x - d_e)\right], & x \geq d_e \end{cases} \tag{2.16}$$

$$h_h(x) = \begin{cases} 0 \quad , & x < d_h \\ \beta^* \exp\left[-\beta^*(x - d_h)\right], & x \geq d_h \end{cases} \tag{2.17}$$

Where x represents the distance electron travels, and similar $-x$ for holes, α^* and β^* are the effective ionization coefficients for electron and hole respectively, d_e and d_h are the dead space for electron and hole respectively.

$$d_e = \frac{E_{the}}{\xi} \tag{2.18}$$

$$d_h = \frac{E_{thh}}{\xi} \tag{2.19}$$

Where E_{the} and E_{thh} are threshold energy for electron and hole to ionize and ξ is the electric field strength.

2.8 References

[1] W. Shockley, "The theory of p-n junctions in semiconductors and p-n junction transistors," *Bell System Technical Journal*, vol. 28, no. 3, pp. 435–489, Jul. 1949. doi:10.1002/j.1538-7305.1949.tb03645.x

[2] S. N. Sze, *Physics of Semiconductor Devices*. New York etc.: John Wiley, 1981.

[3] E. F. Schubert, *Light-emitting diodes*, pp. 59–85, Jun. 2006. doi:10.1017/cbo9780511790546

[4] J. Iveland, L. Martinelli, J. Peretti, J. S. Speck, and C. Weisbuch, "Direct measurement of Auger electrons emitted from a semiconductor light-emitting diode under electrical injection: Identification of the dominant mechanism for efficiency droop," *Physical Review Letters*, vol. 110, no. 17, Apr. 2013. doi:10.1103/physrevlett.110.177406

[5] M. Winter, "The Periodic Table of the Elements," The periodic table of the elements by WebElements, https://winter.group.shef.ac.uk/webelements/ (accessed May 5, 2024).

[6] I. Vurgaftman, J. R. Meyer, and L. R. Ram-Mohan, "Band parameters for iii–V compound semiconductors and their alloys," *Journal of Applied Physics*, vol. 89, no. 11, pp. 5815–5875, Jun. 2001. doi:10.1063/1.1368156

[7] A. R. Mohmad et al., "Localization effects and band gap of GaAsBi Alloys," *Physica Status Solidi (b)*, vol. 251, no. 6, pp. 1276–1281, May 2014. doi:10.1002/pssb.201350311

[8] G. E. Stillman and C. M. Wolfe, "Avalanche Photodiodes," *Semiconductors and Semimetals*, pp. 291–393, 1977. doi:10.1016/s0080-8784(08)60150-7

[9] A. G. Chynoweth, “Ionization rates for electrons and holes in Silicon,” *Physical Review*, vol. 109, no. 5, pp. 1537–1540, Mar. 1958. doi:10.1103/physrev.109.1537

[10] M.M. Hayat, B.E.A. Saleh, and M.C. Teich, “Effect of dead space on gain and noise of double-carrier-multiplication avalanche photodiodes,” *IEEE Trans. Electron Devices*, vol. 39, pp. 546-552, Mar. 1992.

[11] M.A. Saleh, M.M. Hayat, O.-H. Kwon, A.L. Holmes, J.C. Campbell, B. E. A. Saleh, et al., "Breakdown voltage in thin III–V avalanche photodiodes," *Applied Physics Letters*, vol. 79, pp. 4037-4039, 2001.

[12] D.S. Ong, K.F. Li, G.J. Rees, J.P.R. David, and P.N. Robson, “A simple model to determine multiplication and noise in avalanche photodiodes”, *Journal of Applied Physics*, vol. 83, pp. 3426-3428, 1998.

3. Methodology

In this chapter, the device processing procedure, measurement principles and equipment used during the experiment of photoluminescence, photocurrent, IV, CV and photo-multiplication are introduced in detail.

3.1 Device Processing

The fabrication processes described in this chapter are performed in Clean Room for p^+-i-n^+ photodiode on GaAsBi wafers. A standard chemical etching process are involved in forming different sizes of devices.

3.1.1 Sample cleaving and cleaning

The process begins by cleaving the wafer into small samples, followed by a 3-stage solvent cleaning procedure using n-Butyl Acetate ($C_6H_{12}0_2$), Acetone (C_3H_60), and Isopropyl Alcohol (C_3H_80) in succession.

3.1.2 Sample Metallisation

3.1.2.1 Back contact

The surface of the sample should be clean and free of any dirt and dust, which need to be distinguished from permanent growth defects. The sample fabrication stage begins with back contact metallization, which involves using a high vacuum evaporator to evaporate InGe/Au within a pressure range of $2x10^{-6}$ to $6x10^{-6}$ Torr. When doing metallization, two metallization pumps are required, the first for InGe and the second for Au. Then, the annealing process is carried out for 30 seconds within the temperature range of 350 °C to 420 °C to ensure that the metal diffuses into the semiconductor and forms a good ohmic contact and this is shown in Figure 3.3(b).

3.1.2.2 Top contact

Prior to top contact metallisation, photolithography is conducted first on a top surface of a sample covered with thin layer of photoresists. First, the sample need to be soft baked for 1 minute on the purpose of dehydration. Then spin PMGI on the top and bake for 6 minutes at 180 °C. After that SPR350 will be put on the top of PMGI and baked for 1 minute at 100 °C which is shown in Figure 3.3(c). The mesa pattern of 200µm, 100µm, 50µm and 25µm radius of circles devices are aligned to the sample area to fit in as many devices as possible. The samples then are expose under UV light using mask aligner and immersed in the MF26A developer to remove the exposed positive photoresist. The top surface is shown in Figure 3.1 and the process is shown in Figure 3.3(d). Then, the evaporation using Au-Zn-Au evaporates takes place. Three metallization pumps are required in this step, the first for 5 nm Au, the second for 10 nm Zn and the last for 200 nm Au. The whole surface area is now covered with metal as a p-type contact as shown in Figure 3.3(e).

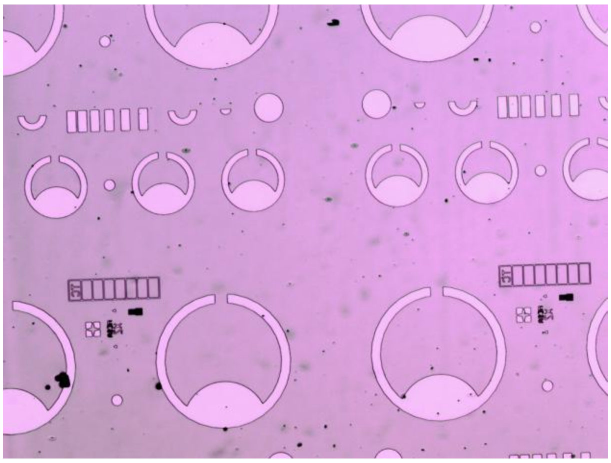

Figure 3.1 Top surface of the sample after photolithography and before metallization

During the fabrication stage, the lift-off process is used to dissolve undeveloped photoresist and remove excess metal. The sample will be slowly stirred in an acetone beaker, and a pipette can be used to introduce some bubbles and lower pressure to remove unwanted metals. After ensuring that there is no metal deposition in the active area of the device, same annealing process is performed. After the annealing, the quality of the top metal can be tested by transmission line measurement (TLM).

The second stage of photolithography was performed to create the mesa pattern that isolates individual devices. A second mask with a deep mesa etch pattern was used, adding an additional 10 µm radius to each device, resulting in final sizes of 210 µm, 110 µm, 60 µm, and 35 µm. UV light was exposed on the remaining sample area, excluding the device area. The exposed photoresist then dissolved in the developer, allowing the exposed areas to undergo the etching process. This stage concludes with a top view of the device after the second photolithography step.

3.1.3 Wet Chemical Selective Etching

The selective etching is the process of removing specific material, without perturbing on any other material. Figure 3.3(f) shows the device with metal contact fabricated on top and bottom surface, before etching stages. The positive photoresist is first covered the whole surface area, before exposed under deep mesa mask pattern. Followed by immersing in developer, the exposed area under UV light will be dissolved and leaving photoresist to cover optical window only, as shown in Figure 3.3(g) and (h).

The sample is then fully immersed in 1:1:1 etchant contains a part of each Hydrobromic acid, Acetic acid, and Potassium Dichromate solutions. Another etching solution is 1:8:80 which contains sulfuric acid, hydrogen peroxide solution and deionized (DI) water. The mixture of etchants will react with GaAs and GaAsBi without attacking the photoresist. A minute in 1:1:1 solution will etch ~2 µm depth and ~0.3 µm depth in 1:8:80. After ensuring the sidewalls of devices has been etched with a desired thickness through Dektek, the photoresist on optical window area is now removed and all the devices will be isolated with each other as shown in Figure 3.2 and this process is shown in Figure 3.3(i) and (j).

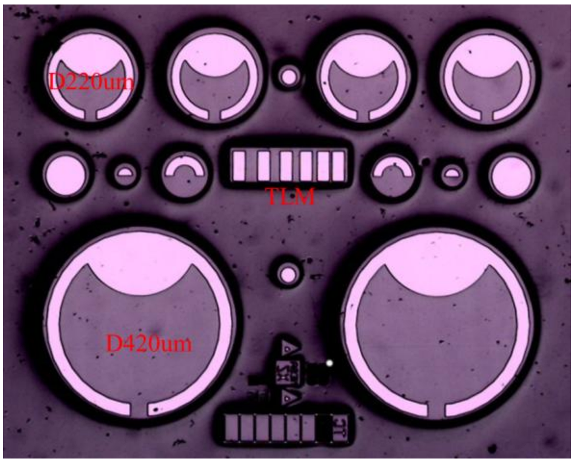

Figure 3.2 A cell of different size devices.

In Figure 3.2, there are four different size of devices which are mention above, also there is a TLM and a stair label in one cell.

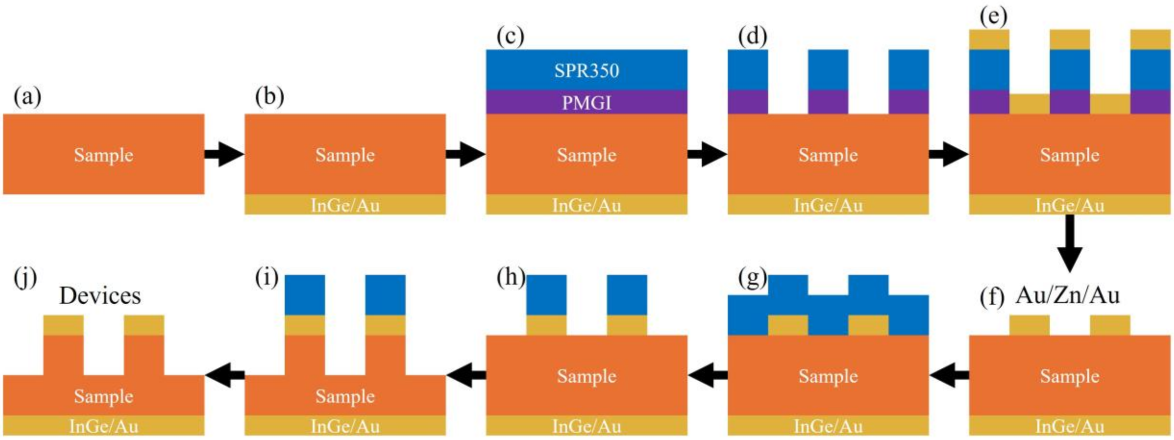

Figure 3.3 Standard device processing procdure step by step. (a) Original sample; (b) back metal(InGe/Au); (c) top photoresist; (d) expose and develop; (e) top metal(Au/Zn/Au); (f) lift off; (g) etching photoresist; (h) expose and develop; (i) wet etching; (j) photoresist remove and final device.

3.2 Photoluminescence (PL) measurement

Photoluminescence (PL) spectroscopy is a precise, non-invasive optical technique used to analyse the bandgap and other optical properties of semiconductors. Light absorption in the semiconductor can be affected by defect energy levels or localized states, and by varying the incident laser power and sample temperature, further insights into these effects can be gained. PL is particularly useful for evaluating the optical quality of materials, as it allows for the analysis of bulk and defect-related electron transitions. This non-destructive method provides important information about material characteristics such as energy bandgap and inhomogeneity, the latter often indicated by the full width at half maximum (FWHM). Additionally, PL can estimate the proportion of Bi in the material based on bandgap changes and assess whether photon-induced carrier recombination is significantly contributing to the emission or if other recombination mechanisms dominate. However, one limitation of PL is its inability to directly measure non-radiative recombination intensity in the device.

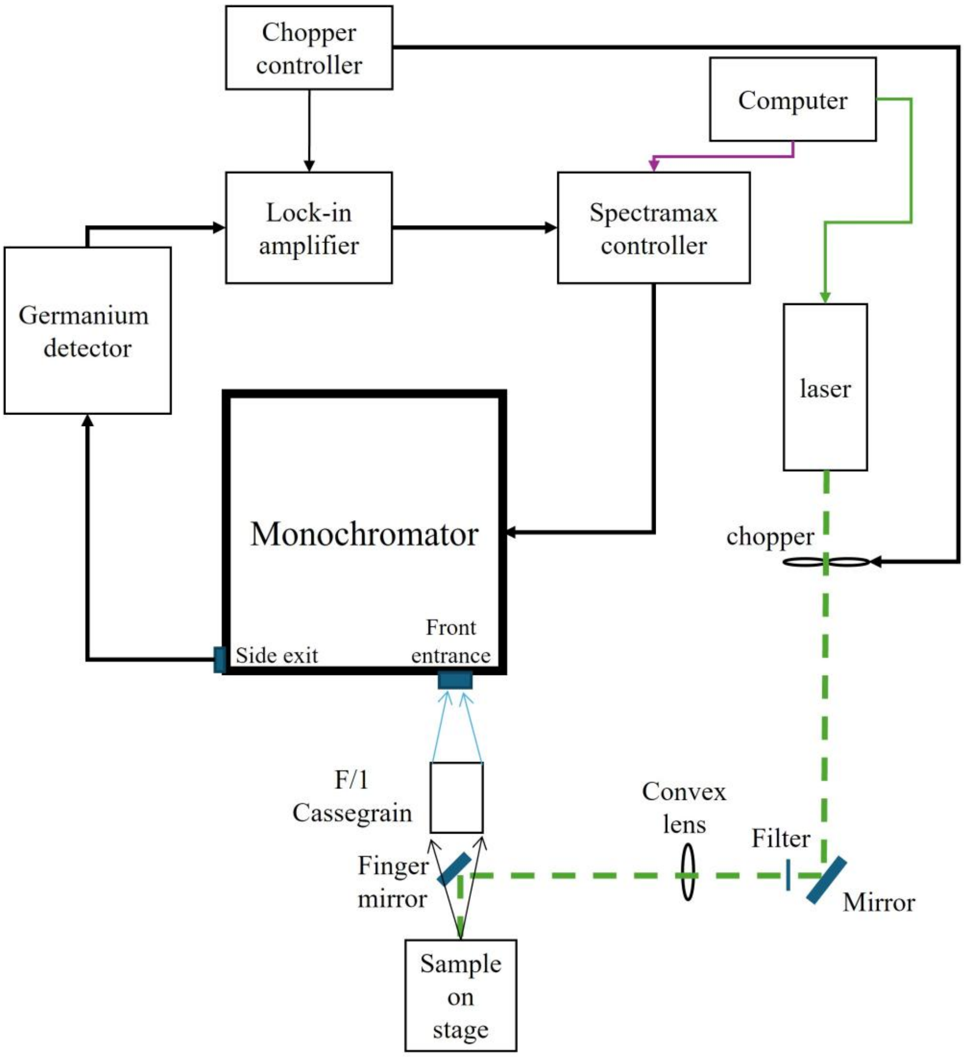

Figure 3.4 Simple diagram of photoluminescence setup

Figure 3.4 illustrates the experimental setup for photoluminescence (PL) measurement. A continuous-wave diode-pumped solid-state laser with a wavelength of 532 nm is used as the excitation source, with second-order effects occurring at 1064 nm. The laser has a spot size of approximately 250 μm. A 350-550 nm band-pass filter is used to block higher-order excitation, allowing only the 532 nm wavelength to pass through. The laser beam is modulated using a chopper set to a frequency of ~180 Hz, which ensures that the signal is not affected by interference from the main power supply, typically operating at multiples of 50 Hz. At room temperature, the sample is placed on an X-Y-Z stage for precise positioning and focusing.

For low-temperature PL measurements, the sample is placed in a closed-cycle helium compressor system, which can reduce the temperature to ~10K and stabilize it at ~19K. The system includes a cryostat with a cold finger plate connected to a temperature controller. The cryostat is mounted on an X-Y-Z stage for accurate sample positioning. The helium compressor, vacuum pump, and water supply system are used to create a low-pressure environment, allowing low-temperature PL measurements. The sample is attached to a cold plate using vacuum grease, which provides thermal conductivity and prevents air from being trapped under the sample during cryogenic operations.

When the laser beam excites the sample, the luminescence signal is collected by an F/1 Cassegrain lens, which must be aligned with the optical axis of the monochromator to maximize signal collection. The signal is then focused and enters the monochromator, which in this case is a Horiba iHR550 spectrometer. The monochromator features three gratings with 1200, 900, and 600 grooves/mm, and for this setup, the 900 grooves/mm grating is used, as the wavelength range of interest is between 700 and 1600 nm. The entrance and exit slits are set to 1 mm.

The PL signal is detected by a 77K germanium (Ge) detector, capable of detecting signals below 1700 nm. The detector is cooled using liquid nitrogen to maintain this temperature. A lock-in amplifier (LIA) is used for phase-sensitive detection, synchronized with the chopper frequency to eliminate unwanted noise and stray signals from the surrounding light sources. Neutral density (ND) filters are employed to attenuate any strong PL signals, and the software

SpectraMax is used to control the scanning and record the LIA data.

3.3 Photocurrent measurement

The photocurrent setup is illustrated in Figure 3.5. The light from the light source undergoes spectral dispersion via the monochromator, which is controlled by a PC. The selected wavelength is focused on the exit slit of the monochromator and modulated at 180 Hz by a chopper and the entrance slit and exit slit are set to be 2 mm wide. The chopper's frequency is synchronized with a lock-in amplifier (LIA) as a phase-locked signal. The diode is connected in series with a load resistor, and the LIA is connected in parallel to the load resistor, ensuring that only the voltage drop across the resistor is fed to the LIA. Depending on the dark current levels, different load resistor values can be chosen for the measurement.

The data shown on the control PC corresponds to the converted LIA reading, which measures the voltage drop across the resistor. Based on the sensitivity settings of the LIA, the accuracy and precision of the actual photocurrent can be controlled. Equation (3.1) describes the relationship between the LIA conversion value and the voltage drop across the diode, while Equation (3.2) provides the photocurrent calculation, which is essentially an adjustment of Ohm's law, [1]

$$V = \frac{intensity}{10} \times sensitivity \tag{3.1}$$

$$photocurrent = \frac{V}{0.45 \times R} = \frac{\frac{intensity}{10} \times sensitivity}{0.45 \times R} \tag{3.2}$$

After the calculation of photocurrent, the measurement of one commercial diode needs to be done. The choosing of commercial diodes dependents on the wavelength needed. For short wavelength from 400 nm to 800 nm, a silicon PIN commercial diode S5973-02 is used[2] . After this range, an InGaAs PIN diode FDGA05 is used to measure system response within 800 nm to 1700 nm[3] .

The responsivity’s equation is:

$$R = \frac{photocurrent}{P} \tag{3.3}$$

where P is power.

Transfer equation (3.3), the power of commercial diode can be calculated with equation below:

$$P_{diode} = \frac{photocurrent_{diode}}{R_{diode}} \tag{3.4}$$

Subsequently, the power of the commercial device can be calculated using equation (3.4). The commercial InGaAs FDGA05 has a radius of 250 nm effective window, while the largest device used has a radius of 200 nm or 210 nm. Additionally, the effective area of the device is 70% of its total area. Moreover, with a reflection coefficient of 0.32, only 68% of the incident power is available for use. Then the real power on the device can be calculated as:

$$\mathrm{P}_{device} = 0.7 \times 0.64 \times 68\% \times P_{diode} \tag{3.5}$$

According to the power of the device measure, the responsivity of the semiconductor can be extracted by equation (3.3), and it is:

$$R_{device} = \frac{photocurrent\ of\ device}{P_{device}} \tag{3.6}$$

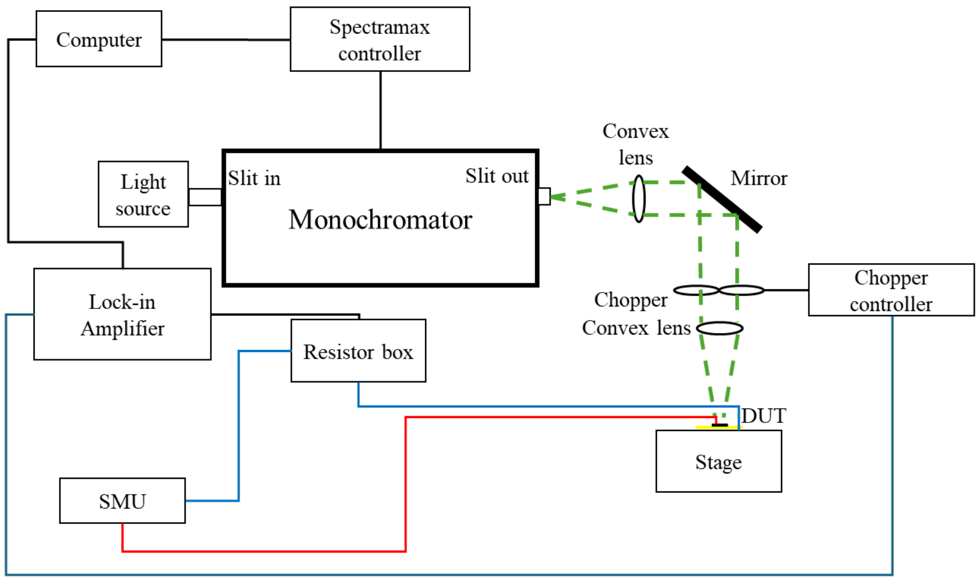

Figure 3.5 The schematic diagram of photocurrent setup

The absorption coefficient is expressed:

$$\alpha = \frac{1}{w}\frac{hv}{q}\frac{1}{1-R_{device}}\frac{1}{\eta}\frac{I_{ph}}{\lambda} \tag{3.7}$$

where w is depletion region, R is the reflectance and η is the quantum efficiency.

The relationship between absorption coefficient and photon energy is:

$$\alpha(hv) = \alpha_g e^{\frac{hv-E_g}{E_0}} \tag{3.8}$$

where E_g is bandgap and α_g is absorption coefficient at the bandgap, E_0 is the low density of states on the shallow localized states and is called Urbach energy[4] . It is used as a quality index of semiconductors[5] .

3.4 Current-voltage (IV) measurement

In IV measurement, the bias is applied through the diode and current will be generated across the circuit. As shown in Figure 3.6, room temperature forward and reverse bias dark I-V measurements were conducted using a Hewlett-Packard HP4140B pico-ammeter[6] , controlled via software on a PC connected through a GPIB cable. A curve tracer was used in the setup to manually verify the diode connections before performing the actual measurements and to confirm if the diode was functioning correctly. Additionally, the curve tracer was used to determine the breakdown voltage of the diode.

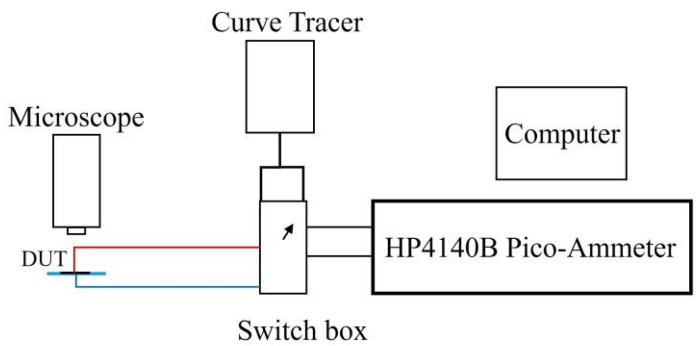

Figure 3.6 The I-V measurement setup.

Dark current refers to the small electric current that flows through a photodetector or semiconductor device even when there is no incident light or optical signal present. It is an inherent phenomenon in APDs, arising from thermal excitation or other non-photon-related processes that cause the generation of electron-hole pairs within the semiconductor material. It follows the Shockley equation[7] mentioned in equation 2.2. The equation can also be given by:

$$J = J_0 \left[\exp\left(\frac{qV}{nkT}\right) - 1 \right] \tag{3.9}$$

where J_0 is the saturation current density, q is the electron charge (1.6×10^{-19}), k is the Boltzmann constant (1.38×10^{-23}), T is the temperature in , n is the ideality factor as introduced in Section 2.2.

In the absence of light, thermal energy can excite electrons in the semiconductor, promoting them from the valence band to the conduction band. This movement of electrons generates a small but measurable current, known as dark current, which exists independently of any external illumination. The amount of dark current typically increases with rising temperature since higher temperatures provide more energy to the electrons, making them more likely to escape their bound states.

3.5 Capacitance-voltage (CV) measurement

In a p-n junction, the formation of a depletion region arises due to the surplus of holes and electrons in the p-type and n-type respectively. The free majority carriers diffuse due to the concentration gradient and the remaining atomic lattice becomes charged. At the edges of the p and n-type material the negatively and positively charged lattice respectively act as the parallel plates of a capacitors with an electric field in between to prevent further diffusion in order to maintain equilibrium in the flow of carriers.

$$C = \frac{\varepsilon A}{w} \tag{3.10}$$

where C is the capacitance, ε is the relative permittivity of the material, A is the area and w is the depletion width.

The Poisson solver is a calculation technique used to determine the electric field profile within semiconductor devices, by solving the Poisson equation for a given charge distribution. In this section, a homojunction p^+-p-n^+ diode is considered. Capacitance measurements can reveal information regarding the depletion width, doping profile and built-in potential of a diode. Capacitance of a diode can be calculated with the following equation:

$$C = \frac{\varepsilon A}{w} \tag{3.11}$$

where C is the capacitance, ε is the permittivity of the material, A is the area of the device, and w is the depletion width.

The equation for ε is:

$$\varepsilon = \varepsilon_0 \varepsilon_r \tag{3.12}$$

where ε_0 is the permittivity of vacuum and ε_r is the relative permittivity of the material.

Doping density can be measured by following equation:

$$N = \frac{2}{\frac{d\frac{1}{C^2}}{dV} e\varepsilon A^2} \tag{3.13}$$

HP 4275A LCR meter in Figure 3.7 is used to measure the CV in this section and the schematic of CV set up is shown in Figure 3.8.

Figure 3.7 Front of HP 4275A LCR meter used in CV set up

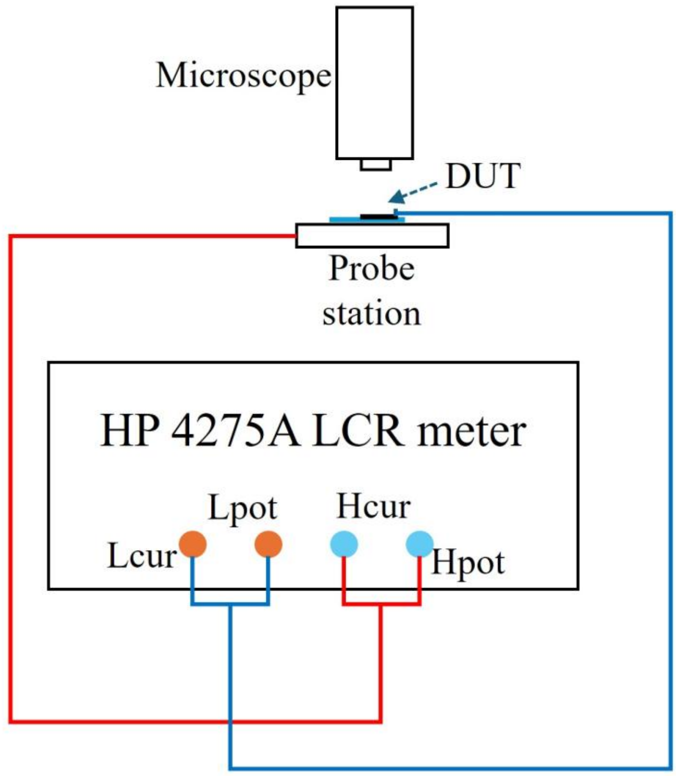

Figure 3.8 Schematic diagram of CV set up. Lcur. Lpot, Hcur, Hpot are low current, low potential, high current, high potential respectively.

3.6 Photo-multiplication measurement

Avalanche multiplication is a process where high electric fields accelerate carriers, causing them to collide with atoms, generating additional electron-hole pairs, resulting in exponential current growth within a semiconductor. Figure 3.9 shows the schematic diagram of the photo-multiplication setup. A laser spot with a diameter of about 50 µm to 100 µm is focused to the top of samples through some adjustable mirrors and focusing lenses. The images of the device and the laser spot can be viewed on the monitor through the camera and the beam splitting cube. Keithley 236 or 237 SMU is used to voltage bias the DUT and resistor. The laser source is modulated by a mechanical chopper at a frequency of about 180 Hz. Similar to photocurrent setup, the LIA measures the photocurrent generated by the voltage drop across the resistor. When the dark current is significantly lower than the photocurrent, SMU can be used to measure the dark current and total current. The dark current has no laser illumination, and the total current has laser illumination. By subtracting the dark current from the total current, the multiplied photocurrent is determined as a function of the bias voltage. The multiplication can be expressed as:

$$M = \frac{measured\ photocurrent}{primary\ photocurrent} = \frac{I_{ph}}{I_{pr}} \qquad (3.14)$$

Also, from Woods et al[8] , I_{ph} can be solved as:

$$I_{ph} = \frac{qG_0}{\cosh\left(\frac{L}{L_d}\right)} \qquad (3.15)$$

where G_0 and L_d are two adjustable parameters,

and L is defined as:

$$L = L_0 - \sqrt{2\epsilon/(qN_D)(V + V_D)} \qquad (3.16)$$

where L_0 is the thickness of the device, N_D is the doping density, ϵ is the permittivity of this material and V_D is the built-in voltage.

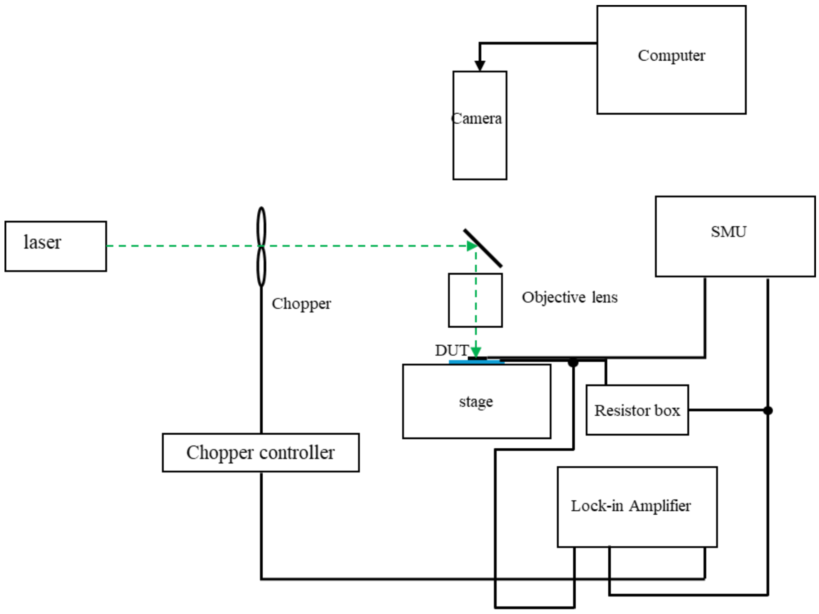

Figure 3.9 Schematic diagram of photo-multiplication setup

3.7 Excess noise measurement

Similar to multiplication setup, the setup of noise is shown in Figure 3.10. There is a DUT system for the sample to be probed. A trans-impedance amplifier (TIA) with a gain of 2200 V/A was used to convert the photocurrent signal into a proportional square waveform at the chopper frequency. The signal was further amplified by a unity-gain amplifier and measured by a lock-in amplifier (LIA) to determine the photocurrent. The TIA output, containing both the photocurrent and its noise, was passed through a bandpass filter (MiniCircuit SBP 10.7) to remove the photocurrent. Additional amplification stages enhanced the noise voltage before it was converted to a mean square value by a power meter. An attenuator was used to control signal strength, and both LIAs were connected to the mechanical chopper controller to have the same frequency.

The multiplication analysis is the same as previous section. The excess noise factor, F, is:

$$F = \frac{N_{DUT}}{N_{Si}} \tag{3.17}$$

The Si device used in this work is SFH2701, which is a non-avalanching diode and has a unity gain at -10 V. The shot noise power of the SFH2701 was measured at varying optical intensities to fully represent the shot noise under non-avalanche operating conditions.

In practice, an ideal APD does not exist, so it is not possible to achieve ideal noise power from a real APD. However, the noise characteristics can be approximated using a non-avalanching Si p-i-n photodiode. When operating in non-avalanching mode, a Si p-i-n photodiode exhibits full shot noise, which is comparable to that of an ideal APD.

The noise power for an ideal Si device can be described as:

$$N_{Si} = 2qI_{pr}BM^2G \tag{3.18}$$

where B is the effective noise bandwidth (ENBW), G is the system gain and M is the multiplication.

In the real device, the noise power is:

$$N_{DUT} = 2qI_{pr}BM^2GF \tag{3.19}$$

If the measured noise power is equalled to the non-avalanching Si p-i-n photodiode noise power, then:

$$N_{DUT} = 2qI_{ph}BG \tag{3.20}$$

F can be expressed as:

$$F = \frac{N_{DUT}}{N_{Si}} = \frac{I_{ph}}{I_{pr}M^2} \tag{3.21}$$

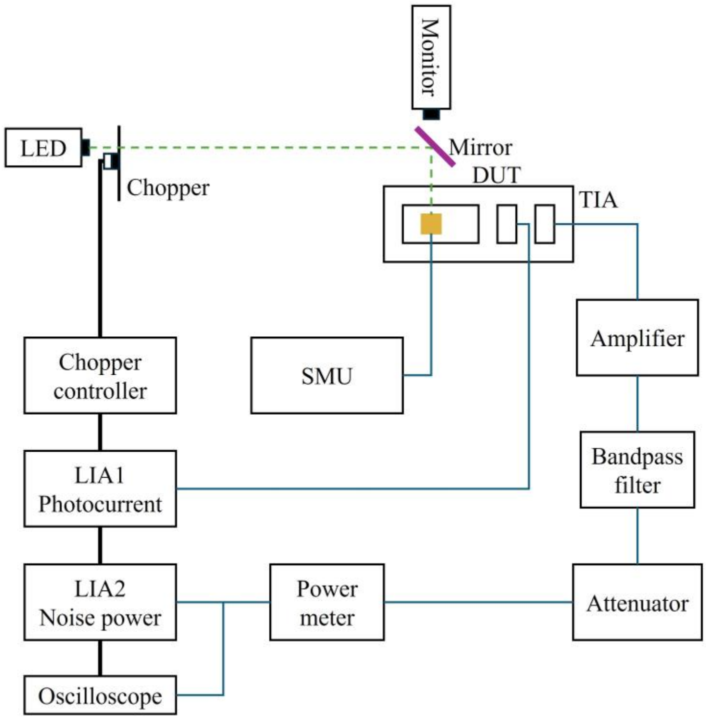

Figure 3.10 Schematic diagram of noise setup

3.8 References

[1] S. R. S. Inc., "Model SR830 DSP Lock-In Amplifier," ed. California, US, 1993

[2] “Si Pin Photodiode S5973-02: Hamamatsu Photonics,” Si PIN photodiode S5973-02 | Hamamatsu Photonics, https://www.hamamatsu.com/jp/en/product/optical-sensors/photodiodes/si-photodiodes/S5973-02.html (accessed Jul. 22, 2024).

[3] “Thorlabs - FDGA05 InGaAs photodiode, 2.5 ns rise time, 800-1700 nm, ø0.5 mm active area,” Thorlabs, Inc. - Your Source for Fiber Optics, Laser Diodes, Optical Instrumentation and Polarization Measurement & Control, https://www.thorlabs.com/thorproduct.cfm?partnumber=FDGA05 (accessed Jul. 22, 2024).

[4] F. Urbach, "The Long-Wavelength Edge of Photographic Sensitivity and of the Electronic Absorption of Solids", *Physical Review*, vol. 92, no. 5, pp. 1324-1324, 1953. Available: 10.1103/physrev.92.1324.

[5] E. Schubert and H. Yao, *Light-emitting diodes,* 2nd ed. Bellingham, Wash.: SPIE, 2002, pp. 146-159.

[6] HP 4140b PA meter / DC voltage source, https://www.valuetronics.com/media/vti/datasheets/HP 4140B.pdf (accessed Jul. 22, 2024).

[7] W. Shockley, “The theory of p-n junctions in semiconductors and p-n junction transistors,” *Bell System Technical Journal*, vol. 28, no. 3, pp. 435–489, Jul. 1949. doi:10.1002/j.1538-7305.1949.tb03645.x

[8] M. H. Woods, W. C. Johnson, and M. A. Lampert, “Use of a Schottky barrier to measure impact ionization coefficients in semiconductors,” S*olid-State Electronics*, vol. 16, no. 3, pp. 381–394, Mar. 1973. doi:10.1016/0038-1101(73)90013-0

4. CHAPTER 4: Room temperature Ionization coefficient and excess noise in $Al_{0.70}In_{0.30}As_{0.74}Sb_{0.26}$ on InP substrate

4.1 Introduction

An avalanche photodiode (APD) is a vital component in low-light optical receivers. APDs designed for short wavelength infrared (SWIR) regions, particularly at 1.55 µm and 2 µm, have shown significant potential for applications in LIDAR within the defence, space[1] [2] , and commercial sectors[3] . APDs are especially beneficial in low-light conditions due to impact ionization, which amplifies the signal and helps overcome circuit readout noise. However, the sensitivity of commercial APDs at 1.55 µm and 2 µm is largely constrained by excess noise, which limits the achievable gain. The overall sensitivity of an optical receiver is defined by its signal-to-noise ratio (SNR). For an APD receiver with gain, SNR is given by equation(4.1):

$$SNR = \frac{I_{ph}^2 M^2}{2qM^2(I_{ph}+I_d)F(M)\Delta f + N_{Amp}} \tag{4.1}$$

where I_{ph} is the gain-free photocurrent that is proportional to quantum efficiency (QE), M is the field-dependent gain from impact ionization, q is the elementary charge, I_d is the gain-free dark current, $F(M)$ is the excess noise factor, Δf is the bandwidth, and N_{Amp} is the noise power from the readout circuit. The crux to reduce $F(M)$ at high gain is to use a low k multiplier material, k is the ratio of impact ionization coefficients of the holes (β) to electrons (α)[4] [5] [6] [7] [8] . Therefore, for a given N_{Amp}, a high QE, a low I_d, and a low k are all needed to increase the SNR of an APD.

Recently, research efforts have expanded to focus on $Al_xIn_{1-x}As_ySb_{1-y}$ lattice-matched to GaSb substrates. At the University of Texas, researchers have conducted thorough investigations into this alloy material. Woodson M.E. et al. [9] explored the development and performance of $Al_{0.7}In_{0.3}As_{0.3}Sb_{0.7}$ APDs grown on GaSb substrates. This material system was chosen due to its advantageous ionization properties, which make it suitable for low-noise applications. The researchers focused on achieving low excess noise, which is critical for improving the sensitivity of APDs, particularly in telecommunications and imaging applications. Their study demonstrated that the $Al_{0.7}In_{0.3}As_{0.3}Sb_{0.7}$ APDs exhibit a low k -value (β/α) of 0.015, which is comparable to that of silicon, traditionally known for its low-noise performance in APDs. The low k -value was achieved due to the material's high electron impact ionization and a large effective hole mass, which reduces noise. Furthermore, the devices exhibited stable gains of up to 95 before breakdown occurred at 40.5 V. In addition, the external quantum efficiency peaked at 68% near 700 nm, with a cutoff wavelength of 1.1 um, demonstrating the material's potential for near-infrared applications. Overall, the research highlights the promise of AlInAsSb alloys in creating high-performance, low-noise APDs for advanced photonic systems. However, a smaller bandgap with aluminium content below 50% leads to significantly high dark current, which worsens as the aluminium percentage decreases.

Ren M. et al. [10] [11] extended the study to investigate the characteristics of $Al_xIn_{1-x}As_ySb_{1-y}$ (x = 0.3-0.7) in APDs. The study demonstrates APDs with Al concentrations from x = 0.3 to 0.7, achieving k -values as low as 0.01, which is comparable to silicon. These APDs showed potential for a wide wavelength range, particularly in telecommunications. They demonstrated a SAM-APD configuration using $Al_{0.4}In_{0.6}AsSb$ as the absorption layer and $Al_{0.7}In_{0.3}AsSb$ as the multiplication layer, balancing low dark current with improved low-noise performance[12] . The excess noise results were comparable to those of silicon, which is promising for next-generation APDs in telecommunications. Also, Jones et al.[13] presented a detailed analysis of the temperature dependence of avalanche breakdown in $Al_xIn_{1-x}As_ySb_{1-y}$ photodiodes grown on GaSb substrates, showing breakdown values of 6 mV/K and 15 mV/K for AlInAsSb p-i-n and SAM-APD structures, respectively. Despite these advancements, the need to grow this alloy on GaSb substrates makes it more challenging and costly to develop, and its small bandgap limits dark current control.

An SACM APD design employs distinct materials for its absorption and multiplication regions, allowing for independent optimization of quantum efficiency in the absorption layer and multiplication M and excess noise factor k in the multiplication layer. For infrared APD applications, HgCdTe is a well-established, high-performance material that doesn't require an SACM structure but does necessitate cooled operation to function effectively[2] [14] . This approach is essential for optimizing the performance of optoelectronic devices, especially in low-light applications. Current commercial SWIR APDs designed for room temperature operation typically utilize SACM structures that pair absorber and multiplier layers made from InGaAs/InP or InGaAs/InAlAs. These material combinations enable efficient performance without the need for cooling, which is a key advantage in applications requiring high sensitivity and low noise at short-wave infrared (SWIR) wavelengths[15] . These commercial SWIR APD options use InP substrates to enhance manufacturability. However, their performance is constrained by the high k -value in the multiplication region, particularly in the InP and InGaAs or InAlAs layers. This high k-value leads to increased noise, which limits the achievable operational gain and signal-to-noise ratio (SNR) in these APDs[16] [17] [18] [19] . Consequently, while these devices are practical for room temperature operation, their performance is restricted compared to other lower-noise technologies. Researchers have identified several alternative, InP substrate-based multipliers, such as InAlAs[20] [21] , AlAsSb[22] [23] , AlGaAsSb[24] [25] [26] , AlGaInAs[27] , and AlInAsSb that improve k over InP or InAlAs. For short-wavelength infrared (SWIR) APDs, a separate absorption, charge, and multiplication (SACM) design is commonly employed. This design allows for independent optimization of each region, improving performance. AlInAsSb grown on InP substrates is emerging as a promising candidate for the multiplication layer because it can achieve a lattice match with various absorber materials suitable for SWIR applications. This combination offers potential for enhanced performance in SWIR detection by reducing noise and increasing operational efficiency. In this chapter, characteristics and analysis on $Al_{0.70}In_{0.30}As_{0.74}Sb_{0.26}$ pin diode will be introduced. This study is based on the work done by Kodati[28] of these key characteristics for AlInAsSb on InP. In this work, a higher M and lower k than previously reported is measured, also the material's ionization coefficients from measurements of gain close to breakdown are extracted and this material is demonstrated to be promised as an APD multiplier. Most of the results have been published in reference [29] .

4.2 Layer details

4.2.1 AlInAsSb growth condition

The $Al_{0.70}In_{0.30}As_{0.74}Sb_{0.26}$ was grown on InP using molecular beam epitaxy by Ohio State University as previously reported[28] . A PIN heterostructure, shown in Figure 4.1, was grown to support material characterisation. In this chapter, $Al_{0.70}In_{0.30}As_{0.74}Sb_{0.26}$ on semi-insulating (SI) (001) InP substrate was grown as a random alloy by molecular beam epitaxy (MBE). The substrate growth temperature was measured using a kSA BandiT system to be around 450 °C. The growth rate for this material was around 0.5 µm per hour, with a V/III ratio between 3 and 5. The Be was used for p-type doping and Si for n-type doping, with calibration performed on GaAs grown on a semi-insulating GaAs substrate previously. The Be and Si doping concentrations were measured using Hall measurements, and it was assumed that, for each set cell temperature, the dopants (Be and Si) were fully ionized, ensuring proper doping levels throughout the growth process. A 1-µm-thick unintentionally doped (UID) AlInAsSb layer was grown as the multiplication layer in the structure. To ensure low contact resistance, both the top and bottom contact layers were made from highly doped, low bandgap InGaAs. Additionally, the 300-nm-thick p+ AlInAsSb layer provides sufficient thickness to support single carrier injection, which is essential for achieving low excess noise in the device. The 20-nm top InGaAs layer serves as a protective cap to prevent AlInAsSb from oxidizing.[28]

4.2.2 AlInAsSb device fabrication

The schematic of the AlInAsSb PIN test devices is shown in Figure 4.1. The 1000 nm unintentionally doped (UID) AlInAsSb layer was designed to account for significant variations in the optical injection profile over different test wavelengths. A three-step fabrication process was used for single-pixel device creation. In Step 1, mesas were etched using a citric acid-based solution. In Step 2, the wafer underwent an HCl: H2O dip for oxide removal and was passivated with SU-8. In Step 3, the wafer was metallized with Ti/Au for the top and bottom contacts. The details of these fabrication can be found in reference[28] and [29] .

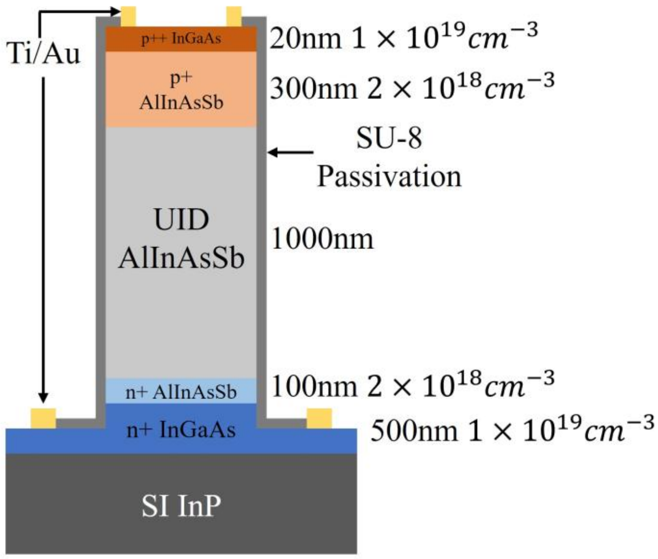

Figure 4.1 Heterostructure and test device schematic for the PIN AlInAsSb test devices.

4.3 Electrical characterisation

In this section, the electrical characterisation of the AlInAsSb PIN is shown, including IV and CV from three different fabricated samples. These three samples are chopped from same layer, but they are fabricated at different time and by different universities.

4.3.1 IV measurements

In the IV measurements, three different samples fabricated by the University of Sheffield (TUoS) and by the Ohio State University (OSU) will be presented.

As shown in Figure 4.2, there are three different sizes of devices been measured, sample fabricated by TUoS shows the surface current dominates between 0 and 0.4 V and after 0.4 V the bulk dark current dominates. Current density is shown in (b), and it shows a good scaling of area in forward IV. It gave a J_0 around $2.5nA/cm^2$ and ideality factor n around 2.13 with IV fitting. The IV fitting comes from diode equation in section 2.2. Series resistance gets involved after 0.6 V and makes the IV curve bend. Reverse dark IV was taken from different size of devices, and the result is shown in (c). From the reverse dark IV measurements, they show a clear sharp breakdown voltage at -60 V. Some devices show an edge breakdown. The reverse dark JV is shown in (d), most of the devices show a current density of $5 \times 10^{-5} A/cm^{-2}$ from -5V and before breakdown voltage. From (e), it is clear that the ideality factor is around 2 from

0.4V to 0.6 V. This is a small voltage range. Before 0.4 V it is the surface current issue which is also obvious in (a), and after 0.6 V the series resistance becomes a problem. In (d) and (f), reverse IV is not scale with neither area nor perimeter. This may come from the uncertainty of the etching process as the forward dark IV scale with areas. This sample will be called TUoS2021.

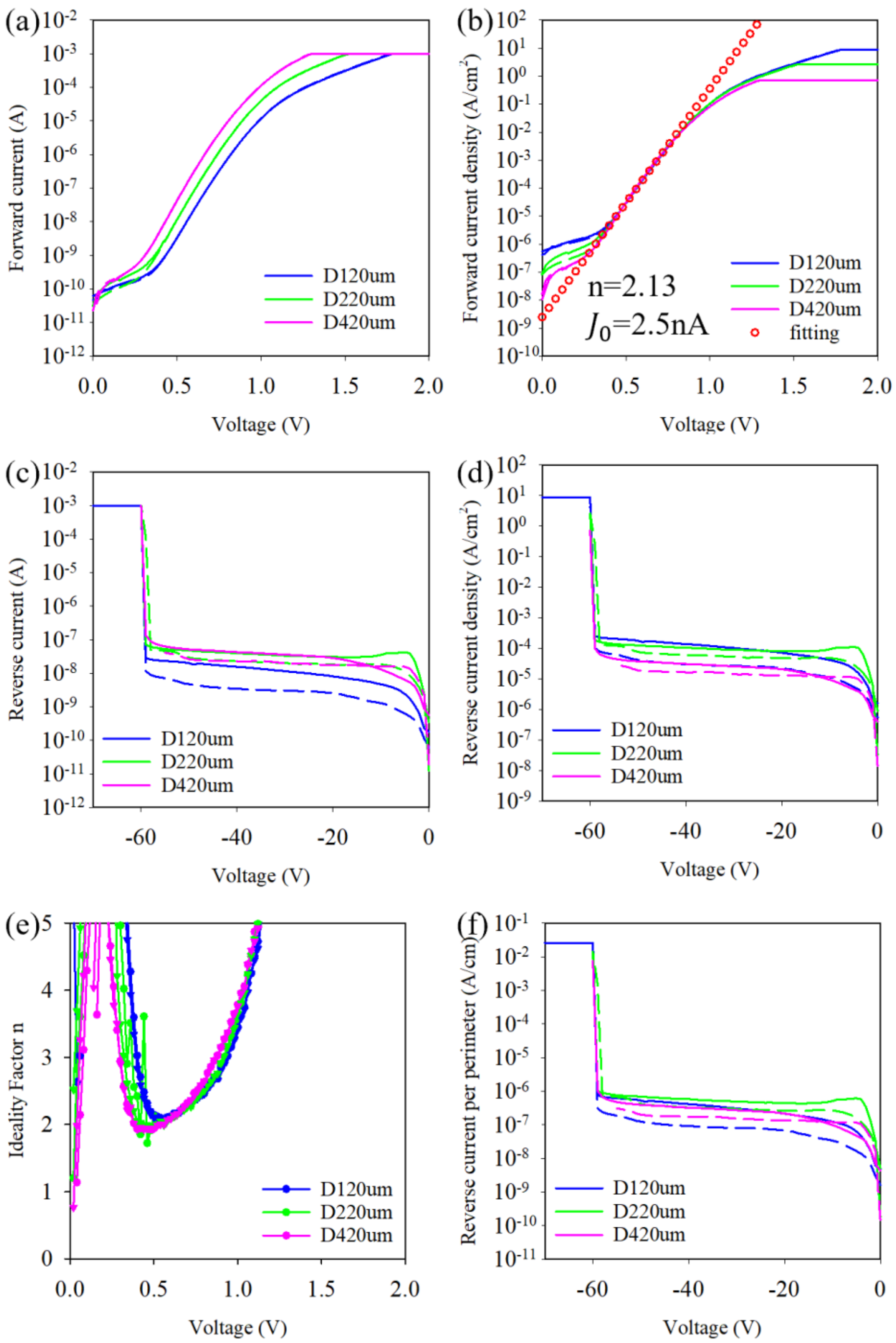

Figure 4.2 (a) Forward IV, (b) forward JV with fitting, (c) reverse JV (d) reverse IV, (e)

Ideality factor and (f) reverse current per perimeter for AlInAsSb fabricated by University of Sheffield in 2021 with different size of devices.

In Figure 4.3, it shows the dark current results of AlInAsSb fabricated by OSU in 2021. This sample will be called OSU2021. From (a) and (b), it is clear that the surface leakage happens from 0 V to 0.25 V. After 0.25 V the bulk dark current becomes significant. Series resistance started influencing the current from 0.45 V and the current density is only $5 \times 10^{-6} A/cm^{-2}$ which shows a huge series resistance. The IV from different size of devices scale with area at low bias indicates the bulk current property. From the JV fitting, this sample gives ideality factor of 1.7 and J_0 of $0.26 nA/cm^2$. From (e) it shows an ideality factor of 1.7 at 0.4 V. (c), (d) and (f) show that this ample has a stable breakdown voltage at -59 V. Also, the reverse dark IV scale with perimeter instead of area presents that surface current is large.

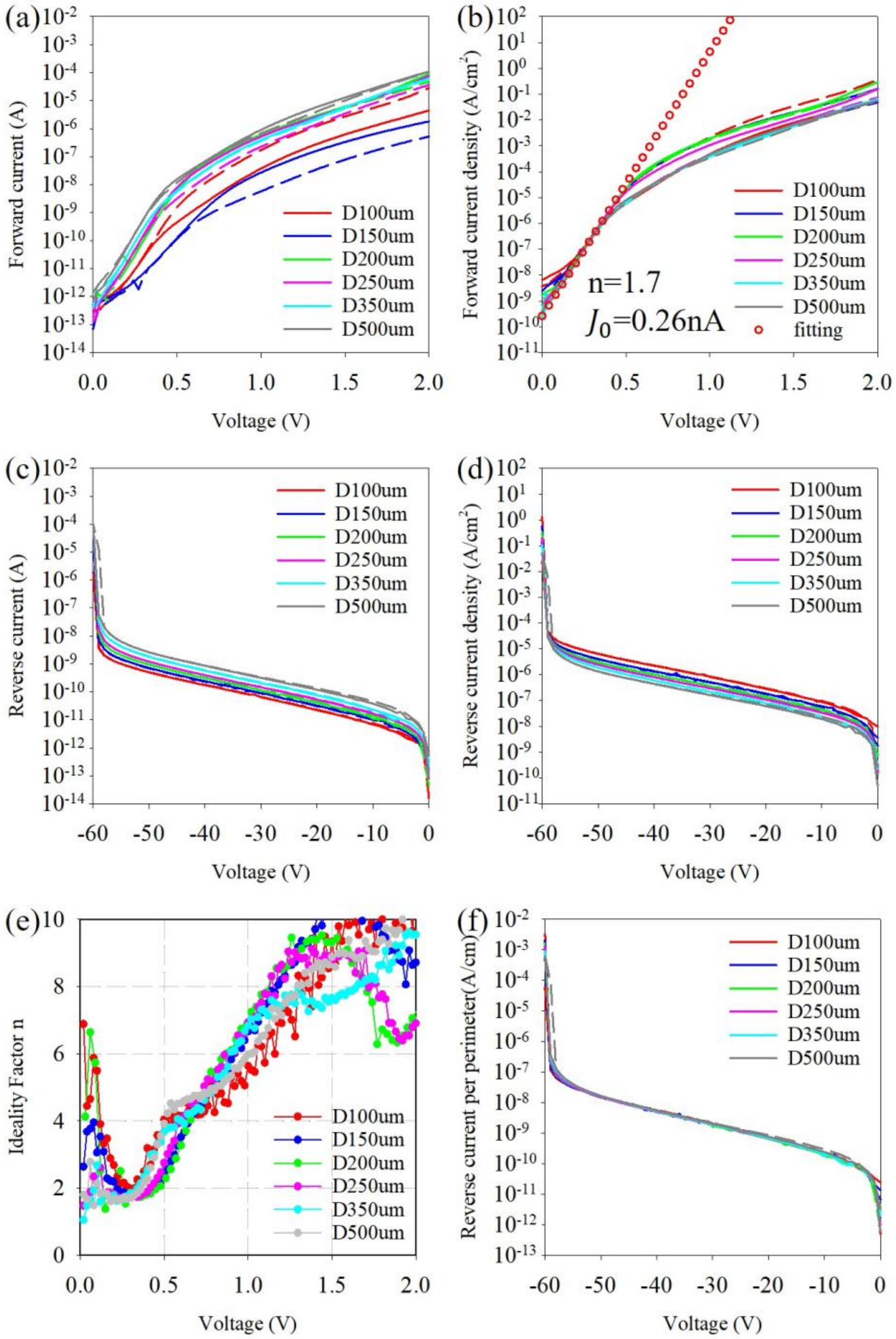

Figure 4.3 (a) Forward IV, (b) forward JV with fitting, (c) reverse JV (d) reverse IV, (e) Ideality factor and (f) reverse current per perimeter for AlInAsSb fabricated by OSU in 2021 with different size of devices.

Also, Figure 4.3 demonstrates the dark current results of AlInAsSb fabricated by OSU in 2022 and it will be shortened as OSU2022. The difference between this sample and the OSU2021 is the improvement of the metal deposition. From (a) and (b), most of the devices show almost no surface leakage. Also, series resistance comes into charge after 0.6 V. From the fitting, it shows the same ideality factor and J_0 as OSU2021. In (e), the ideality is lower than 2 from 0 V to 0.6 V which is better than OSU2021. From (c), (d) and (f), most of the devices show the same reverse dark IV as OSU2021.

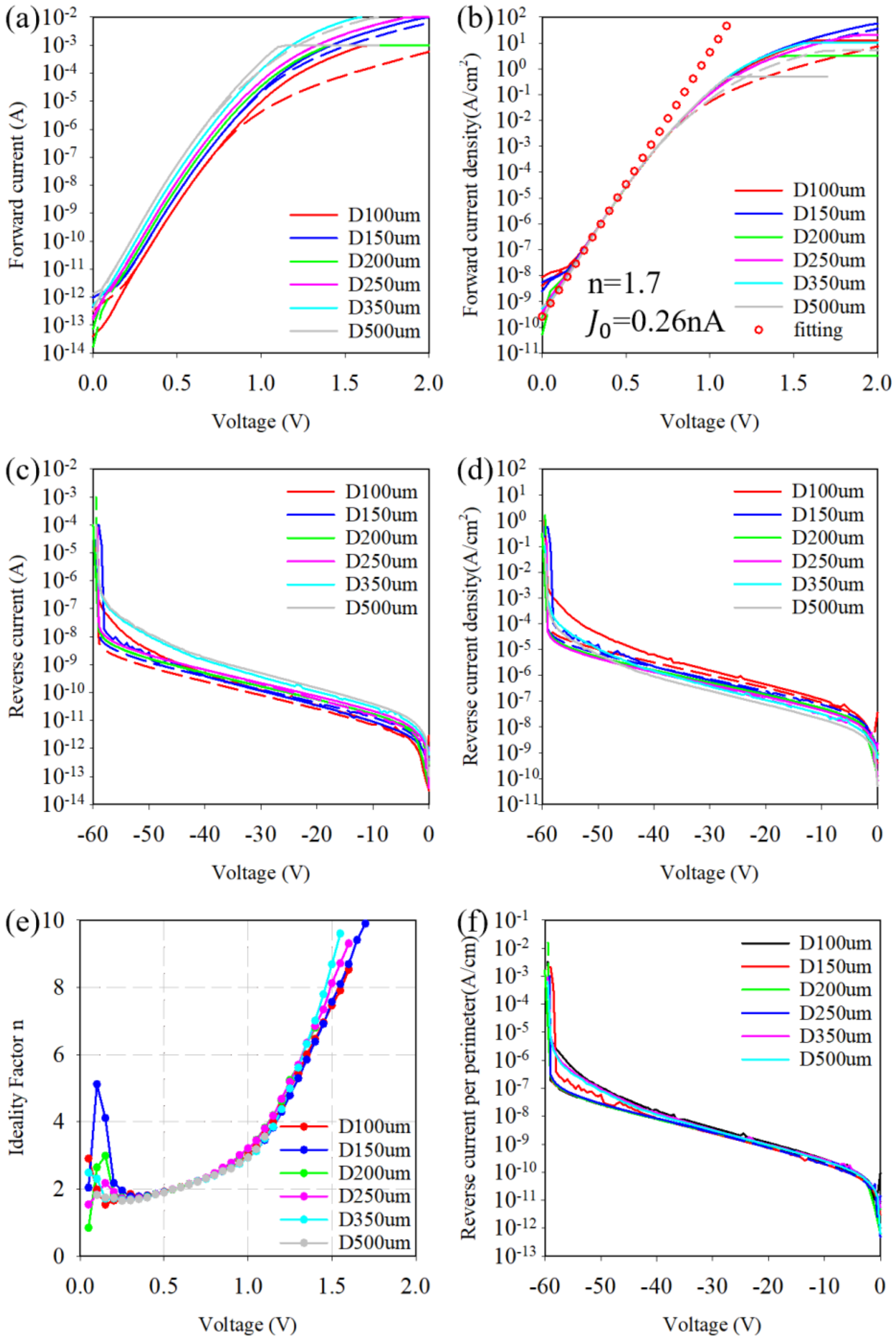

Figure 4.4 (a) Forward IV, (b) forward JV with fitting, (c) reverse JV (d) reverse IV, (e) Ideality factor and (f) reverse current per perimeter for AlInAsSb fabricated by OSU in 2022 with different size of devices.

All the comparison of these three samples is shown in Figure 4.5. (a) is the forward current density. It is obvious that from 0 V to 0.45 V, the OSU2021 shows the same JV as OSU2022, and from 0.5 V to 1 V, the OSU 2022 shows the similar results with TUoS2021. From these three samples, the ideality factor is calculated to be 1.7 and J_0 is $0.26nA/cm^2$. From the JV fitting of TUoS2021, the J_0 is different from here because it is hard to find the linear part of the curve in log-plot. From (b), OSU2022 shows a best ideality factor in the voltage range of 0.2 V to 0.5 V. Other two samples show much higher ideality factor values due to surface leakage and series resistance. From (c) and (d), the OSU2021 and OSU2022 have similar reverse dark current density. TUoS shows a 1000 times higher current density.

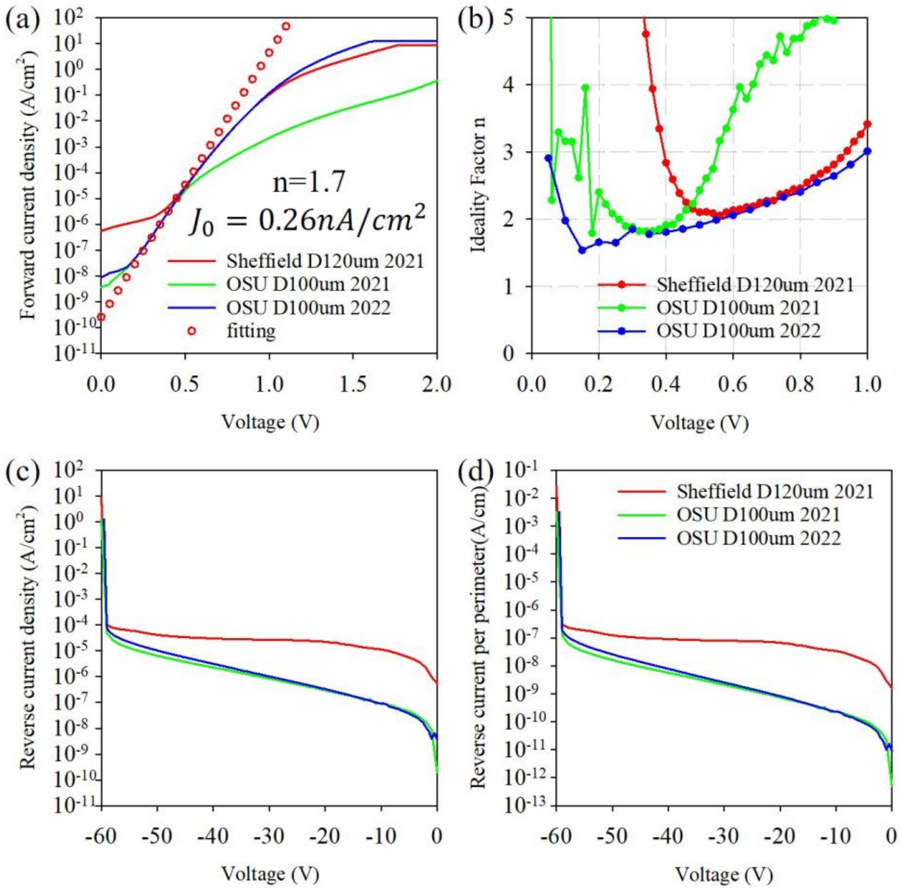

Figure 4.5 (a) Forward current density, (b) Ideality Factor n, (c) Reverse current density and (d) Reverse current per perimeter over three AlInAsSb samples.

4.3.2 CV measurements

The capacitance versus reverse bias results of these three p-i-n samples with different mesa diameters are introduced in this section.

As shown in Figure 4.6, when a reverse bias voltage is applied to a diode, the capacitance initially decreases rapidly due to the expansion of the depletion region within the lightly doped intrinsic (i) region. As the reverse bias increases, the depletion region extends into the heavily doped p or n regions, where the expansion slows down. This change in rate results in a region of constant capacitance, indicating that the intrinsic layer is fully depleted. The shift in capacitance behaviour helps identify the point at which further voltage changes no longer significantly affect the depletion region width. Regarding to (b), 6 µm is needed to be added into the diameter to get the capacitance of two big size devices scale with area. In this case the D120µm devices will not scale with others. According to this, in (c) only D426µm devices will be fitted with doping equation. From the fitting, i-region thickness is 1.09 µm, and the background doping is $1.7 \times 10^{15} cm^{-3}$. (d) shows the doping profile from CV results. Depletion width start from 1.1 µm and at 1.11µm the doping is as high as $5 \times 10^{17} cm^{-3}$ which means on this condition, 1.11 µm can be seen as fully depleted.

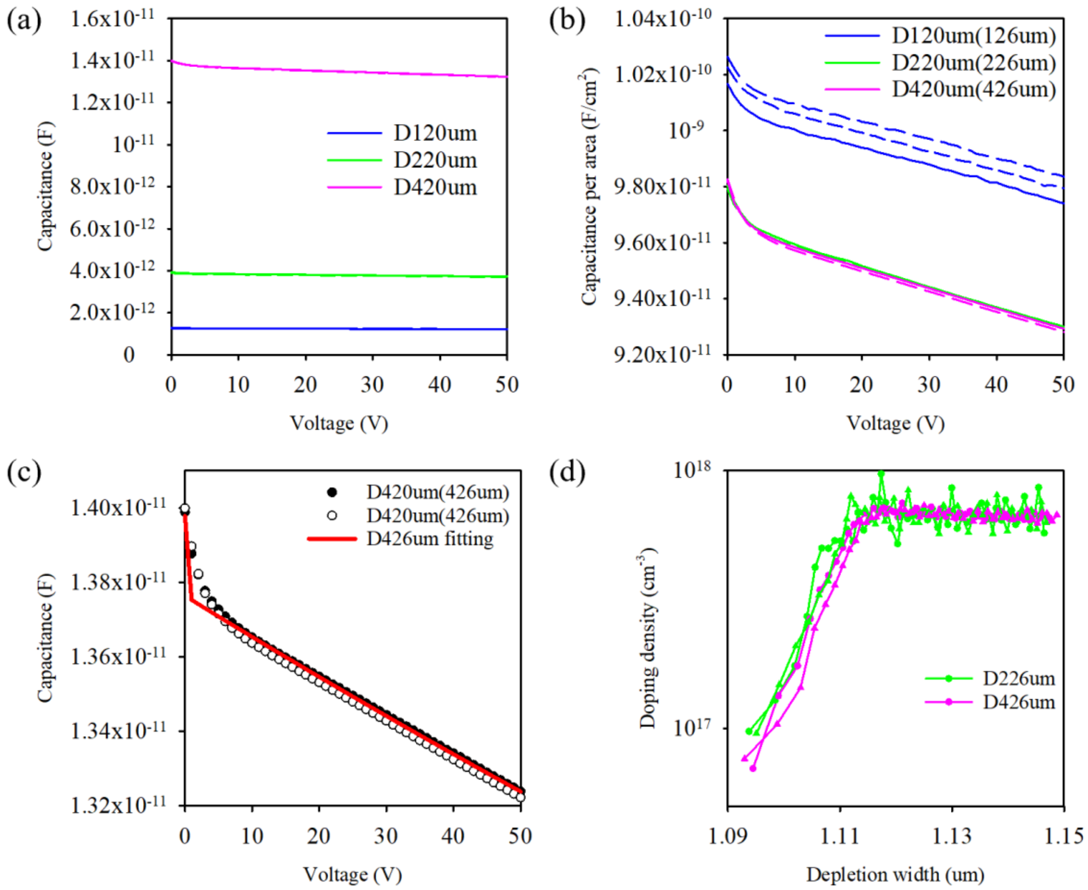

Figure 4.6 (a) CV; (b) Capacitance per area; (c) CV and fitting; (d) Doping profile of AlInAsSb sample fabriced by TUoS in 2021;

When it comes to OSU2021, the CV results are shown in Figure 4.7. However, several devices are measured but they all not scale with area as shown in (b). It is hard to determine the real size of most of the devices. 200 μm diameter device is used as an example to show the fitting value. From (c), the i-region thickness in the fitting is 1.12 μm and the background doping is $1.63 \times 10^{15} cm^{-3}$ which are both similar to TUoS2021. Due to the uncertainty of the device diameters, the doping profile shows a huge variation in (d). The depletion width ranges from 0.94 μm to 1.47 μm.

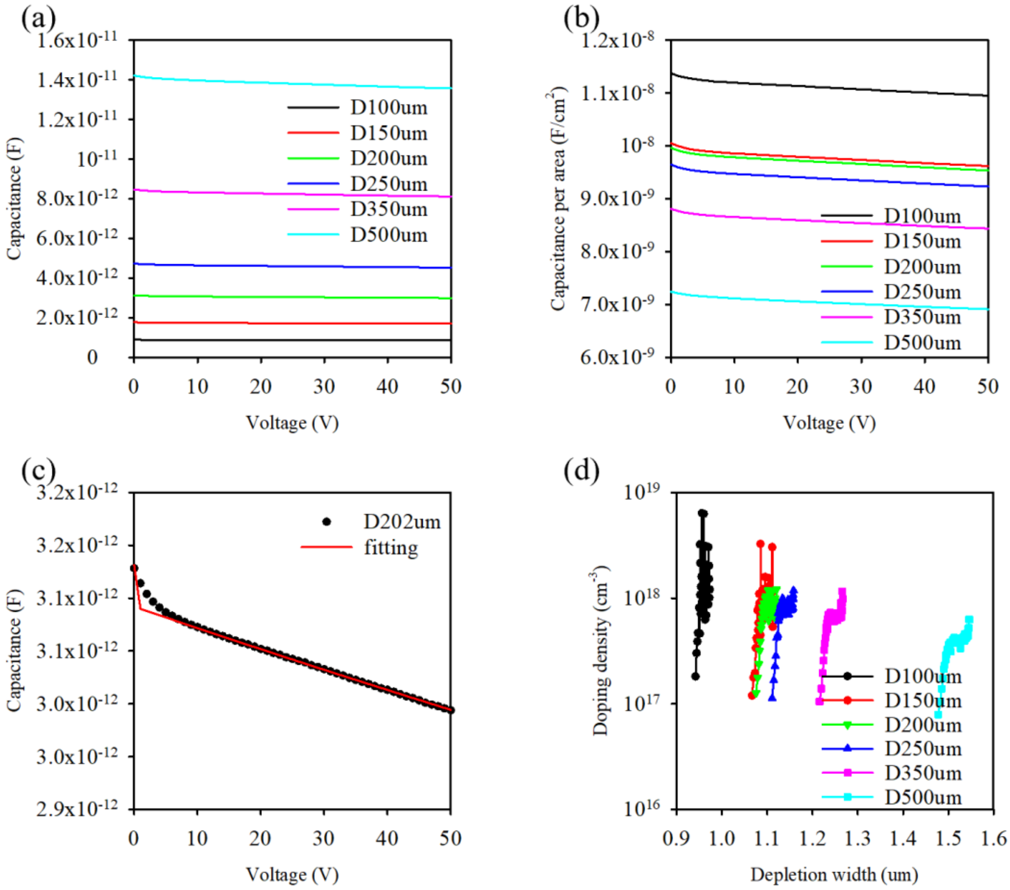

Figure 4.7 (a) CV; (b) Capacitance per area; (c) CV and fitting; (d) Doping profile of AlInAsSb sample fabriced by OSU in 2021;

With the improvement of the fabrication procedure, sample OSU2022 shows a good result compared to TUoS2021 and OSU2021. As shown in Figure 4.8, (a) indicates that the CVs measured by TUoS are scale with area and the error is within 0.2%. In (b), it shows different CV results measured by both TUoS and OSU on the same sample. It is clear that the CV data measured by OSU is higher than that in TUoS, but the error is within 1.8%. Under the circumstances, it can be said that most of the devices are scale with area. According to the CV on 350 μm diameter devices by two universities, the CV fitting is done in (c). The i-region thickness is 0.99 μm and the doping is $2 \times 10^{15} cm^{-3}$ in TUoS and 0.996μm and $2 \times 10^{15} cm^{-3}$ from OSU data. In (d) the depletion width is 0.99 μm which is agree to the fitting parameter.

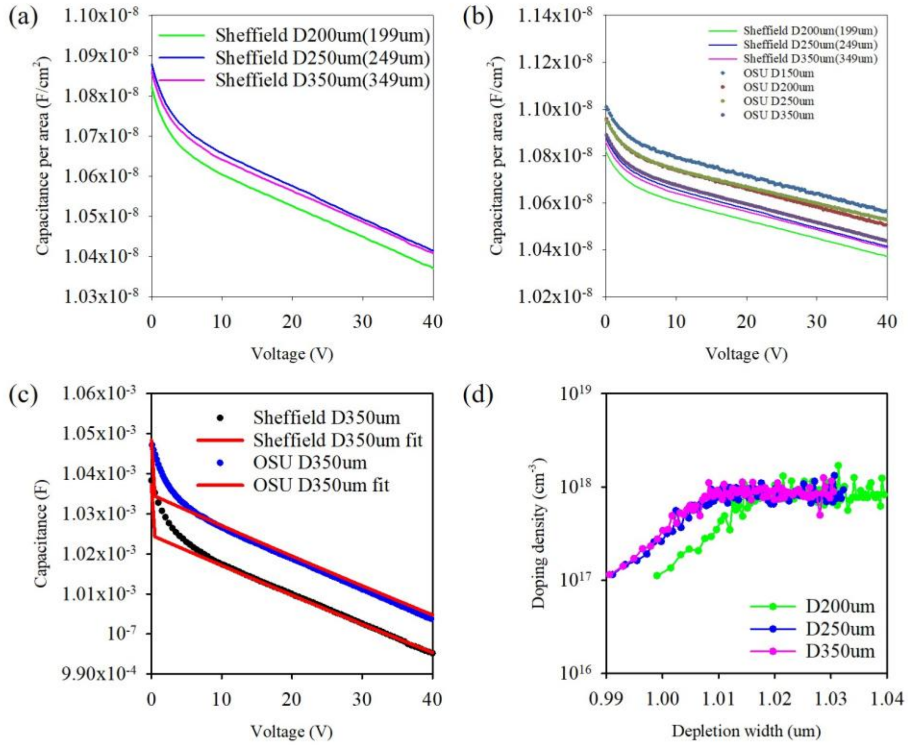

Figure 4.8 (a) Capacitance per area measured by TUoS; (b) Capacitance per area measured by TUoS and OSU; (c) CV and fitting; (d) Doping profile of AlInAsSb sample fabriced by OSU in 2022;

According to the CV data from three samples, the summary is shown in Table 4.1 below.

Samples	i-region thickness from doping profile (μm)	i-region thickness from CV fitting (μm)
TUoS2021	1.11	1.1
OSU2021	0.94-1.47	1.12
OSU2022 by Sheffield	0.99	0.99
OSU2022 by OSU	0.97	0.996

Table 4.1 i-region thickness from different fabricated samples and from different measurement results

As shown in Figure 4.9, the SIMS result gives a clear i-region thickness of 0.997 µm which will be used in the paper. This thickness is calculated by the different positions of Si and Be and the result is agreed with CV fitting above. There is an approximately 5% error range when the assumption is made. So, the i-region thickness could be from 987 nm to 1007 nm.

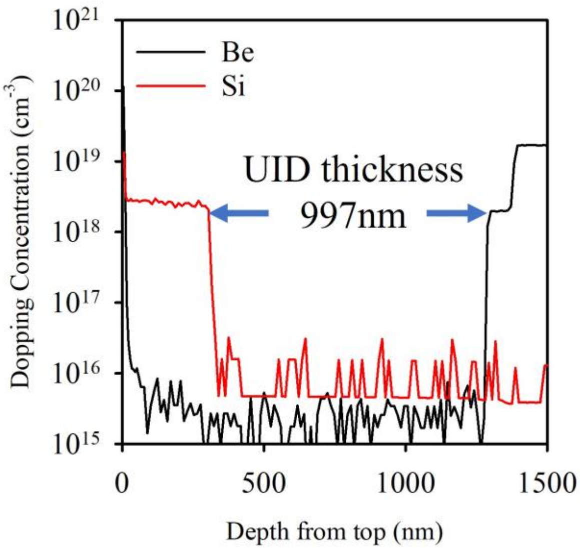

Figure 4.9 SIMS result of AlInAsSb

4.4 Photo-response measurements in AlInAsSb

The photo spectrum measurements were done on 200 µm diameter devices. As shown in Figure 4.10, with the increase of voltage, the relative photo spectrum is increasing. The cut off wavelength is around 780 nm.

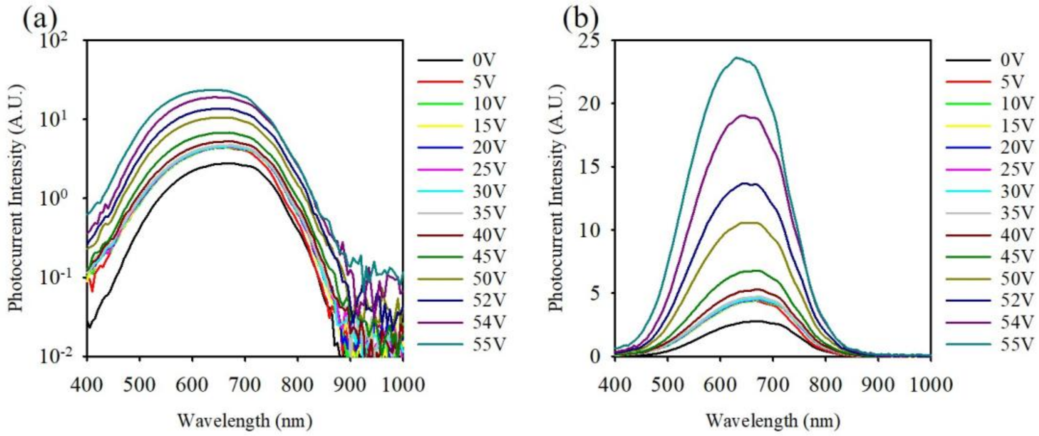

Figure 4.10 Bias dependent photo spectrum in (a) log plot and (b) linear plot.

In Figure 4.11, the maximum QE of this material is 25% which is similar to previous research done by Kodati et al [28] .Also, it shows that it has similar maximum QE compared to 85% AlGaAsSb. And it is clear the QE is higher than 75% materials.

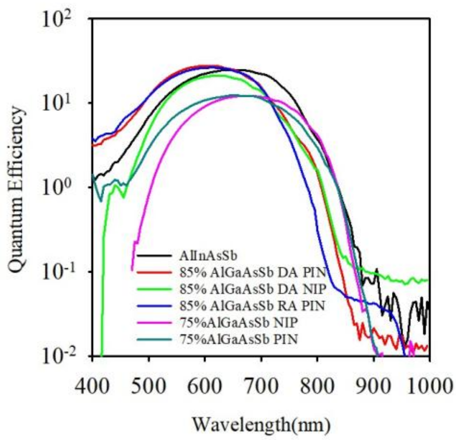

Figure 4.11 Quantum efficiency of AlInAsSb compared to 75% and 85% AlGaAsSb structures.

4.5 Photomultiplication characterisation

4.5.1 Photomultiplication

In this section, all the measurements were done on the 200 µm diameter devices on sample OSU2022 because OSU2022 has lower series resistance than OSU2021 and TUoS2021.

Figure 4.12 (a) and (b) show how the power and place change of the laser will affect the photocurrent and multiplication. From (a), it is clear that the reverse dark current is the lowest and if the laser is shone in the middle of the device, with the power reduced by ND filters, the photocurrent will drop down. At same power, photocurrent generated when laser shiny in the middle will be higher than that on the edge. (b) shows the multiplication when 20 V is set as the unity multiplication point. Regardless of the reverse dark current in (b), when the laser shiny in the middle of the device, with the increase of ND filter, the multiplication is higher at same voltage. The 450 nm without ND filter and pinhole has lowest multiplication when reach to breakdown voltage. This is because the laser power is too high, and laser spot is too big which can be shiny on the edge of devices. The lower power and smaller spot size, the better multiplication can be reached.

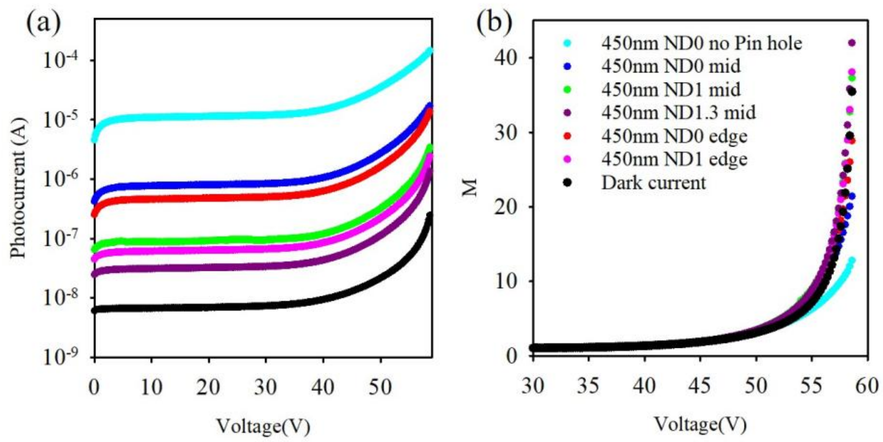

Figure 4.12 Power denepdence (a) original photocurrent and (b) multiplication with 450nm laser

In Figure 4.13 (a) and (b), the highest stable multiplication at 450 nm this sample can reach is 245 at 59.1 V when the unit gain is set at 20 V with less than 50 nA photocurrent. And this multiplication is 16 times higher than what Kodati et al reported[28] . The maximum observed gain with this material was previously reported at 15, but this limited gain is now believed to be due to this photon flux effect.

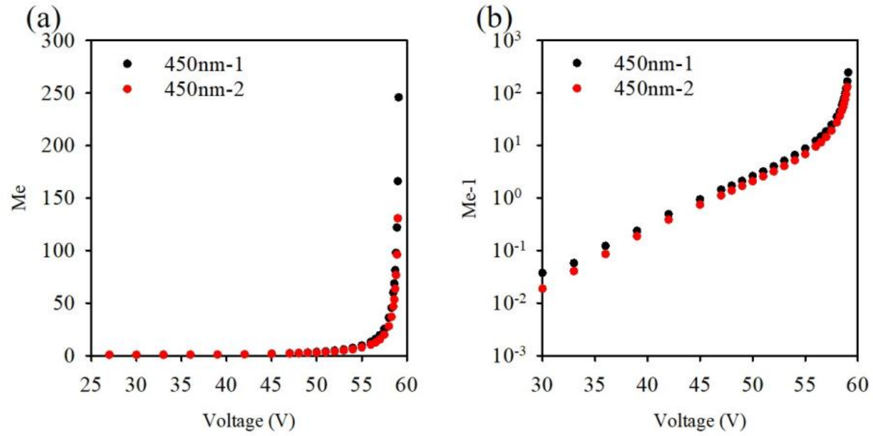

Figure 4.13 Highest (a) M_e and (b) $M_e - 1$ at 450 nm

With data from these improved devices and measurements, A mixed injection approach is applied to quantify the field dependence of impact ionization coefficients. New wavelength- and photon flux-dependent multiplication measurements, Figure 4.15, of this structure determined that the reported by Kodati et al[28] multiplication and noise characteristics were limited by the measurement conditions and not by the material. The device's multiplication and noise behaviour were found to be sensitive to photon flux and series resistance. Photo-generated carriers can screen the applied electric field due to space charge effects[30] , and this has the consequence of suppressing gain with increasing photon flux. In Figure 4.15, (a) shows the multiplication of a 200 µm diode at 450nm (blue dots), 532nm (green dots), 635nm (red dots), and 780nm (purple dots). This multiplication is calculated by cosh function done by Woods et al.[31] . (b) is the multiplication-1 in log plot. It makes the wavelength trend clearer. With the increase of wavelength, the lower multiplication is, this also means $M_e > M_{mix}$ which indicates that $\alpha \gg \beta$.

The primary photocurrent is:

$$I_{pr} = \frac{qG_0}{\cosh\left(\frac{L}{L_{pn}}\right)} \tag{4.2}$$

$$L = L_0 - W = L_0 - \sqrt{\left(\frac{2\in}{qN_D}\right)(V + V_D)} \tag{4.3}$$

Where L_0 is the thickness of the device, $\in$ is the permittivity of the material, N_D is the doping density and L_{pn} is the major carries diffusion length.

The linear model and cosh model are shown in Figure 4.14. Cosh baseline correction is used in the following multiplication analysis.

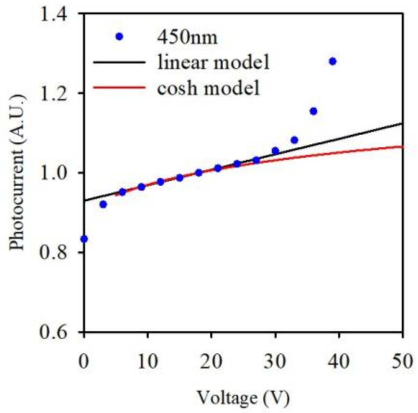

Figure 4.14 Linear model and cosh Fucntion model.

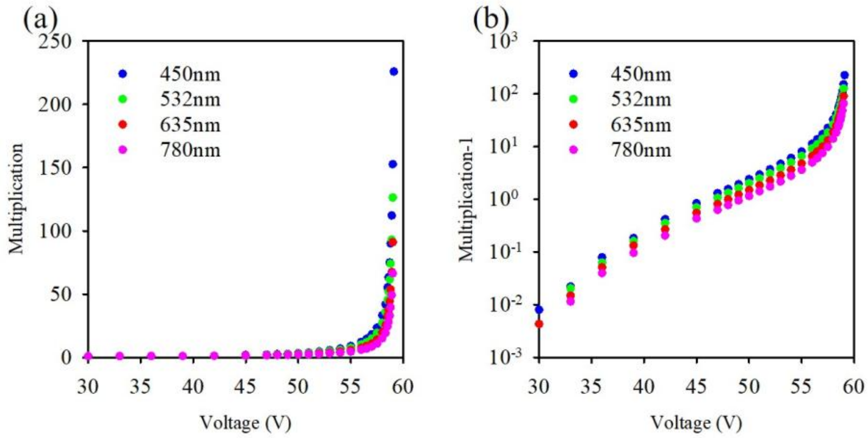

Figure 4.15 (a) Multiplication and (b) Multiplication-1 of 200 µm diameter device from sample OSU2022 at 450nm(blue dots), 532nm(green dots), 635nm(red dots), 780nm(purple dots).

As shown in Figure 4.16, the wavelength dependent multiplication results from TUoS and OSU show a high degree of similarity. The difference is within 1% from 35 V to 55 V and after 55 V, due to the different measurement methods and different wavelengths, the difference increases to 5%. The multiplication from TUoS can go up to 245 when that from OSU can go to 90.

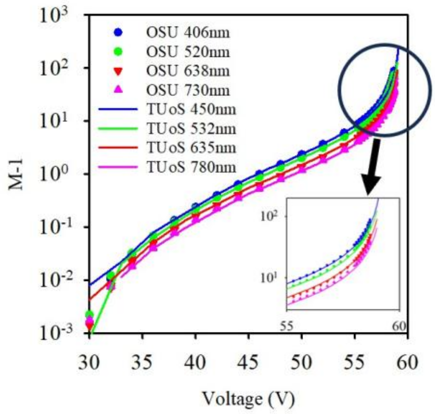

Figure 4.16 Multiplication results from TUoS campared to that from OSU.

4.5.2 Impact ionization coefficient

According to the error range from SIMS and CV fitting, the i-region thickness will range from 987 nm to 1007 nm, so different thickness assumption will be made in this section. Multiplication data from OSU will be used to do the fitting in this part due to the lower photocurrent.

As shown in Figure 4.17, (a) and (b) are the fitting results at different wavelength and the i-region thickness is fixed to be 987 nm. Similar, (c) and (d) use 990.5 nm, (e) and (f) is 997 nm, (g) and (h) are 1007 nm. Multiplication with 406nm light is used to be M_e and other wavelengths are M_{mix}. The absorption coefficients used for 520 nm, 638 nm, 730 nm are 48140, 10250 and 4000 cm-1 respectively. And for all the fitting, the diffusion length is set as 0.1 μm. It is clear that a tiny change in the i-region thickness will not significantly change the absolute values of α and β. α behaviours similar to AlAsSb[32] in high electric filed but reduces heavily at low electric field. Also, β shows the similar trend compared to AlAsSb. When comparing to InAlAs[33] , it has a large difference, β is much lower than InAlAs.

All the α and β parameters are shown in Table 4.2 with different i-region thickness.

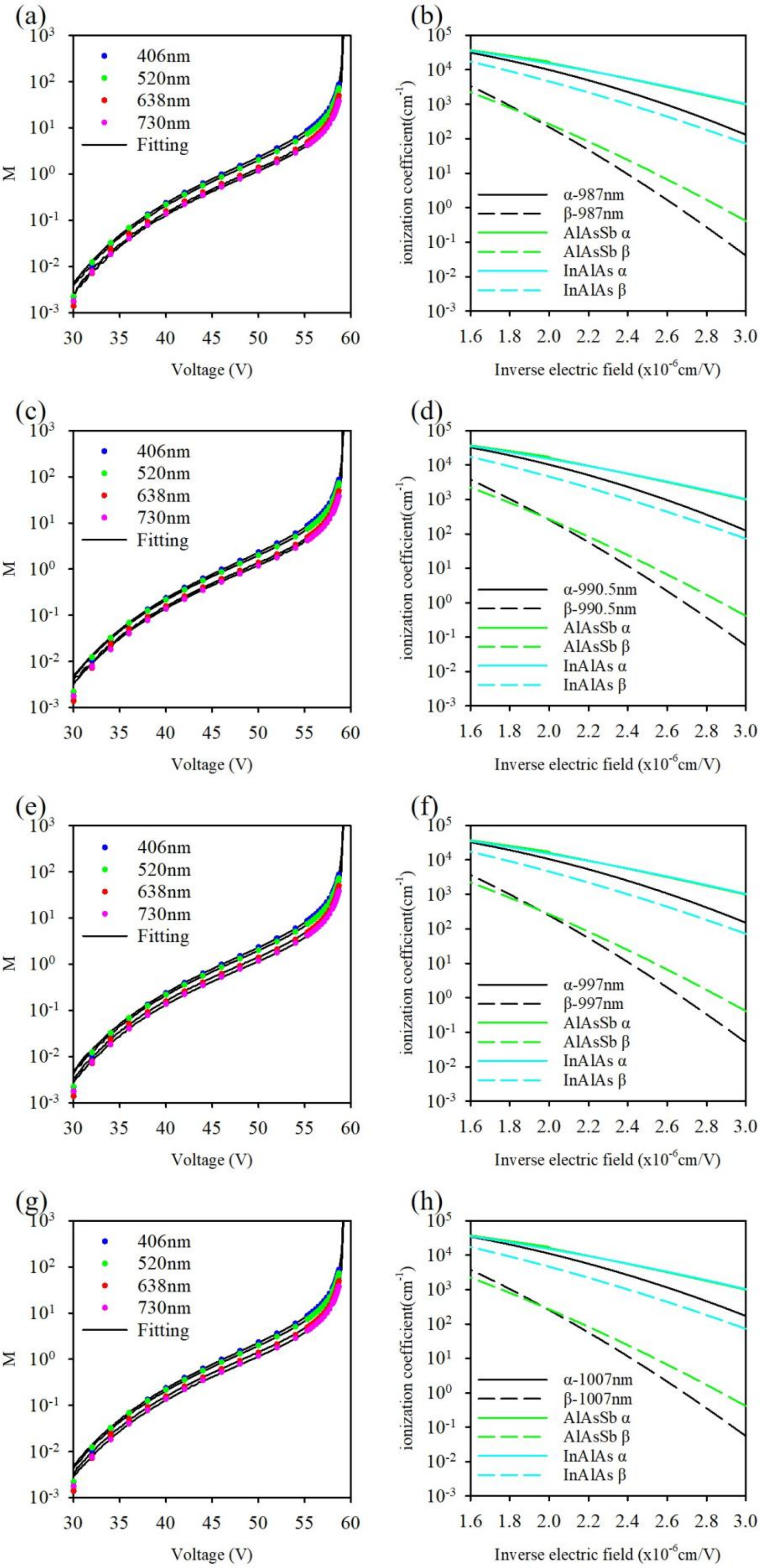
(a)
406nm
520nm
638nm
730nm
Fitting
M
Voltage (V)
(b)
α-987nm
β-987nm
AlAsSb α
AlAsSb β
InAlAs α
InAlAs β
ionization coefficient(cm-1)
Inverse electric field (x10-6cm/V)
(c)
406nm
520nm
638nm
730nm
Fitting
M
Voltage (V)
(d)
α-990.5nm
β-990.5nm
AlAsSb α
AlAsSb β
InAlAs α
InAlAs β
ionization coefficient(cm-1)
Inverse electric field (x10-6cm/V)
(e)
406nm
520nm
638nm
730nm
Fitting
M
Voltage (V)
(f)
α-997nm
β-997nm
AlAsSb α
AlAsSb β
InAlAs α
InAlAs β
ionization coefficient(cm-1)
Inverse electric field (x10-6cm/V)
(g)
406nm
520nm
638nm
730nm
Fitting
M
Voltage (V)
(h)
α-1007nm
β-1007nm
AlAsSb α
AlAsSb β
InAlAs α
InAlAs β
ionization coefficient(cm-1)
Inverse electric field (x10-6cm/V)

Figure 4.17 (a) Multiplication and fitting (b) α and β with 987nm i-region thickness; (c) Multiplication and fitting (d) α and β with 990.5nm i-region thickness; (e) Multiplication and fitting (f) α and β with 997nm i-region thickness; (g) Multiplication and fitting (h) α and β with 1007nm i-region thickness. All the α and β results are compared with AlAsSb[32] and InAlAs[33] .

Sample thickness (nm)		A (10^5 cm^{-1})	B (10^5 V cm^{-1})	C
987	α	1.8	8	2.26
	β	14.5	18.24	1.68
990.5	α	1.8	7.9	2.3
	β	14	18	1.68
997	α	1.8	7.93	2.26
	β	14.5	18.1	1.68
1007	α	2.1	8.2	2.18
	β	14.5	18.05	1.68

Table 4.2 Details of AlInAsSb impact ionization coefficients with different i-region assumptions.

When it comes to the α/β ratio of this material, it is shown in Figure 4.18. Compared to Xin's AlAsSb[32] , this material shows similar α/β ratio from inverse electric field of 1.6 to $3 \times 10^{-6} cm/V$. Also, the α/β ratio is significantly larger than InAlAs[33] . According to the large α/β ratio, the excess noise should be extremely low, and it will be discussed in the next session.

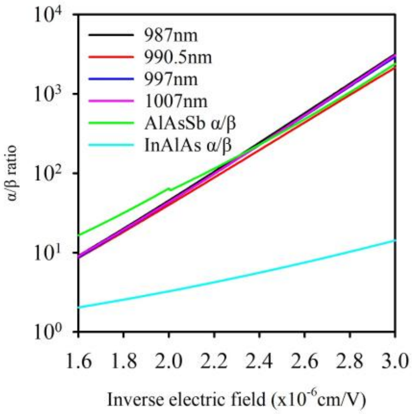

Figure 4.18 α/β ratio of AlInAsSb with different i-region assumptions.

4.6 Noise measurement

The excess noise setup is introduced in Chapter 3. All the noise measurements were done with a 10MHz±4MHz centre frequency circuit[33] . And the reference Si diode is used to calculate the k-value to get real excess noise. Different wavelength noise results on 200 um diameter devices are shown in Figure 4.19. In this p-i-n structure, wavelength comes from 455 nm to 780 nm and the injection function is from pure to mix. With the increasing of wavelength, the excess noise increases which is following the trend in multiplication measurements. This pure injection (blue dots) has equivalent k=0.04 in McIntyre's local model. This k value is 2 times lower than the predictions from the ionization coefficient analysis. It also indicates that this material shows $\alpha \gg \beta$.

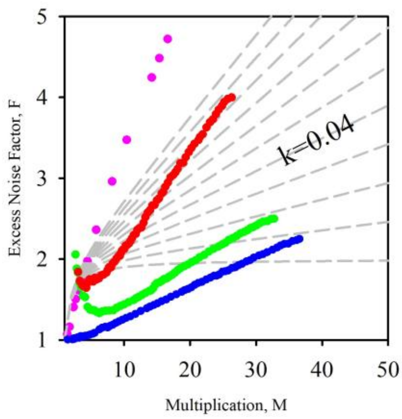

Figure 4.19 Measured excess noise (F) vs Multiplication (M) at different wavelength. Blue solid dots are 455nm, green solid dots are 520nm, red solid circles dots are 625nm and purple

solid dots are 780nm. Grey dash lines are McIntyre lines from 0 to 0.1 in the step of 0.01.

4.7 Discussion

Parameters	Value	Source
P-region thickness (nm)	300	SIMS
P-region doping (cm^{-3})	$2 \times 10^{18} cm^{-3}$	SIMS
I-region thickness (nm)	997	SIMS
I-region doping (cm^{-3})	$1 \times 10^{13} cm^{-3}$	SIMS
N-region thickness (nm)	100	SIMS
N-region doping (cm^{-3})	$2 \times 10^{18} cm^{-3}$	SIMS
Built in Voltage (V)	1.497	CV
Diffusion length (μm)	0.1	RPL model

Table 4.3 Parameters used in the analysis

In conclusion, the multiplication, ionization coefficients, and excess noise for the AlInAsSb alloy on an InP substrate were presented, over a field range of 0.33–0.6MV/cm. These results will assist in the design and analysis of high-performance SWIR SACM APDs with an AlInAsSb multiplication layer on manufacturable InP substrates. The demonstrated characteristics are all improvements over a commercially available SWIR APD incorporating InGaAs as the multiplier. The maximum demonstrated gain of 245 (a factor of 8 improvement), the relatively low dark current of $10^4\ A/cm^2$ (a factor of 10 improvement) at a gain of 30, and the low excess noise of 2.5 (a factor of 4 improvement) at a gain of 30 all demonstrate that this is a promising multiplier material for SWIR APD applications.

4.8 References

[1] R. A. Barton-Grimley et al., “Evaluation of the High Altitude Lidar Observatory (HALO) methane retrievals during the summer 2019 ACT-America campaign,” *Atmospheric measurement techniques*, vol. 15, no. 15, pp. 4623–4650, Aug. 2022, doi.org/10.5194/amt-15-4623-2022.

[2] X. Sun et al., “HgCdTe avalanche photodiode array detectors with single photon sensitivity and integrated detector cooler assemblies for space lidar applications,” *Optical Engineering*, vol. 58, no. 06, p. 1, Jun. 2019, doi.org/10.1117/1.oe.58.6.067103.

[3] Y. Li and J. Ibanez-Guzman, “Lidar for Autonomous Driving: The Principles, Challenges, and Trends for Automotive Lidar and Perception Systems,” IEEE Signal Processing Magazine, vol. 37, no. 4, pp. 50–61, Jul. 2020, doi.org/10.1109/msp.2020.2973615.

[4] R. J. McIntyre, “Multiplication noise in uniform avalanche diodes,” *IEEE Transactions on Electron Devices*, vol. ED-13, no. 1, pp. 164–168, Jan. 1966, doi.org/10.1109/t-ed.1966.15651.

[5] Md. M. Hossain, J. P. David, and M. M. Hayat, “Exact analytical formula for the excess noise factor for mixed carrier injection avalanche photodiodes,” *Journal of Lightwave Technology*, vol. 37, no. 13, pp. 3315–3323, Jul. 2019. doi:10.1109/jlt.2019.2914443

[6] D. S. Ong, A. H. Tan, K. Y. Choo, K. H. Yeoh, and J. P. David, “Weibull-fréchet random path length model for avalanche gain and noise in Photodiodes,” *Journal of Physics D: Applied Physics*, vol. 55, no. 6, p. 065105, Nov. 2021. doi:10.1088/1361-6463/ac31f0

[7] R. J. McIntyre, “A new look at impact ionization-PART I: A theory of gain, noise, breakdown probability, and frequency response,” *IEEE Transactions on Electron Devices*, vol. 46, no. 8, pp. 1623–1631, 1999. doi:10.1109/16.777150

[8] P. Yuan et al., “A new look at impact ionization-PART II: Gain and noise in short avalanche photodiodes,” IEEE Transactions on Electron Devices, vol. 46, no. 8, pp. 1632–1639, 1999. doi:10.1109/16.777151

[9] M. E. Woodson et al., “Low-noise AlInAsSb avalanche photodiode,” *Applied Physics Letters*, vol. 108, no. 8, Feb. 2016. doi:10.1063/1.4942372

[10] M. Ren et al., “Characteristics of $Al_xIn_{1-x}As_ySb_{1-y}$ (x: 0.3−0.7) Avalanche Photodiodes,” *Journal of Lightwave Technology*, vol. 35, no. 12, pp. 2380–2384, Jun. 2017. doi:10.1109/jlt.2017.2681041

[11] S. R. Bank et al., "Avalanche photodiodes based on the AlInAsSb Materials System," *IEEE Journal of Selected Topics in Quantum Electronics*, vol. 24, no. 2, pp. 1–7, Mar. 2018. doi:10.1109/jstqe.2017.2737880

[12] M. Ren et al., "AlInAsSb separate absorption, charge, and multiplication avalanche photodiodes," *Applied Physics Letters*, vol. 108, no. 19, May 2016. doi:10.1063/1.4949335

[13] A. H. Jones et al., "$Al_xIn_{1-x}As_ySb_{1-y}$ photodiodes with low avalanche breakdown temperature dependence," *Optics Express*, vol. 25, no. 20, p. 24340, Sep. 2017. doi:10.1364/oe.25.024340

[14] W. Sullivan et al., "Linear-mode HgCdTe avalanche photodiodes for photon-counting applications," Journal of Electronic Materials, vol. 44, no. 9, pp. 3092–3101, May 2015. doi:10.1007/s11664-015-3824-3

[15] "InGaAs APD G14858-0020AA: Hamamatsu Photonics," InGaAs APD G14858-0020AA | Hamamatsu Photonics.

[16] N. Li et al., "InGaAs/InAlAs Avalanche photodiode with undepleted absorber," *Applied Physics Letters*, vol. 82, no. 13, pp. 2175–2177, Mar. 2003. doi:10.1063/1.1559437

[17] Y. Zhao and S. He, "The experimental investigation on Dark Current for InGaAs–INP avalanche photodiodes," Microelectronic Engineering, vol. 98, pp. 19–23, Oct. 2012. doi:10.1016/j.mee.2012.06.001

[18] L. W. Cook, G. E. Bulman, and G. E. Stillman, "Electron and hole impact ionization coefficients in INP determined by photomultiplication measurements," *Applied Physics Letters,* vol. 40, no. 7, pp. 589–591, Apr. 1982. doi:10.1063/1.93190

[19] Y. Yuan et al., "Temperature dependence of the ionization coefficients of InAlAs and AlGaAs Digital Alloy: Erratum," *Photonics Research*, vol. 7, no. 3, p. 273, Feb. 2019. doi:10.1364/prj.7.000273

[20] J. Zheng et al., "Digital Alloy InAlAs Avalanche Photodiodes," Journal of Lightwave Technology, vol. 36, no. 17, pp. 3580–3585, Sep. 2018. doi:10.1109/jlt.2018.2844114

[21] D. S. Ong et al., "InAlAs avalanche photodiode with type-II superlattice absorber for detection beyond 2 µm," *IEEE Transactions on Electron Devices*, vol. 58, no. 2, pp. 486–489, Feb. 2011. doi:10.1109/ted.2010.2090352

[22] J. Xie, S. Xie, R. C. Tozer, and C. H. Tan, “Excess noise characteristics of thin AlAsSb APDs,” *IEEE Transactions on Electron Devices*, vol. 59, no. 5, pp. 1475–1479, May 2012. doi:10.1109/ted.2012.2187211

[23] C. H. Tan, S. Xie, and J. Xie, “Low noise avalanche photodiodes incorporating a 40 nm AlAsSb Avalanche region,” *IEEE Journal of Quantum Electronics*, vol. 48, no. 1, pp. 36–41, Jan. 2012. doi:10.1109/jqe.2011.2176105

[24] S. Lee et al., “High gain, low noise 1550 nm GaAsSb/AlGaAsSb avalanche photodiodes,” *Optica*, vol. 10, no. 2, p. 147, Jan. 2023. doi:10.1364/optica.476963

[25] S. Lee et al., “Random alloy thick AlGaAsSb avalanche photodiodes on InP substrates,” *Applied Physics Letters*, vol. 120, no. 7, Feb. 2022. doi:10.1063/5.0067408

[26] S. Lee et al., “Low noise $Al_{0.85}Ga_{0.15}As_{0.56}Sb_{0.44}$ avalanche photodiodes on InP substrates,” *Applied Physics Letters*, vol. 118, no. 8, Feb. 2021. doi:10.1063/5.0035571

[27] S. Lee et al., “Engineering of impact ionization characteristics in $In_{0.53}Ga_{0.47}As/Al_{0.48}In_{0.52}As$ superlattice avalanche photodiodes on InP substrate,” *Scientific Reports*, vol. 10, no. 1, Oct. 2020. doi:10.1038/s41598-020-73810-w

[28] S. H. Kodati et al., “AlInAsSb avalanche photodiodes on InP substrates,” *Applied Physics Letters*, vol. 118, no. 9, Mar. 2021. doi:10.1063/5.0039399

[29] T. J. Ronningen et al., “Ionization coefficients and excess noise characteristics of AlInAsSb on an InP substrate,” *Applied Physics Letters*, vol. 123, no. 13, Sep. 2023. doi:10.1063/5.0165800

[30] M. Moresco, F. Bertazzi, and E. Bellotti, “Gan Avalanche photodetectors: A full band Monte Carlo Study of gain, noise and bandwidth,” *IEEE Journal of Quantum Electronics*, vol. 47, no. 4, pp. 447–454, Apr. 2011. doi:10.1109/jqe.2010.2091257

[31] M. H. Woods, W. C. Johnson, and M. A. Lampert, “Use of a Schottky barrier to measure impact ionization coefficients in semiconductors,” *Solid-State Electronics*, vol. 16, no. 3, pp. 381–394, Mar. 1973. doi:10.1016/0038-1101(73)90013-0

[32] X. Yi et al., “Demonstration of large ionization coefficient ratio in $AlAs_{0.56}Sb_{0.44}$ lattice matched to INP,” Scientific Reports, vol. 8, no. 1, Jun. 2018. doi:10.1038/s41598-018-27507-w

[33] K. S. Lau et al., “Excess noise measurement in avalanche photodiodes using a transimpedance amplifier front-end,” *Meas. Sci. Technol.*, vol. 17, no. 7, pp. 1941–1946, 2006, doi: 10.1088/0957-0233/17/7/036.

5. CHAPTER 5: Ionization coefficient in GaAs/GaAsBi multiple quantum wells

5.1 Introduction

Semiconductor-based Avalanche Photodiodes are commonly used in place of standard photodiodes when photon availability is limited, as they enhance the sensitivity of optical systems[1] . APDs boost the Signal-to-Noise Ratio (SNR) through a process of internal multiplication (M) arising from the impact ionization of optically generated carriers when the semiconductor material is subject to a high electric field. The multiplication (or gain) of the signal, however, is usually accompanied by some extra 'excess' noise that arises due to the stochastic nature of the impact ionization process in semiconductors. In 1966 McIntyre defined this excess noise factor (F) as a function of the multiplication (M) as:[2]

$$F(M) = kM + (1-k)\left(2 - \frac{1}{M}\right) \tag{5.1}$$

Here, 'k' represents the ratio of the impact ionization coefficients for holes (β) and electrons (α), denoted as $k = \beta/\alpha$ for the case when electrons initiate the avalanche multiplication process. This excess noise sets a limit on the maximum useful multiplication for a given device before the SNR degrades. High-sensitivity APDs require a substantial SNR, necessitating the use of avalanche materials with a very low ' k ' value for electron-initiated multiplication. Semiconductor materials like HgCdTe[3] and InAs[4] have effectively no hole ionization and therefore provide near ideal multiplication with little or no excess noise; however, their narrow bandgaps mean that the devices have to be operated at cryogenic temperatures to reduce their thermally generated dark currents. The best example of a wider bandgap semiconductor capable of low dark currents at room temperature and possessing a small k is silicon[5] and AlGaAsSb[6] [7] . In an attempt to overcome the limitations of materials that have broadly similar α and β, considerable effort has gone into modifying material properties for example by using multiple quantum wells (MQWs)[8] or 'staircase' structures where band discontinuities are used to give carriers extra energy[9] , the use of quantum dot avalanching regions[10] , or by using nano-structuring to make one carrier type ionize more readily[11] . These have only demonstrated limited success to date and require careful design of the material combination and/or complicated growth and fabrication for this to work. Recently, the research showed that the addition of the large Group V atom, bismuth (Bi), to GaAs had a significant effect on reducing the hole ionization coefficients while leaving the electron ionization coefficients almost unaffected[12] . This was attributed to the effect of the band anti-crossing interaction of the large Bi atom on the GaAs valence band increasing the spin orbit splitting energy (Δso)[13] . Hole ionization in GaAs relies on holes from the heavy and light hole bands scattering into the split-off band from where they can easily gain sufficient energy to impact ionize[14] . Any increase in Δso reduces the population of holes in the split-off band and consequently reduces β. There are several challenges associated with the growth of thick GaAsBi layers. One problem with adding Bi to GaAs is that the compressive strain also increases such that the critical layer thickness[15] can be exceeded leading to the formation of misfit dislocations and higher dark currents. Relaxed GaAsBi shows improved surface roughness compared with relaxed InGaAs[16] ; however, relaxation still negatively affects the performance of GaAsBi devices[17] . Finding alternative ways to incorporate Bi into structures is therefore important if we are to use this idea to reduce k by reducing β.

In this chapter, it is demonstrated that thick, bulk GaAsBi structures are not required to reduce β. Introducing thin layers of GaAsBi as quantum wells (QWs) within a GaAs matrix can also enhance the performance of avalanching structures. A systematic study of the avalanche multiplication of a series of GaAsBi/GaAs MQW structures grown in a p-i-n configuration is undertaken for the first time and their ionization behaviours investigated from photomultiplication measurements. The β/α ratio in GaAs was decreased by suppressing hole impact ionization through a modification of the valence band structure. Bismuth (Bi), being one of the largest atoms that can be incorporated into GaAs, significantly perturbs the valence band structure due to the strong electronegativity difference between Bi and the arsenic (As) atoms it replaces, causing Bi to act as an isovalent impurity in GaAs. This leads to not only a significant narrowing of the bandgap via a band anticrossing interaction[18] , but more importantly for our interests, an increase in the valence band spin-orbit splitting energy.

5.2 Layer details

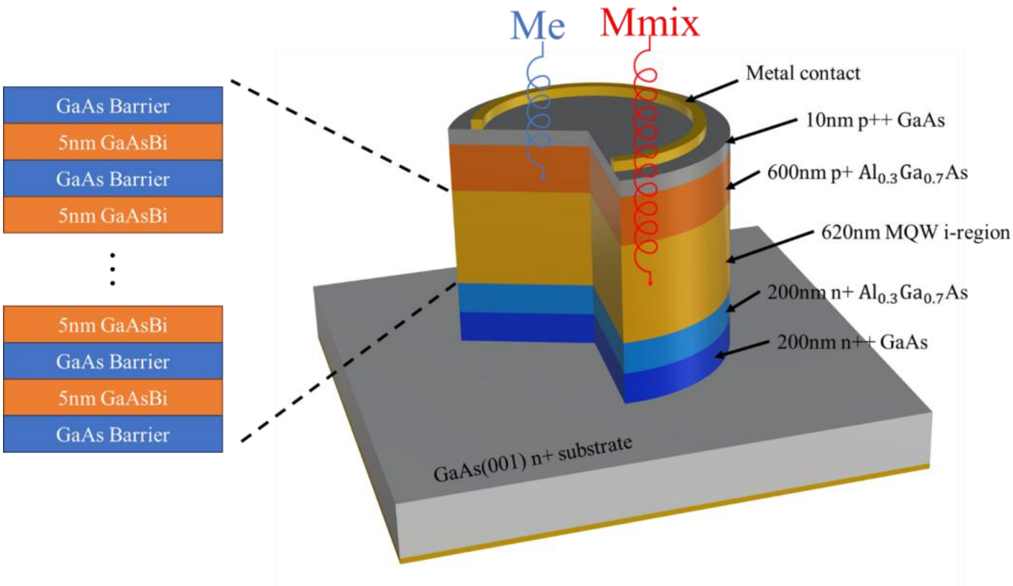

Figure 5.1 Schematic cross-section of the MQW p-i-n device structures used in this investigation

Layer	Number of periods, N	Barrier thickness (nm), L_B	i-region thickness (nm), w	$< MQW_{Bi\%} >$
QW05	5	101	630	0.15%
QW20	20	24	605	0.70%
QW40	40	10	605	1.43%
QW54	54	6	620	2.15%
QW63	63	4	582	2.38%

Table 5.1 Details of MQW structures investigated

A series of GaAsBi/GaAs multiple quantum well (MQW) p-i-n structures were grown on GaAs substrates with the layer structure shown in Figure 5.1. The growth was paused at each well-barrier interface in an attempt to prevent the accumulation of excess bismuth on the growing surface before growing the GaAs barrier[19] . The use of a multi-layer QW structure may allow a bismuth surfactant-like layer to be present on the surface to improve the material quality[20] , while preventing the deleterious accumulation of excess Bi on the surface that can cause roughness[21] . The nominal GaAsBi QW thickness (L_W) and Bi % (4.4 %) were determined from high resolution x-ray ω-2θ measurements (XRD), transmission electron microscopy (TEM) and photoluminescence (PL) measurements as 5 nm and 4.4 % Bi respectively[17] . The

5 nm QW thickness and 4.4% Bi was chosen to avoid exceeding the Matthews and Blakeslee critical layer thickness[15] whilst still incorporating an appreciable amount of Bi into the structures. Details of the numbers of MQW periods, which vary from 5 to 63 with corresponding barrier widths (L_B), are shown in Table 5.1[17] [22] . For the purposes of this study, the QWs in each MQW are assumed identical.

On the top and bottom of the MQW region are 600 nm of p+ $Al_{0.3}Ga_{0.7}As$ and 200 nm of n+ $Al_{0.3}Ga_{0.7}As$ respectively. These ensure that long wavelength light illumination is only absorbed in the MQW region. A thin 10 nm p+ GaAs contacting layer was grown to top the structure.

5.3 SIMS and TEM of MQWs

The SIMS results of QW40 are shown in Figure 5.2. The i-region thickness can be determined to be 605 nm from the calculation between Si and Be doping. However, due to the minimum step SIMS can do is large than 5 nm, it can not provide the well thickness in i-region, it can only show the stop point of Be and the start point of Bi and Si. Also, there is no reference of Bi so it can not provide accurate Bi doping level like Si and Be. The useful information can be got from it is the doping level of cladding layers and thickness of p+, i-region and n+. In (d), most of the Bi scan start and end points are in the same places respectively. Bi-1 starts from different point because of the calibration.

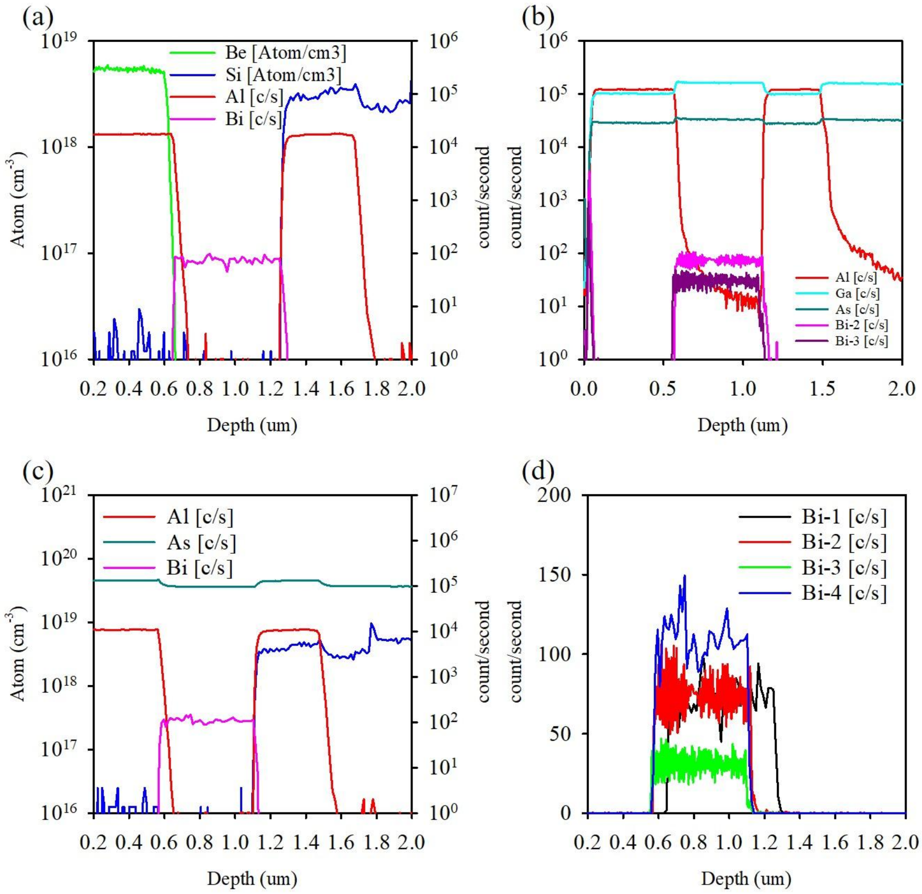

Figure 5.2 SIMS results of QW40

From the TEM in Figure 5.3 and Figure 5.4, the thickness of each QWs in all the samples are uniform. Details of how to interpolate the TEM is in reference [19] . Dislocation is clear in QW54 and QW63 which is not obvious in other samples. These dislocations will result in strain relaxation. It is clear that there are dislocations at the AlGaAs/GaAs interfaces in QW54 and QW63. According to the work done by Richards et al., the average Bi% is set as 4.4% and the well thickness is set to be 5 nm in this research. The calculation of the average Bi% content in the i-region ($MQW_{Bi\%}$) is shown below:

$$MQW_{Bi\%} = 4.4 \times N \times 5\ nm/w \tag{5.2}$$

where N is the number of QWs, and w is the total width of the i-region.

The TEM and SIMS of QW40 both show that i-region is 605 nm thickness.

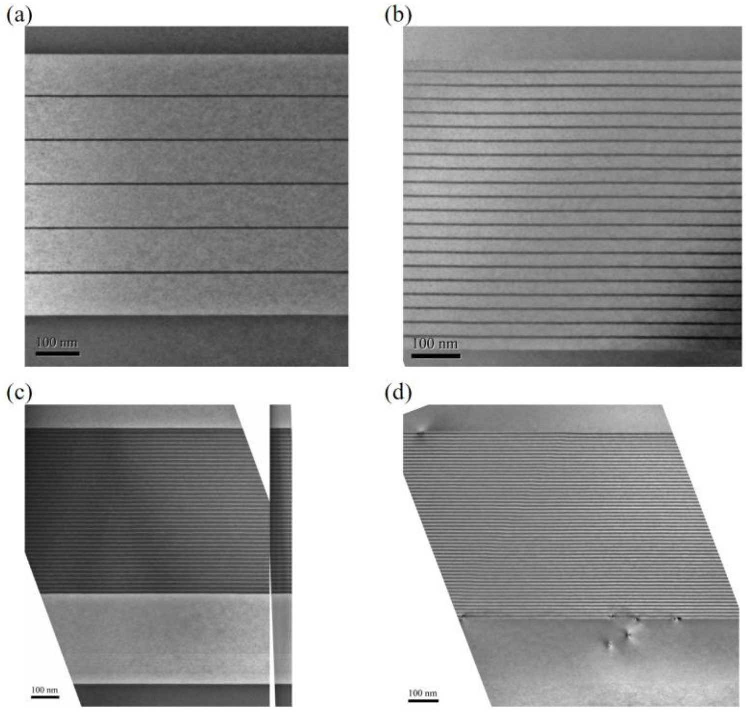

Figure 5.3 (a)-(d) TEM results of QW05, QW20, QW40 and QW54 respecitivily

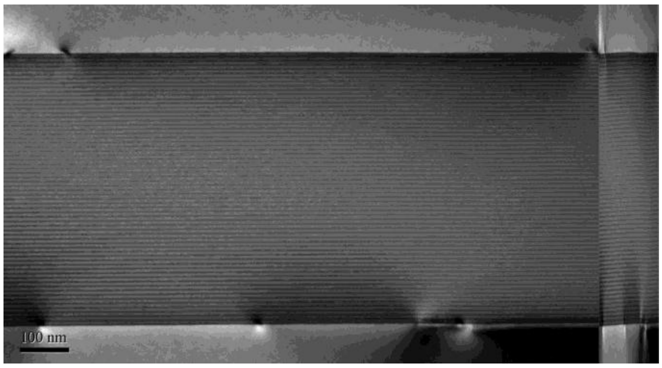

Figure 5.4 TEM of QW63

5.4 Electrical characterisation of MQWs

5.4.1 IV measurements

In Figure 5.5, the forward dark current shows that the bulk current dominants from 0 V and until 0.65 V the series resistance gets involved to affect the IV curve. Reverse dark IV shows that QW05 has 20 V breakdown voltage but the curves are not scale with area perfectly when the forward IV can.

Similar, in Figure 5.6, Figure 5.7, Figure 5.8, Figure 5.9, the dark current and density of other MQW samples are presented. For QW20, the forward current shows a linear line in log plot and scales with area. However, reverse IV not scales perfectly. The reverse dark IV of QW40 shows a different shape on different devices. When it comes to QW54, it has bad forward dark IV with high series resistance. Also, it may because of the dislocation. The reverse dark IV shows a smooth breakdown. For QW63, the reverse dark IV also shows different shape from different devices. It may because the non-uniformity of the growth. Detailed analysis is shown below.

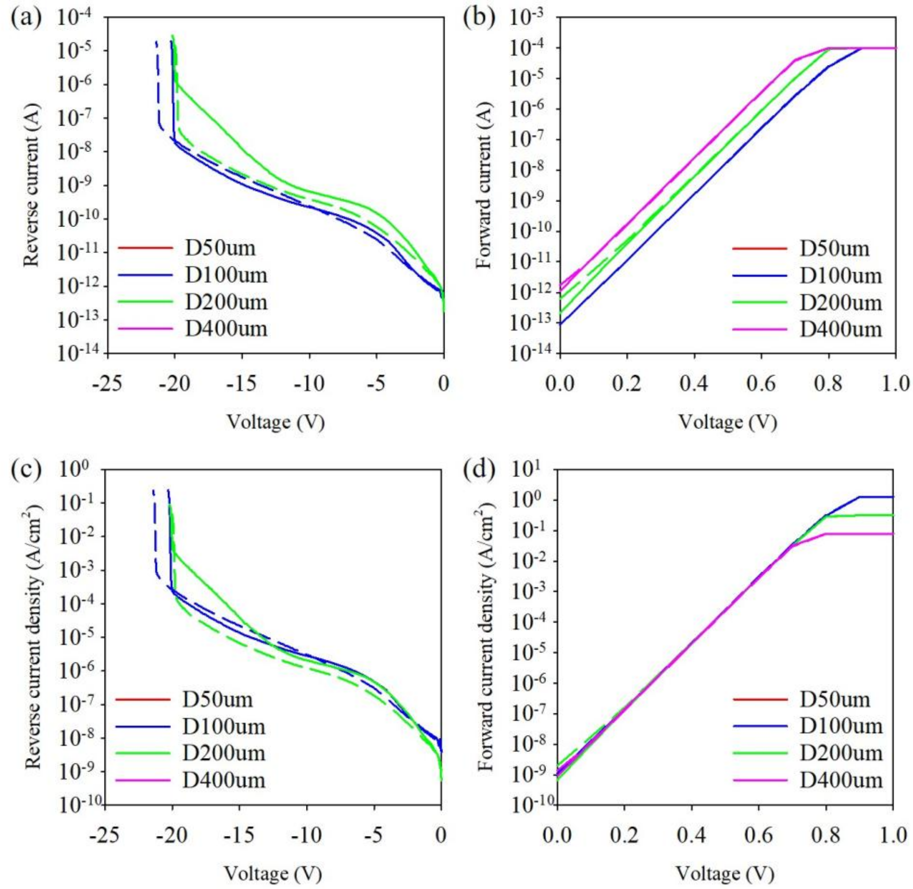

Figure 5.5 (a) Reverse dark current, (b) forward dark current, (c) reverse dark current density, (d) forward dark current density of QW05

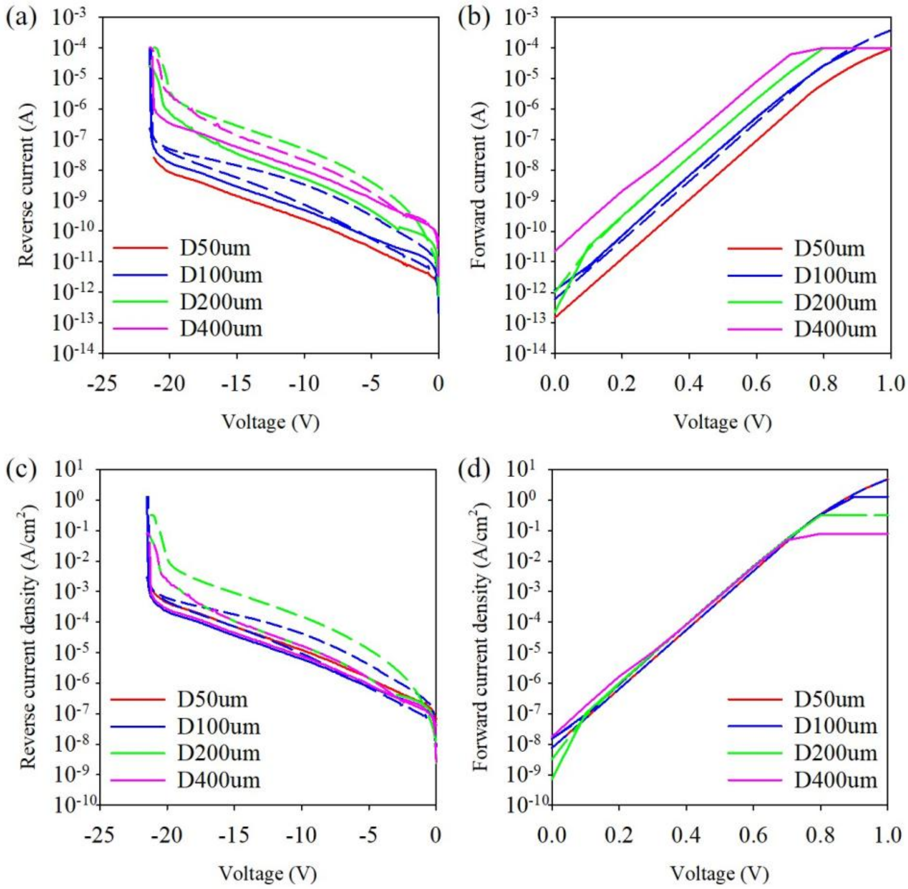

Figure 5.6 (a) Reverse dark current, (b) forward dark current, (c) reverse dark current density, (d) forward dark current density of QW20

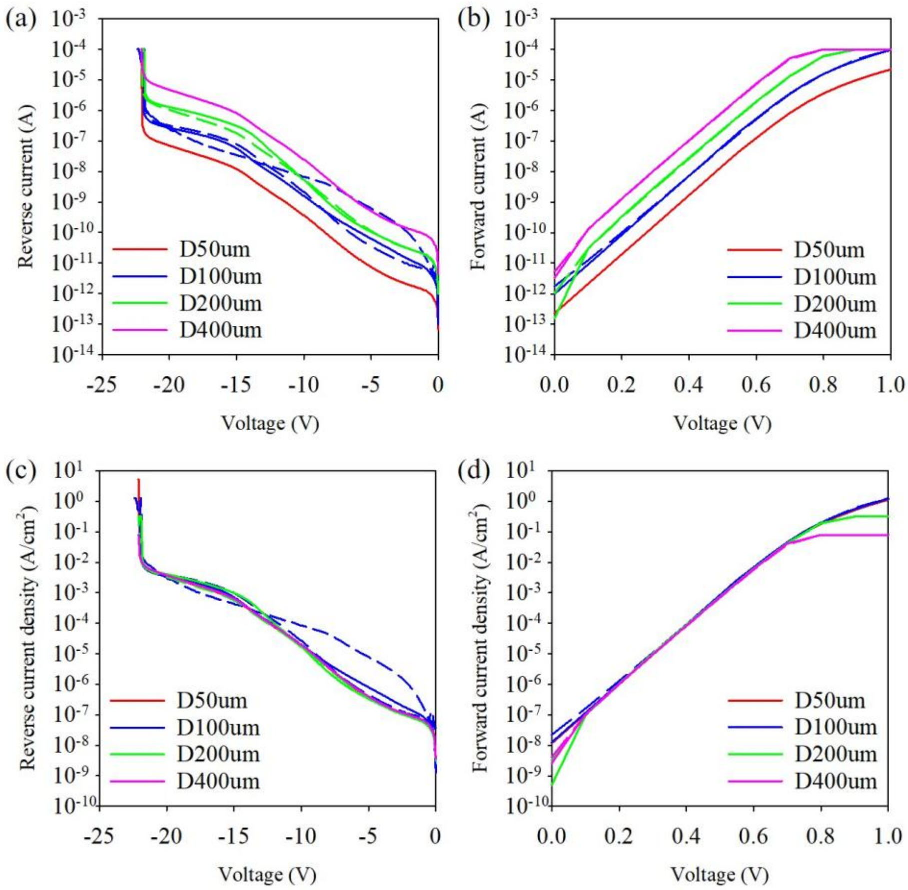

Figure 5.7 (a) Reverse dark current, (b) forward dark current, (c) reverse dark current density, (d) forward dark current density of QW40

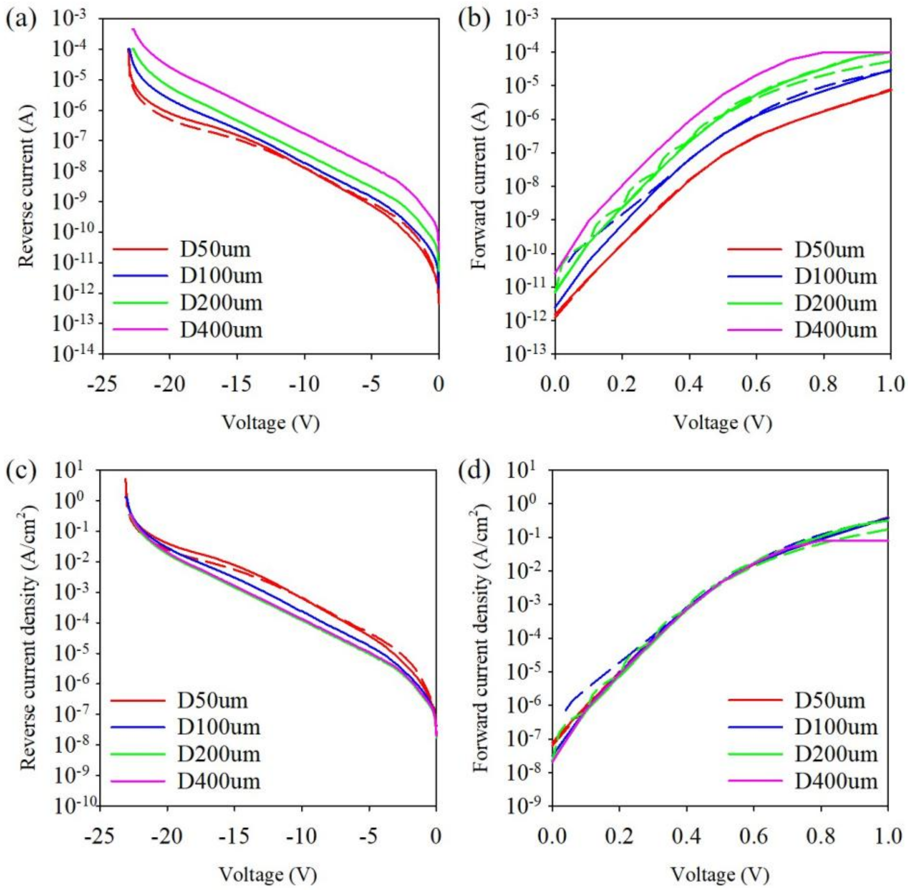

Figure 5.8 (a) Reverse dark current, (b) forward dark current, (c) reverse dark current density, (d) forward dark current density of QW54

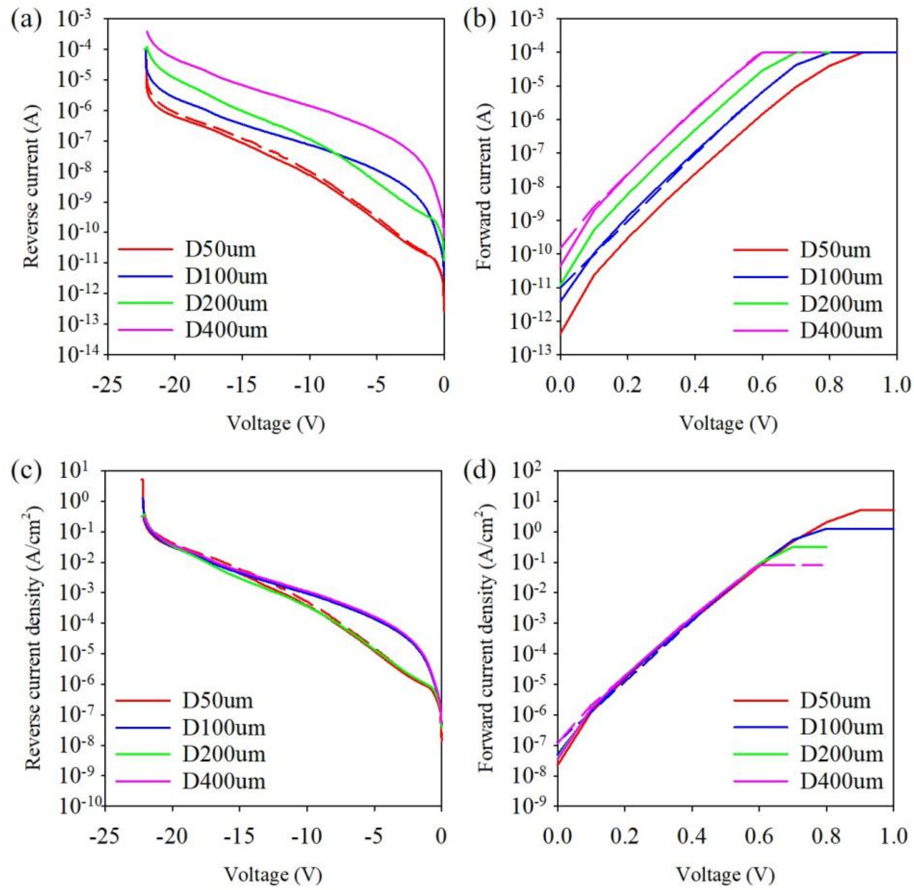

Figure 5.9 (a) Reverse dark current, (b) forward dark current, (c) reverse dark current density, (d) forward dark current density of QW63

As shown in Figure 5.10, both reverse and forward dark IV show that with the increasing of QW numbers, the dark IV increases. The forward JV is lower than 4% bulk GaAsBi samples 400 nm and 800 nm[12] . However, QW54 shows a different curve because of series resistance and strain relaxation. QW54 and QW63 both shows a magnitude higher forward JV. In the meanwhile, QW05, QW20 and QW40 has lower reverse dark JV compared to 4% GaAsBi. QW54 shows a lower dark JV before breakdown and QW63 is similar to 800nm 4% GaAsBi bulk sample. In assumption, QW63 has lower reverse dark JV compared to 4.4% 620 nm GaAsBi bulk sample.

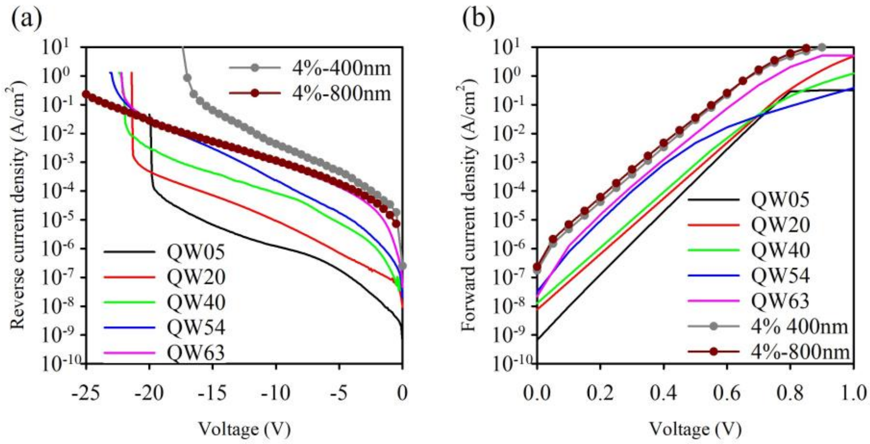

Figure 5.10 (a) Reverse dark current densities and (b) Forward dark current densities of the MQW p-i-n diodes compared with GaAs- $GaAs_{0.96}Bi_{0.04}$-GaAs p-i-n 400 nm and 800 nm samples[12] .

In Table 5.2 and Figure 5.11, the ideality factor, n is calculated by diode equation which is described in detail in chapter 2 and chapter 3. QW05 shows a lower n which is 1.58 and others are approximately 1.8., J_0 is calculated by JV fitting. J_0 of QW05 is 10 times lower than QW20 and as the number of quantum wells increases, the J_0 also increases.

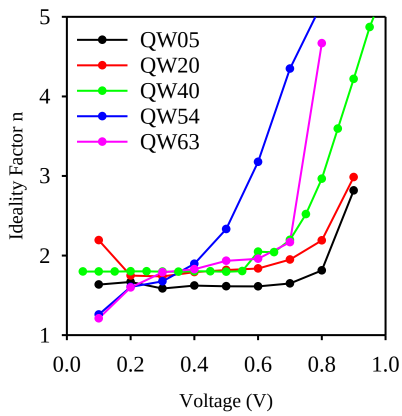

Figure 5.11 Ideality factor of each MQW verse voltage

Samples	$J_0(A/cm^2)$	Ideality Factor n
QW05	7.6×10^{-10}	1.58
QW20	7.6×10^{-9}	1.8
QW40	1.3×10^{-8}	1.81
QW54	6.7×10^{-8}	1.8

QW63	1.7×10^{-7}	1.79

Table 5.2 Dark current density and ideality factor of each MQW from diode equation.

5.4.2 CV measurements

CV measurements setup is described in chapter 3. Several devices are measured on each MQW samples. From Figure 5.12 to Figure 5.16, most of the samples show that the CVs are not scale with area and this indicates the sizes of the devices are not exactly the same as they are labelled. For QW05, the error is within 5% and it will not affect the doping profile analysis. For QW20, the shape indicates that the doping in cladding layer is not uniform. For QW40 and QW54, they both show that the CV is not scale with area and even same size devices show different capacitance values. For QW63, most of the devices are scale with area.

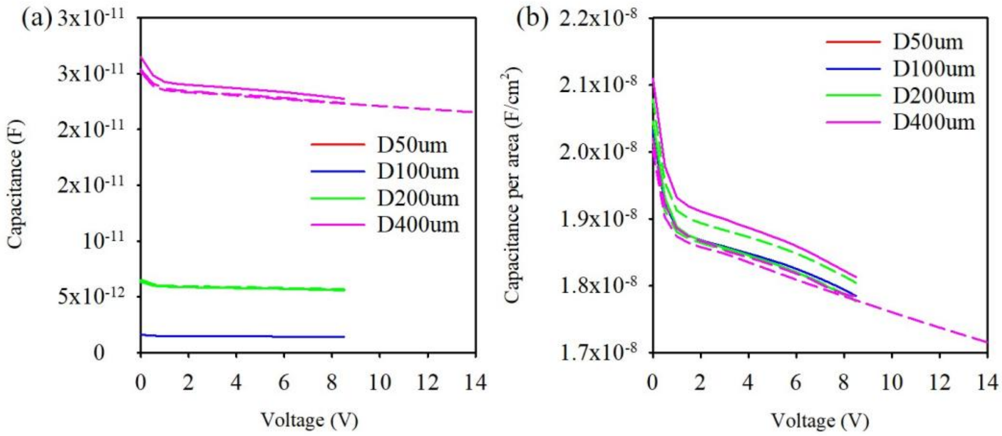

Figure 5.12 (a) CV data of QW05 (b) Capacitance per area of QW05.

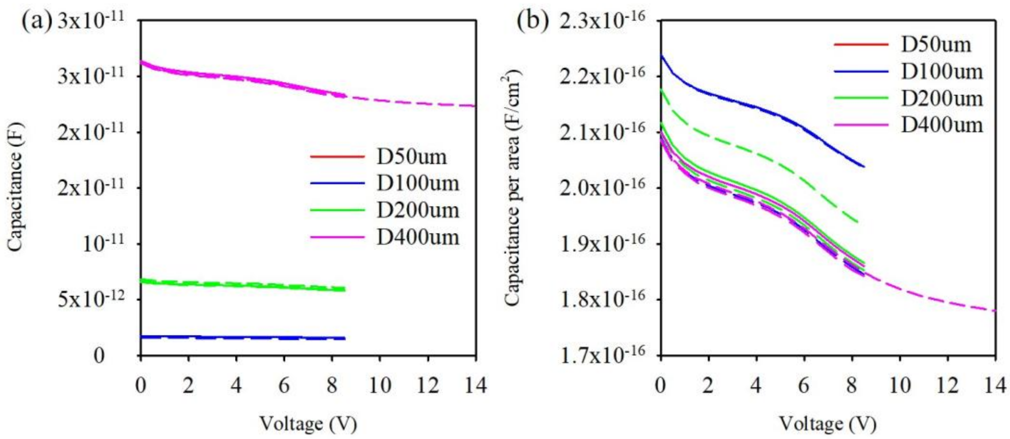

Figure 5.13 (a) CV data of QW20; (b) Capacitance per area of QW20.

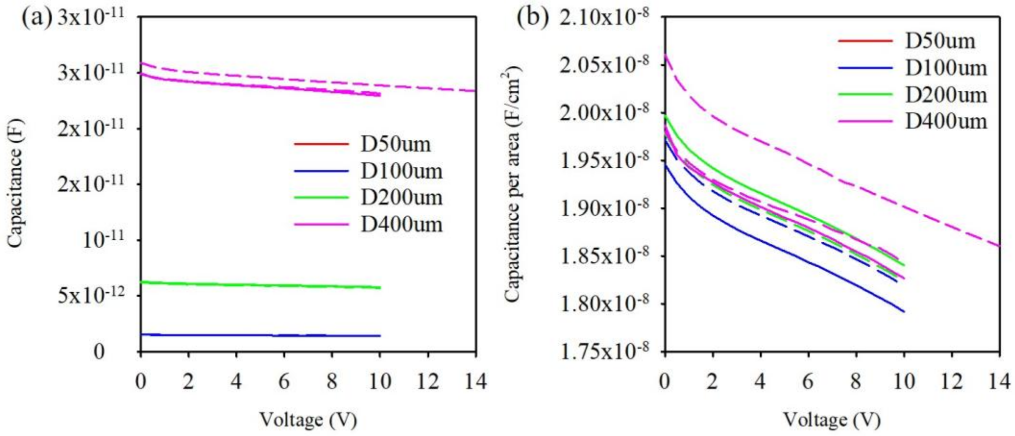

Figure 5.14 (a) CV data of QW40; (b) Capacitance per area of QW40.

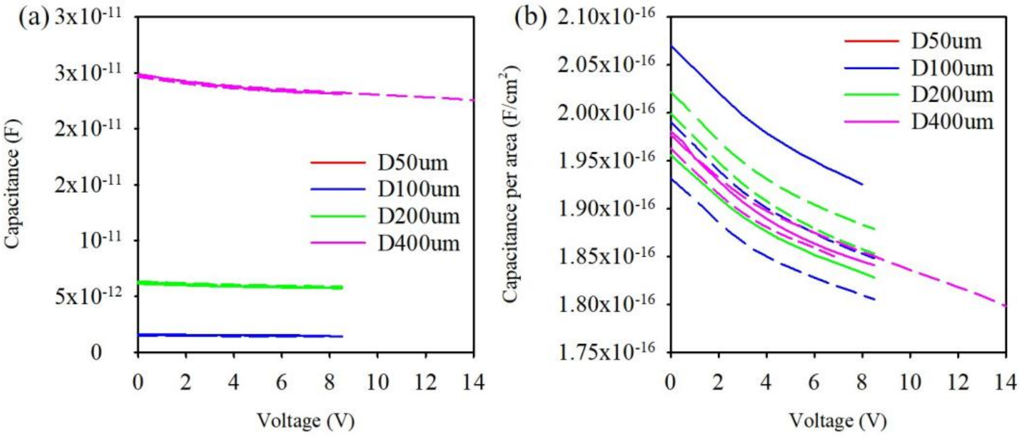

Figure 5.15 (a) CV data of QW54; (b) Capacitance per area of QW54.

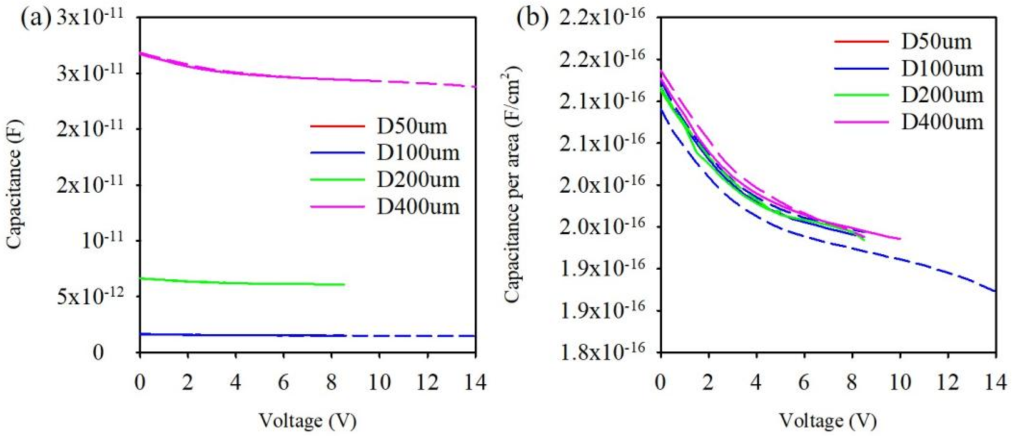

Figure 5.16 (a) CV data of QW63; (b) Capacitance per area of QW63.

Figure 5.17 shows the CV fitting of MQWs on 400 μm diameter devices and the estimated doping profile. The built-in voltage is estimated to be 1.2 V according to the $1/C^2$. The i-region thickness and doping density used to fit the CV results are shown in Table 5.3, also the error compared to the nominal i-region thickness is shown. It indicates that most of the samples are close to designed thickness and the largest error is 6% which is acceptable.

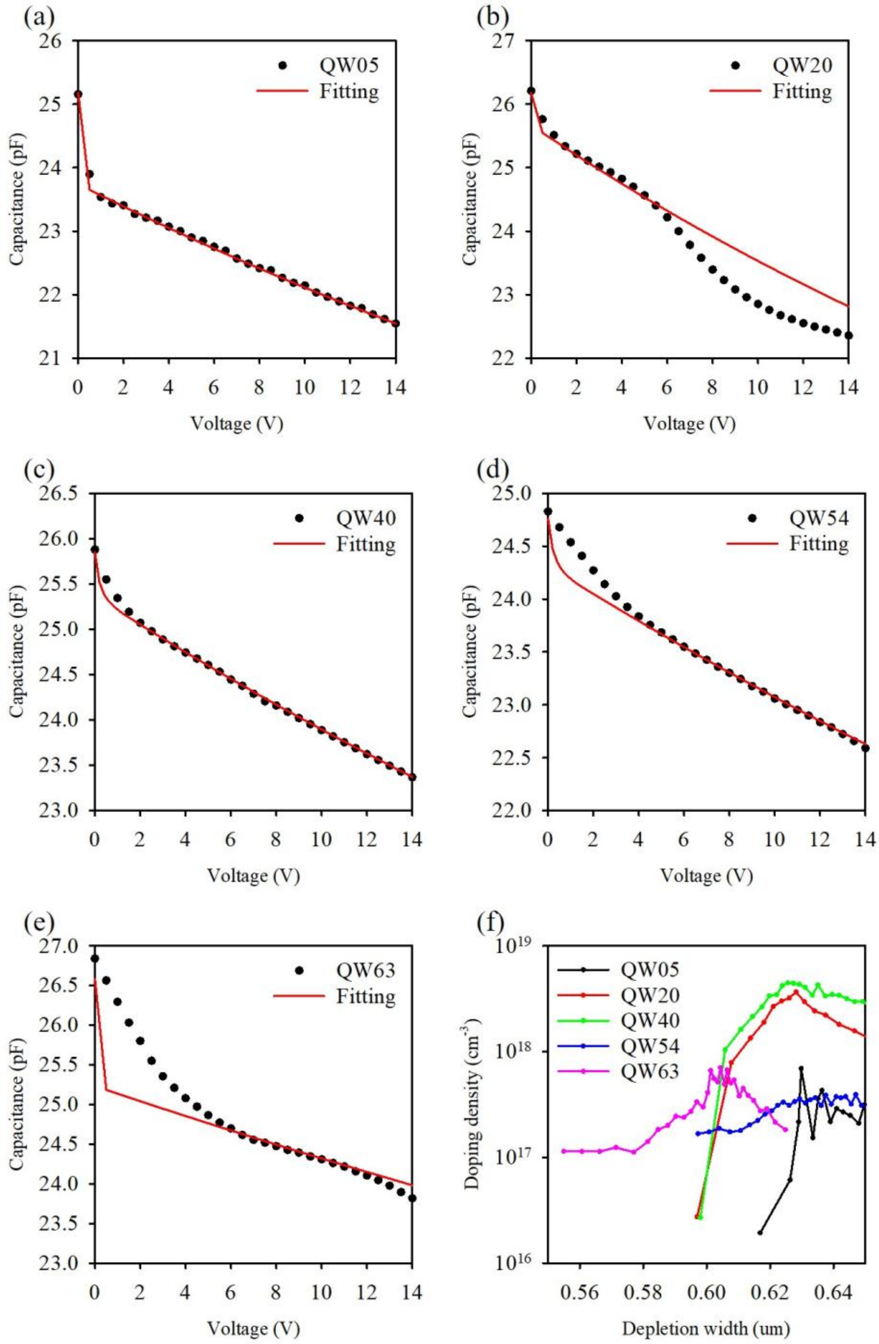

Figure 5.17 (a)-(e) Measured CV of MQWs series, black dots are raw data of each MQWs and solid red lines are fitting from Posion's equation, all raw data are from D400μm devices; (f) Dopping profile of MQWs.

Layer	Nominal i-region thickness(nm)	i-region doping ($10^{15}cm^{-3}$)	i-region thickness(nm)	Error (%)
QW05	620	4.7	630	+1.6
QW20	620	4.8	605	-2.4
QW40	620	4.78	605	-2.4
QW54	620	4.5	620	0
QW63	620	5.2	582	6.1

Table 5.3 CV model parameters compared with nominal thickness.

5.5 Photo spectrum of MQWs

The bias dependent photocurrent measurements on all samples were done in photocurrent setup. In Figure 5.18 (a)-(e), different biased photocurrent of each MQW from 0 V to -18 V are shown. In (a), there are two intersections, one is around 830nm which is bandgap of GaAs, and the other one is 1000 µm which is the bandgap of GaAsBi. This intersection is because of Franz-Keldysh effect. With the increasing of QW numbers, the intersection points wavelength increases from ~1000 nm to ~1100 um. The absorption coefficients shown in (f) are from the equation below:

$$\alpha = \frac{1}{w}\frac{hv}{q}\frac{1}{1-R}\frac{1}{\eta}\frac{I_{ph}}{\lambda} \tag{5.3}$$

Where w is the depletion width, R is the responsivity and λ is the wavelength.

Because of different thickness, MQWs show different cut off wavelength. And they have similar absorption coefficient at 980nm, and this absorption coefficient is used in the multiplication fitting in the next session.

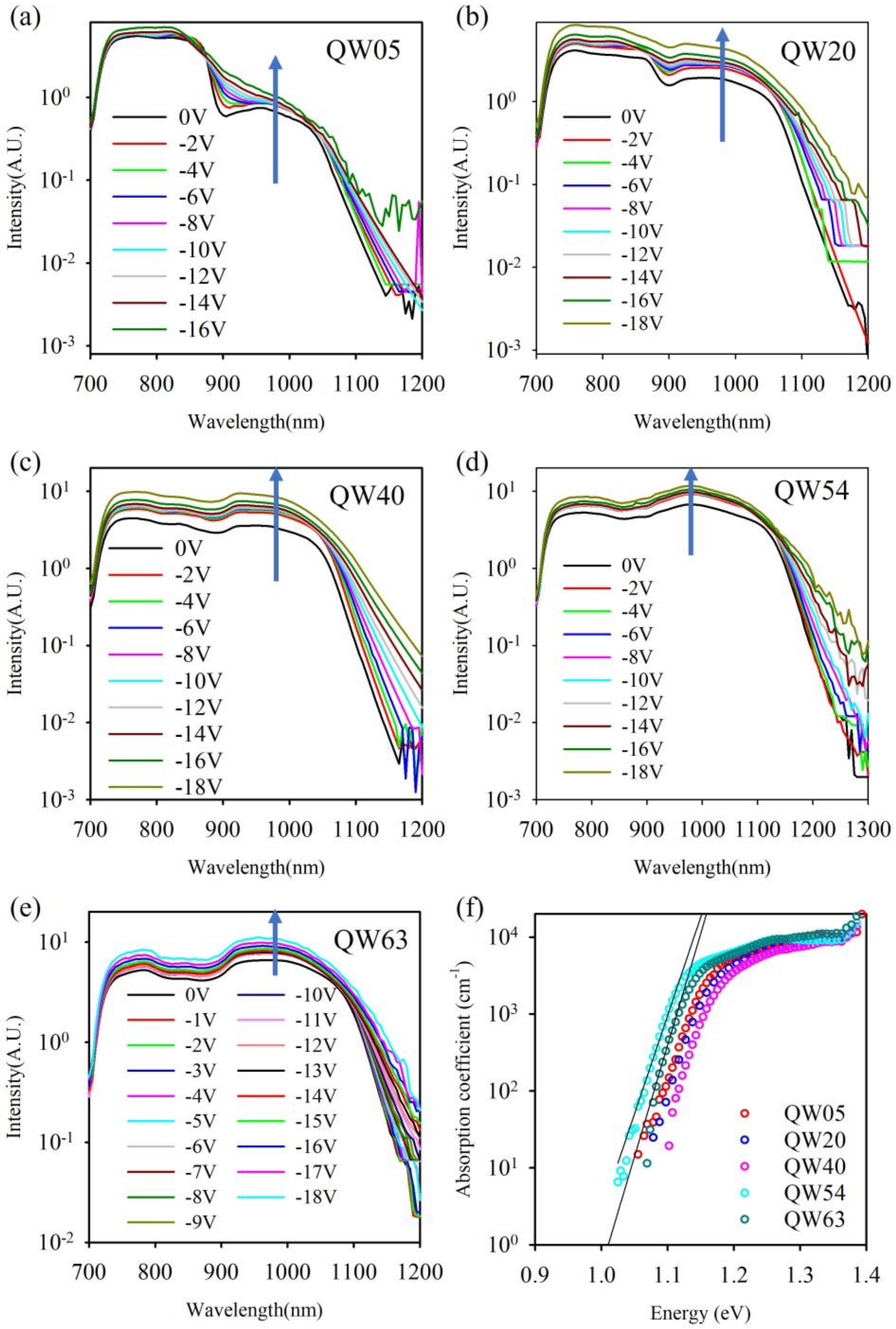

Figure 5.18 (a)–(e) Bias dependent photocurrent of MQWs; (f) Absorption coefficient of MQWs at 0V.

5.6 Photomultiplication characterisation of MQWs

In this section, all the key results are shown. From Figure 5.19 to Figure 5.23, multiplication at 450nm (blue dots), 532nm (green dots) and 980nm (purple dots) are plotted. All the solid black lines are the fitting using RPL model. All the model results come from local model. As multiplication at 450nm is similar to that at 532nm, so multiplication at 450nm is used to be M_e and multiplication at 980nm is used to be M_{mix}. All the fitting parameters are shown in the next session.

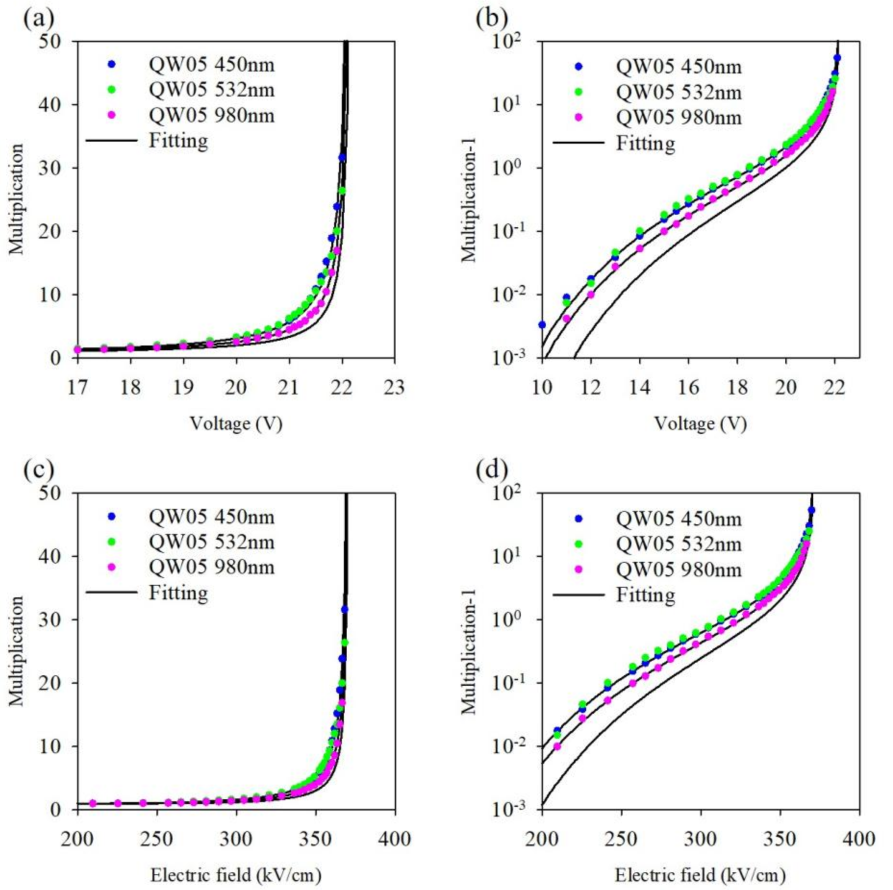

Figure 5.19 (a) M_e (blue dots), M_{532} (green dots) and M_{mix} (purple dots) of QW05 with RPL fitting (solid lines) at different voltage; (b) $M_e - 1$ (blue dots) , $M_{532} - 1$ (green dots) and $M_{mix} - 1$ (purple dots) of QW05 in log plot with RPL fitting (solid lines) at different voltage; (c) M_e (blue dots), M_{532} (green dots) and M_{mix} (purple dots) of QW05 with RPL fitting (solid lines) at different electric field; (d) $M_e - 1$ (blue dots) , $M_{532} - 1$ (green dots) and $M_{mix} - 1$ (purple dots) of QW05 in log plot with RPL fitting (solid lines) at different electric field.

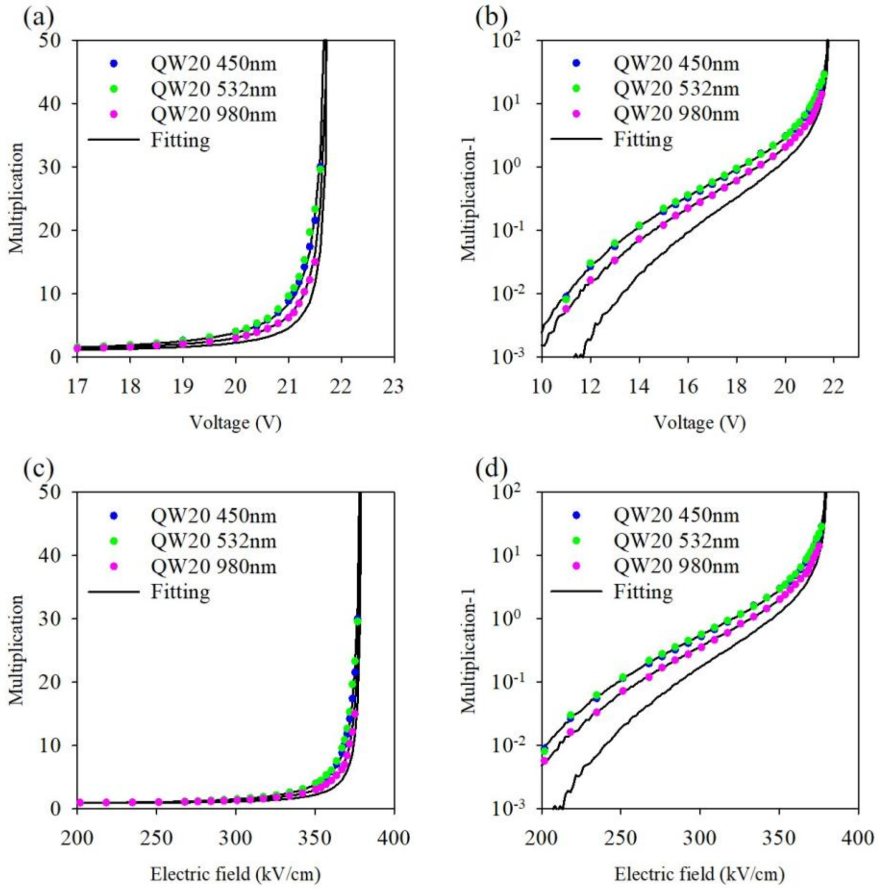

Figure 5.20 (a) M_e (blue dots), M_{532} (green dots) and M_{mix} (purple dots) of QW20 with RPL fitting (solid lines) at different voltage; (b) $M_e - 1$ (blue dots) , $M_{532} - 1$ (green dots) and $M_{mix} - 1$ (purple dots) of QW20 in log plot with RPL fitting (solid lines) at different voltage; (c) M_e (blue dots), M_{532} (green dots) and M_{mix} (purple dots) of QW20 with RPL fitting (solid lines) at different electric field; (d) $M_e - 1$ (blue dots) , $M_{532} - 1$ (green dots) and $M_{mix} - 1$ (purple dots) of QW20 in log plot with RPL fitting (solid lines) at different electric field.

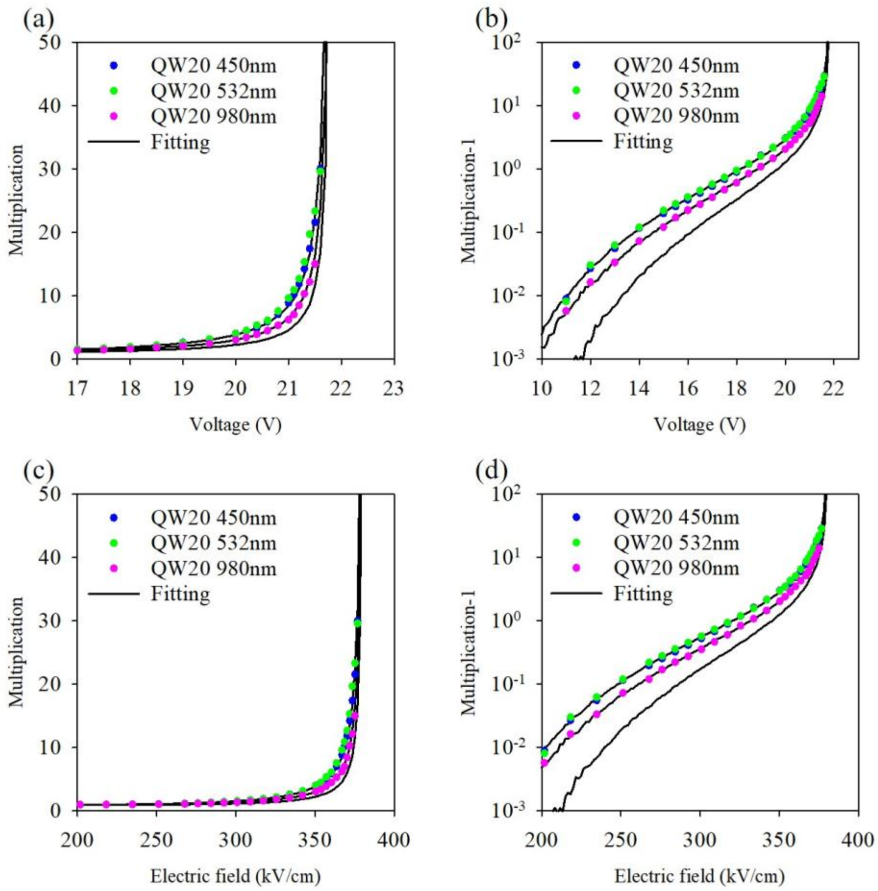

Figure 5.21 (a) M_e (blue dots), M_{532} (green dots) and M_{mix} (purple dots) of QW40 with RPL fitting (solid lines) at different voltage; (b) $M_e - 1$ (blue dots) , $M_{532} - 1$ (green dots) and $M_{mix} - 1$ (purple dots) of QW40 in log plot with RPL fitting (solid lines) at different voltage; (c) M_e (blue dots), M_{532} (green dots) and M_{mix} (purple dots) of QW40 with RPL fitting (solid lines) at different electric field; (d) $M_e - 1$ (blue dots) , $M_{532} - 1$ (green dots) and $M_{mix} - 1$ (purple dots) of QW40 in log plot with RPL fitting (solid lines) at different electric field.

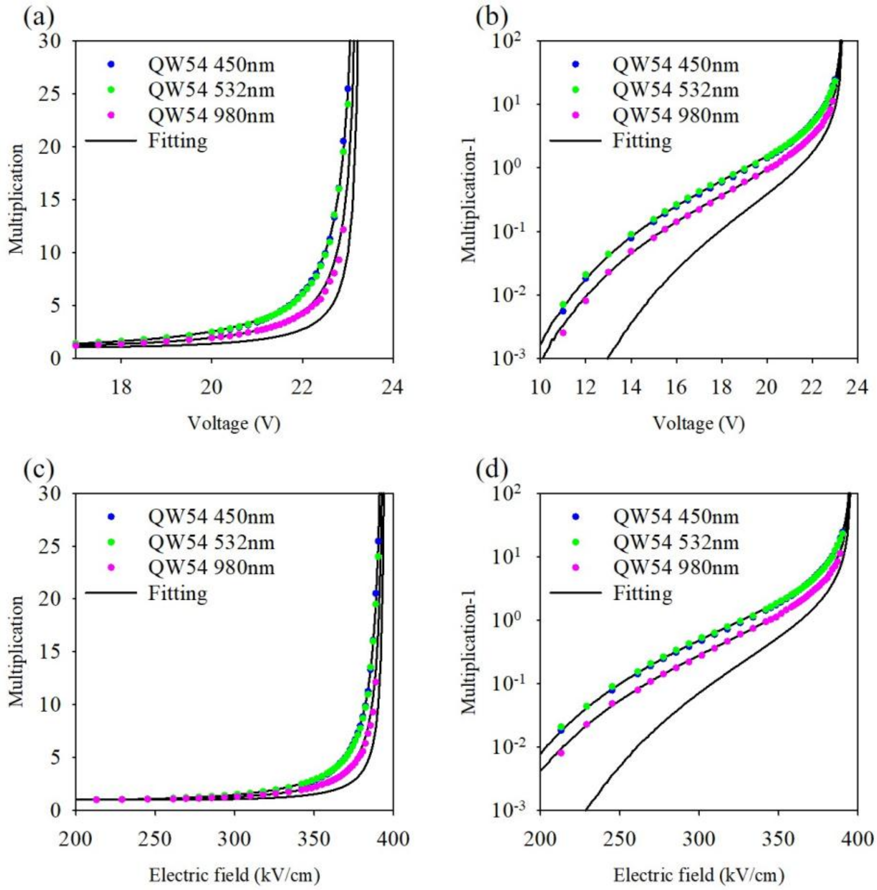

Figure 5.22 (a) M_e (blue dots), M_{532} (green dots) and M_{mix} (purple dots) of QW54 with RPL fitting (solid lines) at different voltage; (b) $M_e - 1$ (blue dots) , $M_{532} - 1$ (green dots) and $M_{mix} - 1$ (purple dots) of QW54 in log plot with RPL fitting (solid lines) at different voltage; (c) M_e (blue dots), M_{532} (green dots) and M_{mix} (purple dots) of QW54 with RPL fitting (solid lines) at different electric field; (d) $M_e - 1$ (blue dots) , $M_{532} - 1$ (green dots) and $M_{mix} - 1$ (purple dots) of QW54 in log plot with RPL fitting (solid lines) at different electric field.

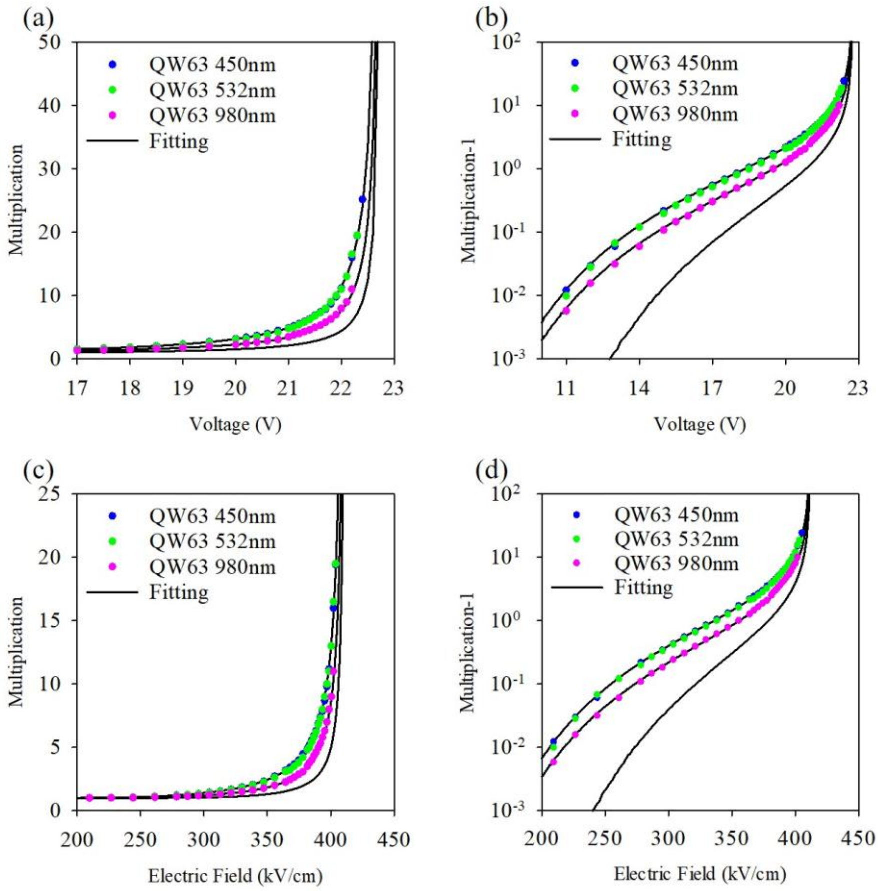

Figure 5.23 (a) M_e (blue dots), M_{532} (green dots) and M_{mix} (purple dots) of QW63 with RPL fitting (solid lines) at different voltage; (b) $M_e - 1$ (blue dots) , $M_{532} - 1$ (green dots) and $M_{mix} - 1$ (purple dots) of QW63 in log plot with RPL fitting (solid lines) at different voltage; (c) M_e (blue dots), M_{532} (green dots) and M_{mix} (purple dots) of QW63 with RPL fitting (solid lines) at different electric field; (d) $M_e - 1$ (blue dots) , $M_{532} - 1$ (green dots) and $M_{mix} - 1$ (purple dots) of QW63 in log plot with RPL fitting (solid lines) at different electric field.

When converting the voltage into electric field, the multiplication-1 results in Figure 5.24 are clear. More QW numbers will lead to higher Bi average percentage, and this will lead to higher breakdown electric field. It shows how M_e and M_{mix} vary with increasing number of wells (N) as a function of the reverse electric field. The data plotted as $log(M_e - 1)$, shows that the measurable onset of the ionization process (defined here as when M_e = 1.01) occurs at a threshold electric field of around 204 kV/cm and is almost independent of the number of QWs. The threshold electric field necessary for M_{mix} to occur, however, varies from 209 kV/cm for

QW05 and increases to 217 kV/cm for QW63.

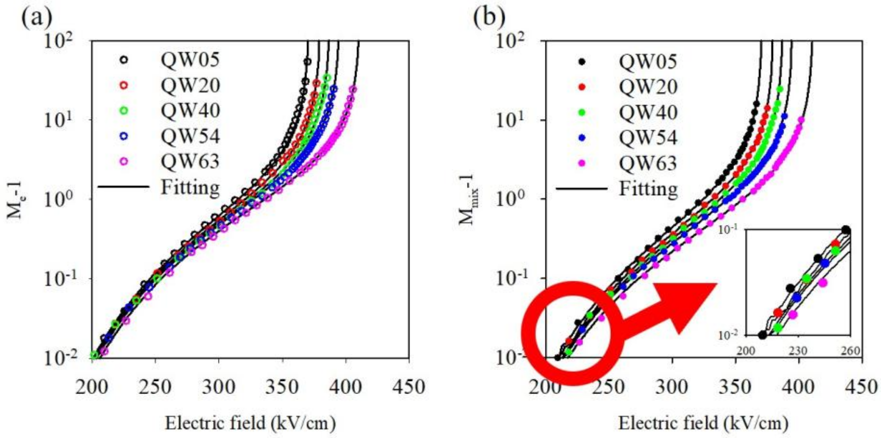

Figure 5.24 (a) $M_e - 1$ (dots) verse electric field of MQWs with RPL fitting (solid lines); (b) $M_{mix} - 1$ (980 nm)(dots) verse electric field of MQWs with RPL fitting (solid lines).

5.7 Impact ionization coefficient of MQWs

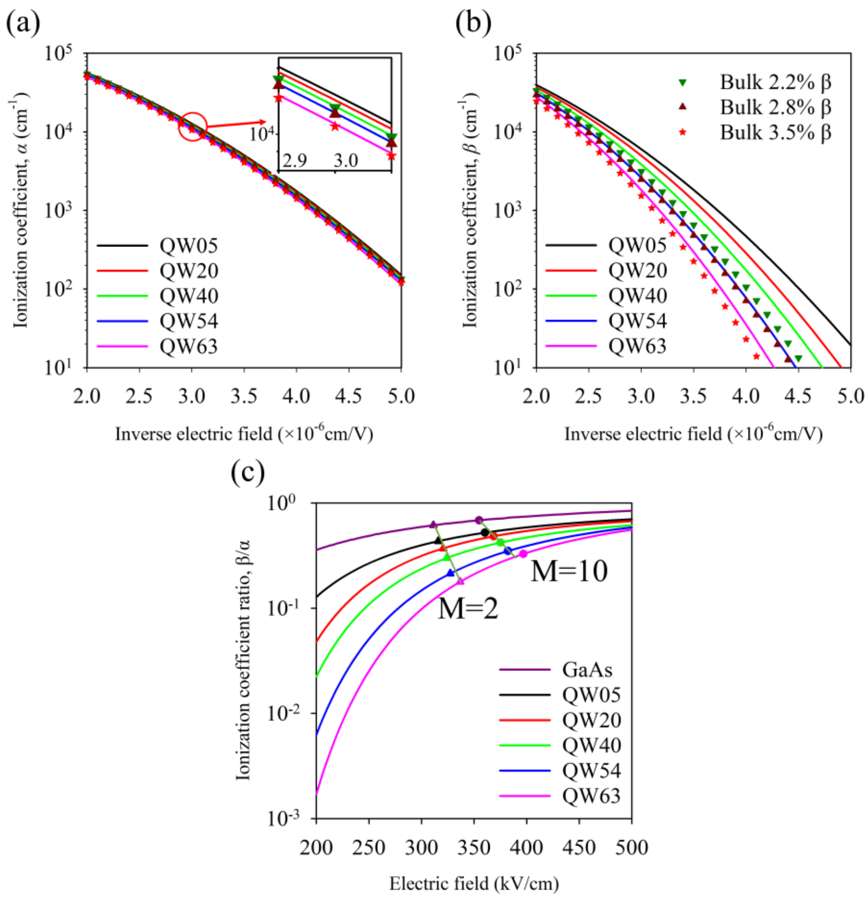

Figure 5.25 (a) α vs inverse electric field at a range of MQWs (solid lines) and bulk GaAsBi samples[12] , (b) β of GaAsBi vs inverse electric field for a range of MQWs and bulk GaAsBi samples[12] [12] , (c) β/α ratio of MQW samples and GaAs.

The impact ionization coefficients were determined from these multiplication measurements using a 'local' model that assumes carrier ionization at a given position within a device is a function solely of the electric field at that point (following the Chynoweth expression[26]), with no consideration of any 'dead space' [27] or history dependence of carrier energy[28] . This dead-space was found to reduce the multiplication only when the avalanching width was ≤ 0.1 μm[29] and so can be ignored in these structures.

For the p-i-n devices in this study, the carriers are generated by photon absorption (G_a) with an exponential decay profile dependent on the absorption coefficient (γ_λ),[30]

$$G_a(x) \propto e^{-\gamma_\lambda x} \tag{5.3}$$

For pure electron multiplication, all photo-generated carriers are generated prior to entering the multiplication region. In mixed multiplication, carriers are also photo-generated in the multiplier region. The observed, average multiplication is then dependent on the carrier generation function, $G(x)$, as

$$< M >= \frac{\int_0^w M(x)G(x)dx}{G(x)dx} \tag{5.4}$$

$$M(x_0) = \frac{exp \int_{x_0}^{w}(\alpha - \beta)dx}{1 - \int_0^w \alpha\ exp\left[-\int_0^x (\alpha - \beta)dx'\right]dx} \tag{5.5}$$

where $M(x_0)$ is the multiplication due to the injection of an electron−hole pair at position x_0, between the high field region 0 to w. In the case of p-i-n or n-i-p structures where a constant electric field can be assumed to exist between 0 to w, and only pure electrons or holes initiate the multiplication, this can be simplified to:

$$M_e = \frac{1}{1 - \frac{\alpha}{\beta - \alpha}\{exp[(\beta - \alpha)w] - 1\}} \tag{5.6}$$

$$M_h = \frac{1}{1 - \frac{\beta}{\alpha - \beta}\{exp[(\alpha - \beta)w] - 1\}} \tag{5.7}$$

The α and β can be expressed as:[26]

$$\alpha = A_n e^{-\left(\frac{B_n}{E}\right)^{C_n}} \tag{5.8}$$

$$\beta = A_p e^{-\left(\frac{B_p}{E}\right)^{C_p}} \tag{5.9}$$

The six coefficients—A_n, B_n, C_n, A_p, B_p, and C_p—are empirical coefficients that are determined from the best fit to the M_e and M_{mix} multiplication data. An absorption coefficient of 8000 cm^{-1} at 980 nm was assumed in this analysis. These are shown for the different structures in Table 2 and are valid for an electric field range of ~ 200 kV/cm to 400 kV/cm.

Figure 5.25 (a) and (b) show these ionization coefficients for these MQW GaAsBi devices over a wide electric field range. The effect of the increasing N (effectively an increasing $MQW_{Bi\%}$) is seen more clearly in Figure 5.25 (c) where the β/α ratio (k) is plotted as a function of electric field. Compared to GaAs, a significant decrease in k is observed (especially at lower electric fields) as N increases. The accuracy of these ionization coefficients is demonstrated by the Random Path Length (RPL) simulated M_e and M_{mix} values for the structures, replicating the measured data almost exactly over two orders of magnitude as shown by the lines from Figure 5.19 to Figure 5.24. While the α value only decreases by about 16 % between QW05 to QW63, the β value decreases by over two orders of magnitude at lower electric fields. Such highly dissimilar changes in ionization coefficients with increasing N appears to be uniquely related to the presence of GaAsBi.

Layer		A (10^5 cm^{-1})	B (10^5 V cm^{-1})	C
QW05	α	2.10	5.80	1.86
	β	2.00	6.45	1.9
QW20	α	2.05	5.81	1.86
	β	1.70	6.15	2.06
QW40	α	2.25	6.05	1.81
	β	1.78	6.40	2.06
QW54	α	2.20	6.07	1.81
	β	2.15	6.90	2.04
QW63	α	2.00	6.00	1.83
	β	2.10	7.00	2.1

Table 5.4 Details of MQW impact ionization coefficients.

5.8 Excess noise of QW40

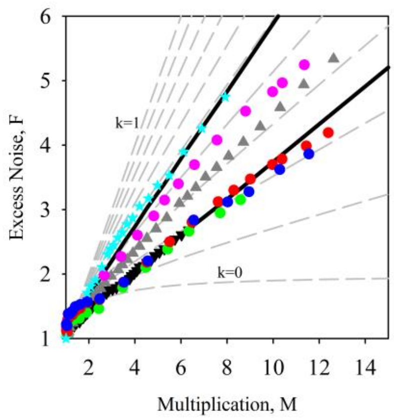

Figure 5.26 F_e results of QW40 (red, green and blue circles) compared to that of a similar thickness GaAs bulk sample from Li et al.[32] , (cyan star). F_{mix} of QW40 (purple circle), F_e of bulk 450 nm GaAsBi 2.3 % sample (grey triangle) and bulk 400 nm GaAsBi 4.0% bulk sample (black triangle) from Liu et al are also shown. The higher and lower black lines are RPL simulations for the bulk GaAs and QW40 respectively with model details as described in

the text.

In order to confirm the decrease seen in k with increasing number of QWs, excess noise measurements were undertaken as a function of multiplication on QW40. According to equation (5.1), this layer should have lower excess noise than a GaAs p-i-n structure. Measurements were undertaken using the excess noise set-up of Lau et al.[31] detailed in Chapter 3 with 455 nm and 780 nm wavelength illumination, which would correspond to M_e and M_{mix} respectively. The results obtained are shown in Figure 5.26. For comparison, a GaAs p-i-n sample with an equivalent 620 nm avalanche width would have an excess noise F vs M characteristic that follows an equivalent k of ~0.5[32] as shown. The F_e measured with 455 nm on QW40 however is significantly lower, corresponding to a k~0.2. Using 780 nm illumination gives rise to M_{mix} and therefore a higher F_{mix} and correspondingly larger k as expected. Figure 5.26 also shows the excess noise for a 450 nm thick bulk GaAsBi 2.3 % p-i-n and 400 nm thick bulk GaAsBi 4.0 % p-i-n[12] . Modelling the excess noise in structures with avalanching width < 1 μm requires the ionization probability density function (PDF) to be taken into consideration[32] as the McIntyre equation (5.1) is not capable of dealing with the 'dead-space' of the ionizing carriers. We have done this using a random path length model as described in the Methods with the ionization coefficients for GaAs[29] and GaAsBi from Table 5.4. The electron and hole threshold energies (E_{the} and E_{thh} respectively) used were E_{the} =2.3 eV and E_{thh} = 2.1 eV for GaAs and E_{the} =2.5 eV and E_{thh} = 3 eV for the QW40 to get the good agreement shown by the black lines in Fig. 7. While these values for GaAs are broadly in keeping with previously published data[33] , the values for QW40 are higher, suggesting that the hole ionization behaviour has been disproportionally affected.

5.9 Discussion

The $MQW_{Bi\%}$ varies from 0.15% to 2.38% for the QW5 to QW63 structures respectively as shown in Table 1. The multiplication behaviour of these MQW p-i-ns is qualitatively similar to the bulk p-i-n/n-i-p structures studied by Liu et al[12] with the breakdown fields increasing as $MQW_{Bi\%}$ increases due to the reduction in β. The onset of M_e occurs at almost the same electric field for all the devices (Figure 5.24 a) but the onset of M_{mix} (Figure 5.24 b) requires a slightly increasing electric field as the holes are also initiating the multiplication process. As in bulk

GaAsBi structures, the α hardly reduces as N increases in Figure 5.25 (a) compared to the β (Figure 5.25 (b)) which shows a significant reduction. A comparison with the α and β of bulk GaAsBi in Figure 5.25 (a) and Figure 5.25 (b) however shows that the MQW structure has reduced ionization coefficients, especially for β. The F_e for QW40 with $MQW_{Bi\%}$ of 1.43% in Figure 5.26 is also equivalent to that of a bulk GaAsBi 4.0%, albeit with a thinner 400 nm avalanche width. To explain the mechanism, we look at the band edge energies in GaAsBi as a function of Bi%, taken from Usman et al[13] as shown in Figure 5.27. At low Bi% the bandgap (E_g) of GaAsBi reduces because the conduction (E_C) band edge reduces and valence (E_V) band edges increase in energy. The split off band energy level (E_{SO}), however, also reduces slightly, resulting in an increase in the spin orbit splitting energy, Δ_{SO}. A consequence of this is to give rise to the bandstructure for the QW40 as shown in Fig. 8b. The band offsets at a GaAs to GaAsBi interface are typically 40:60 forΔ_{EC}: Δ_{EV}.[13] A simplistic analysis of the hole transport considering the valence band energies (shown by the black lines in Fig. 8b) might expect holes to ionize more readily in the GaAsBi quantum 'well', gaining energy from Δ_{EV}. However, the holes that initiate ionization will most likely have to do so from the spin split-off band[14] as in GaAs. Looking at the energy of holes in the blue split-off band in Fig. 8b, we can see that instead of gaining energy by falling into a GaAsBi 'well', the holes, actually see a small barrier due to the large increase in Δ_{SO} for the GaAsBi layer. This is similar to the observation by Czakjowski et al[34] that ionization by electrons in a AlGaAs/GaAs quantum well was determined by the band-offsets in the satellite valleys rather than Δ_{EC}. This may cause β to be reduced below that which may be expected from the $MQW_{Bi\%}$ only and explain the lower measured F_e for QW40. Introducing even a few bismuth-containing QW's appears to have a beneficial advantage in reducing $\beta$and this may be applied to other alloys as a way to reduce excess noise in APD structures.

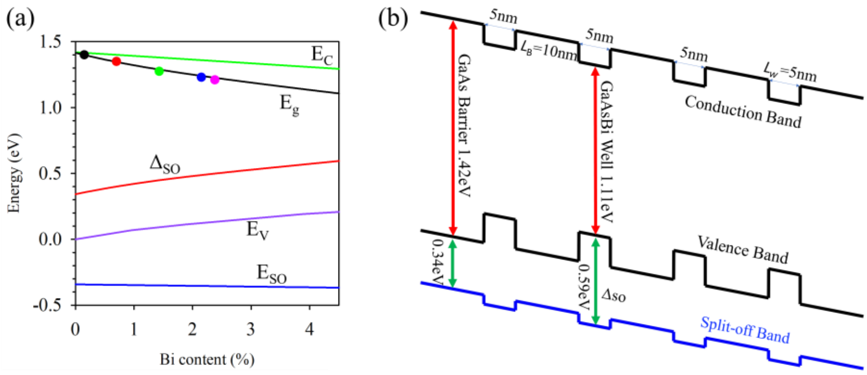

Figure 5.27 (a) The conduction band edge E_C, the bandgap energy E_g, the valence band edge E_V, the spin-split-off band energy E_{SO}, and the spin-orbit-splitting energy Δ_{SO} is plotted as the function of Bi content in $GaAs_{1-x}Bi_x$[13] . Coloured circles represent the five MQW structures in Table 5.1. (b) Diagram of the conduction, valence and split-off band energy levels of QW40.

5.10 References

[1] G. P. Agrawal, *Fiber‐optic communication systems*, Jun. 2021. doi:10.1002/9781119737391

[2] R. J. McIntyre, “Multiplication noise in uniform avalanche diodes,” *IEEE Transactions on Electron Devices*, vol. ED-13, no. 1, pp. 164–168, Jan. 1966. doi:10.1109/t-ed.1966.15651

[3] J. Beck et al., “The HgCdTe Electron Avalanche photodiode,” *Journal of Electronic Materials*, vol. 35, no. 6, pp. 1166–1173, Jun. 2006. doi:10.1007/s11664-006-0237-3

[4] A. R. Marshall, J. P. David, and C. H. Tan, “Impact ionization in InAs electron avalanche photodiodes,” *IEEE Transactions on Electron Devices*, vol. 57, no. 10, pp. 2631–2638, Oct. 2010. doi:10.1109/ted.2010.2058330

[5] “Si APD S16453-10K: Hamamatsu Photonics,” Si APD S16453-10K | Hamamatsu Photonics, https://www.hamamatsu.com/jp/en/product/optical-sensors/apd/si-apd/S16453-10K.html (accessed Mar. 23, 2024).

[6] X. Jin et al., “Very low excess noise Very Low Excess Noise $Al_{0.75}Ga_{0.25}As_{0.56}Sb_{0.44}$ Avalanche Photodiode,” *Optics Express*, vol. 31, no. 20, p. 33141, Sep. 2023. doi:10.1364/oe.500169

[7] S. Lee et al., “High Gain, Low Noise, Room Temperature 1550 nm GaAsSb/AlGaAsSb Avalanche Photodiodes,” *Optica*, vol. 10, no. 2, p. 147, Jan. 2023. doi:10.1364/optica.476963

[8] F. Capasso, Won-Tien Tsang, and G. F. Williams, “Staircase solid-state photomultipliers and avalanche photodiodes with enhanced ionization rates ratio,” *IEEE Transactions on Electron Devices*, vol. 30, no. 4, pp. 381–390, Apr. 1983. doi:10.1109/t-ed.1983.21132

[9] M. Ren et al., “AlInAsSb/GaSb staircase avalanche photodiode,” *Applied Physics Letters*, vol. 108, no. 8, Feb. 2016. doi:10.1063/1.4942370

[10] Y. Ma et al., “Enhanced carrier multiplication in InAs quantum dots for bulk avalanche photodetector applications,” *Advanced Optical Materials*, vol. 5, no. 9, Mar. 2017. doi:10.1002/adom.201601023

[11] A. C. Farrell et al., “Plasmonic field confinement for separate absorption-multiplication in InGaAs nanopillar avalanche photodiodes,” *Scientific Reports*, vol. 5, no. 1, Dec. 2015. doi:10.1038/srep17580

[12] Y. Liu et al., “Valence band engineering of GaAsBi for low noise avalanche photodiodes,” *Nature Communications*, vol. 12, no. 1, Aug. 2021. doi:10.1038/s41467-021-24966-0.

[13] M. Usman, C. A. Broderick, A. Lindsay, and E. P. O'Reilly, "Tight-binding analysis of the electronic structure of dilute bismide alloys of GaP and GaAs," Physical Review B, vol. 84, no. 24, Dec. 2011. doi:10.1103/physrevb.84.245202

[14] İ. H. Oğuzman, Y. Wang, J. Kolník, and K. F. Brennan, "Theoretical study of hole initiated impact ionization in bulk silicon and GaAs using a wave-vector-dependent numerical transition rate formulation within an ensemble Monte Carlo Calculation," Journal of Applied Physics, vol. 77, no. 1, pp. 225–232, Jan. 1995. doi:10.1063/1.359374

[15] J. W. Matthews and A. E. Blakeslee, "Defects in epitaxial multilayers: III. Preparation of almost perfect multilayers", *Journal of Crystal Growth*, vol. 32, no. 2, pp. 265–273, Feb. 1976. doi:10.1016/0022-0248(76)90041-5

[16] R. France, C.-S. Jiang, and A. J. Ptak, "In situ strain relaxation comparison between GaAsBi and GaInAs grown by molecular-beam epitaxy," *Applied Physics Letters*, vol. 98, no. 10, Mar. 2011. doi:10.1063/1.3562952

[17] R. D. Richards et al., "Photovoltaic characterisation of GaAsBi/GaAs multiple quantum well devices," *Solar Energy Materials and Solar Cells*, vol. 172, pp. 238–243, Dec. 2017. doi: 10.1016/j.solmat.2017.07.029

[18] K. Alberi et al., "Valence band anticrossing in $GaBi_xAs_{1-x}$," *Applied Physics Letters*, vol. 91, no. 5, Jul. 2007. doi:10.1063/1.2768312

[19] R. D. Richards, F. Bastiman, D. Walker, R. Beanland, and J. P. David, "Growth and Structural Characterisation of GaAsBi/GaAs Multiple Quantum Wells," *Semiconductor Science and Technology*, vol. 30, no. 9, p. 094013, Jul. 2015. doi: 10.1088/0268-1242/30/9/094013

[20] D. Fan et al., "MBE grown GaAsBi/GaAs double quantum well separate confinement heterostructures," *Journal of Vacuum Science & Technology B, Nanotechnology and Microelectronics: Materials, Processing, Measurement, and Phenomena*, vol. 31, no. 3, Feb. 2013. doi:10.1116/1.4792518

[21] A. J. Ptak et al., "Kinetically limited growth of GaAsBi by molecular-beam epitaxy," Journal of Crystal Growth, vol. 338, no. 1, pp. 107–110, Jan. 2012. doi: 10.1016/j.jcrysgro.2011.10.040

[22] R. D. Richards et al., "MBE grown GaAsBi/GaAs multiple quantum well structures: Structural and optical characterisation," *Journal of Crystal Growth*, vol. 425, pp. 237–240, Sep. 2015. doi: 10.1016/j.jcrysgro.2015.02.053

[23] B. Monemar, K. K. Shih, and G. D. Pettit, "Some optical properties of the $Al_xGa_{1-x}As$ alloys system", Journal of Applied Physics, vol. 47, no. 6, pp. 2604–2613, Jun. 1976. doi:10.1063/1.322979

[24] G. E. Stillman, C. M. Wolfe, C. O. Bozler, and J. A. Rossi, "Electroabsorption in GaAs and its application to waveguide detectors and modulators," *Applied Physics Letters*, vol. 28, no. 9, pp. 544–546, May 1976. doi:10.1063/1.88816

[25] D. A. Miller et al., “Band-Edge Electroabsorption in Quantum Well Structures: The Quantum-Confined Stark Effect,” *Physical Review Letters*, vol. 53, no. 22, pp. 2173–2176, Nov. 1984. doi:10.1103/physrevlett.53.2173

[26] A. G. Chynoweth, “Ionization rates for electrons and holes in Silicon,” *Physical Review*, vol. 109, no. 5, pp. 1537–1540, Mar. 1958. doi:10.1103/physrev.109.1537

[27] M. M. Hayat, B. E. Saleh, and M. C. Teich, “Effect of Dead Space on Gain and Noise of Double-Carrier-Multiplication Avalanche Photodiodes,” *Optical Society of America Annual Meeting*, 1991. doi: 10.1364/oam.1991.fu2

[28] R. J. McIntyre, “A new look at impact ionization-PART I: A theory of gain, noise, breakdown probability, and frequency response,” *IEEE Transactions on Electron Devices*, vol. 46, no. 8, pp. 1623–1631, 1999. doi:10.1109/16.777150

[29] S. A. Plimmer et al., “Investigation of impact ionization in thin GaAs diodes,” *IEEE Transactions on Electron Devices*, vol. 43, no. 7, pp. 1066–1072, Jul. 1996. doi:10.1109/16.502416

[30] G. E. Stillman and C. M. Wolfe, “Avalanche Photodiodes,” *Semiconductors and Semimetals*, pp. 291–393, 1977. doi:10.1016/s0080-8784(08)60150-7

[31] K. S. Lau et al., “Excess noise measurement in avalanche photodiodes using a Transimpedance amplifier front-end,” *Measurement Science and Technology*, vol. 17, no. 7, pp. 1941–1946, Jun. 2006. doi:10.1088/0957-0233/17/7/036

[32] K. F. Li et al., “Avalanche multiplication noise characteristics in thin GaAs p^+-i-n^+ diodes”, *IEEE Transactions on Electron Devices*, vol. 45, no. 10, pp. 2102–2107, 1998. doi:10.1109/16.725242

[33] D. S. Ong, K. F. Li, G. J. Rees, J. P. David, and P. N. Robson, “A simple model to determine multiplication and noise in avalanche photodiodes,” *Journal of Applied Physics*, vol. 83, no. 6, pp. 3426–3428, Mar. 1998. doi:10.1063/1.367111

[34] I. K. Czajkowski, J. Allam, and A. R. Adams, “Role of satellite valleys in ionisation rate enhancement in multiple quantum well avalanche photodiodes,” *Electronics Letters*, vol. 26, no. 16, p. 1311, 1990. doi:10.1049/el:19900843

[35] R. D. Richards et al., “Molecular beam epitaxy growth of GaAsBi using As_2 and As_4,” *Journal of Crystal Growth*, vol. 390, pp. 120–124, Mar. 2014. doi: 10.1016/j.jcrysgro.2013.12.008

6. CHAPTER 6: Conclusion and future work

6.1 Conclusion

The primary objective of this thesis was to investigate the impact ionization coefficient and excess noise factor of $Al_{0.70}In_{0.30}As_{0.74}Sb_{0.26}$ grown on InP substrates. The growth of this layer was achieved using Molecular Beam Epitaxy (MBE) through the random alloy (RA) growth technology. To assess the performance of this material system, various electrical and optical characterization techniques were employed. Current-Voltage (IV) measurements were performed to evaluate the electrical properties, while Capacitance-Voltage (CV) and Secondary Ion Mass Spectrometry (SIMS) measurements were conducted to determine the i-region thickness and doping concentration. Furthermore, photocurrent measurements were carried out, allowing the determination of quantum efficiency (QE) and absorption coefficients. The wavelength-dependent multiplication measurements enabled the extraction of the impact ionization coefficients, which were analyzed using the Random Path Length (RPL) model under both pure and mixed injection conditions. The results confirmed that this material exhibits a large α/β ratio and a low excess noise factor, with the impact ionization coefficient ratio k as low as 0.04, making it a promising candidate for low-noise avalanche photodetectors.

Additionally, a comparative study was performed on a different material system, namely the GaAs/GaAsBi multiple quantum well (MQW) structures, which were also grown using MBE. Transmission Electron Microscopy (TEM) measurements were conducted to analyze the well thickness, ensuring accurate structural characterization. Multiplication measurements at 450 nm and 980 nm wavelengths were performed, and the impact ionization coefficients were extracted using the RPL local model. The findings indicate that, even with a lower Bi%, the incorporation of an MQW structure can achieve a similarly large α/β ratio compared to a bulk structure. Moreover, the excess noise results demonstrated that the value of the k was lower than expected, suggesting potential advantages in noise performance.

Overall, this research contributes to the understanding of impact ionization mechanisms in emerging semiconductor materials and provides valuable insights into the design of low-noise, high-performance avalanche photodetectors. The results highlight the potential of AlInAsSb and GaAsBi MQW structures as promising candidates for next-generation optoelectronic devices, particularly in applications requiring high gain, low noise, and tailored absorption properties. Future work may explore further optimization of growth parameters, alternative heterostructures, and device-level integration to enhance performance and broaden the applicability of these material systems.

6.2 Future work

Although this thesis has provided significant insights into the impact ionization characteristics and excess noise factors of $Al_{0.70}In_{0.30}As_{0.74}Sb_{0.26}$ and GaAs/GaAsBi MQW structures, there remain several areas for further investigation and ongoing research. Some of these studies are still in progress and have not yet been published, but a brief overview of the planned work is provided below.

Firstly, the impact ionization coefficients of $Al_{0.70}In_{0.30}As_{0.74}Sb_{0.26}$ reported in this thesis were determined at room temperature. However, to fully understand the temperature dependence of impact ionization processes in this material, low- and high-temperature measurements are currently being conducted. These measurements will provide critical insights into carrier dynamics, thermal stability, and breakdown behaviour under varying operational conditions, which are essential for practical device applications. Additionally, a Separate Absorption and Multiplication Avalanche Photodiode (SAM-APD) incorporating this layer is being developed and will require extensive performance characterization, including gain, noise, and breakdown voltage analysis.

Similarly, for the GaAs/GaAsBi MQW system, further temperature-dependent studies are necessary to evaluate IV characteristics, photocurrent responses, and impact ionization behaviour at different operating temperatures. Such investigations will be crucial in assessing the feasibility of GaAsBi-based devices under varying thermal conditions and determining whether Bi incorporation enhances or degrades temperature stability in impact ionization processes.

In addition to the materials studied in this thesis, ongoing research is being conducted on the impact ionization coefficient and excess noise factor of AlInAsBi grown on InP. Some preliminary results from this study were presented at the Semiconductor and Integrated Opto-Electronics Conference (SIOE) in Cardiff on April 5, 2023. However, further experimental work is required, particularly the growth and characterization of additional n-i-p structures, to refine the impact ionization model and validate the material's potential for low-noise avalanche photodetector applications.